

DNA 4881F

INVESTIGATION OF THE BASIC MECHANISMS OF RADIATION EFFECTS ON SEMICONDUCTOR DEVICES USED IN ELECTRO-OPTICAL SENSOR APPLICATIONS

J. R. Srour, S. Othmer, S. C. Chen, and R. A. Hartman
Northrop Corporation
Northrop Research and Technology Center
1 Research Park
Palos Verdes Peninsula, California 90274

31 August 1979

Final Report for Period January 1978—January 1979

CONTRACT No. DNA 001-78-C-0028

APPROVED FOR PUBLIC RELEASE;
DISTRIBUTION UNLIMITED.

THIS WORK SPONSORED BY THE DEFENSE NUCLEAR AGENCY
UNDER RDT&E RMSS CODE 332307P464 Z09GAXTA00760 H2590D.

Prepared for
Director
DEFENSE NUCLEAR AGENCY
Washington, D. C. 20305

79 10 26 022

AD A 076940

Destroy this report when it is no longer
needed. Do not return to sender.

PLEASE NOTIFY THE DEFENSE NUCLEAR AGENCY,
ATTN: STTI, WASHINGTON, D.C. 20305, IF
YOUR ADDRESS IS INCORRECT, IF YOU WISH TO
BE DELETED FROM THE DISTRIBUTION LIST, OR
IF THE ADDRESSEE IS NO LONGER EMPLOYED BY
YOUR ORGANIZATION.



UNCLASSIFIED

SECURITY CLASSIFICATION OF THIS PAGE (When Data Entered)

REPORT DOCUMENTATION PAGE		READ INSTRUCTIONS BEFORE COMPLETING FORM
1. REPORT NUMBER DNA 4881F	2. GOV. ACCESSION NO.	3. RECIPIENT'S CATALOG NUMBER
4. TITLE (and Subtitle) INVESTIGATION OF THE BASIC MECHANISMS OF RADIATION EFFECTS ON SEMICONDUCTOR DEVICES USED IN ELECTRO-OPTICAL SENSOR APPLICATIONS		5. TYPE OF REPORT & PERIOD COVERED Final Report for Period Jan 78—Jan 79
		6. PERFORMING ORG. REPORT NUMBER NRTC 79-9R
7. AUTHOR(s) Joseph R. Srour Susan C. Chen Siegfried Othmer Robert A. Hartmann		8. CONTRACT OR GRANT NUMBER(s) DNA 001-78-C-0028
9. PERFORMING ORGANIZATION NAME AND ADDRESS Northrop Corporation, Northrop Research and Technology Center, 1 Research Park Palos Verdes Peninsula, California 90274		10. PROGRAM ELEMENT, PROJECT, TASK AREA & WORK UNIT NUMBERS Subtask Z99QAXTA007-66
11. CONTROLLING OFFICE NAME AND ADDRESS Director Defense Nuclear Agency Washington, D.C. 20305		12. REPORT DATE 31 August 1979
		13. NUMBER OF PAGES 146
14. MONITORING AGENCY NAME & ADDRESS (if different from Controlling Office)		15. SECURITY CLASS (of this report) UNCLASSIFIED
		15a. DECLASSIFICATION/DOWNGRADING SCHEDULE
16. DISTRIBUTION STATEMENT (of this Report) Approved for public release; distribution unlimited.		
17. DISTRIBUTION STATEMENT (of the abstract entered in Block 20, if different from Report)		
18. SUPPLEMENTARY NOTES This work sponsored by the Defense Nuclear Agency under RDT&E RMSS Code B323078464 Z99QAXTA00766 H2590D.		
19. KEY WORDS (Continue on reverse side if necessary and identify by block number) Silicon Neutron Damage Extrinsic Silicon Carrier Removal Silicon Dioxide Infrared Detectors Charge-coupled Devices Radiation Hardening Depletion Region MOS Capacitors		
20. ABSTRACT (Continue on reverse side if necessary and identify by block number) This report describes results of an investigation of radiation effects on semiconductor devices used in electro-optical sensor applications. Emphasis is placed on determining the basic mechanisms of the interaction of radiation with such devices with a view toward gaining understanding of benefit to developers of radiation-tolerant devices. A study of ionizing radiation effects on silicon MOS devices was performed at temperatures ranging from 4 to 77°K. Charge buildup in the SiO ₂ layer was observed to be identical at 4 and		

DD FORM 1 JAN 73 1473

EDITION OF 1 NOV 65 IS OBSOLETE

UNCLASSIFIED

SECURITY CLASSIFICATION OF THIS PAGE (When Data Entered)

UNCLASSIFIED

SECURITY CLASSIFICATION OF THIS PAGE(When Data Entered)

19. KEY WORDS (Continued)

Dark Current	Generation Centers
Neutron Irradiation	Neutron Damage Coefficients
Gamma Irradiation	Ionizing Radiation Effects
Low-temperature Radiation Effects	Basic Mechanisms
Charge Buildup	Electro-optical Sensors

20. ABSTRACT (Continued)

170K after a steady-state exposure to ionizing radiation, which indicates that electron trapping is not important at 40K. Results at both temperatures can be accounted for quite well in terms of hole trapping and hole transport. An investigation of the basic mechanisms of radiation effects on extrinsic silicon detector material was initiated. Carrier removal produced by neutron bombardment of such material was studied and it was found that the introduction rate of compensating defects depends strongly on the depth within the forbidden gap of the intentional dopant level. A detailed study of radiation effects on charge-coupled devices was performed, with emphasis placed on examining changes in dark current density produced by bombardment with neutrons and with ionizing radiation. The rate of increase in dark current density was found to be very similar for neutron-irradiated buried-channel CCDs obtained from two sources. Results of short-term annealing measurements on CCDs following pulsed neutron bombardment are also presented. A damage coefficient appropriate for describing the introduction of damage in silicon depletion regions was experimentally determined. This coefficient was then used to predict neutron-induced increases in dark current for various silicon devices.

UNCLASSIFIED

SECURITY CLASSIFICATION OF THIS PAGE(When Data Entered)

PREFACE

The authors wish to thank C. P. Chang, K. G. Aubuchon, and E. Harari of Hughes Aircraft for supplying some of the devices used in this investigation. In addition, helpful discussions with H. E. Boesch, C. P. Chang, J. M. Killiany, J. M. McGarrity, and F. B. McLean are gratefully acknowledged.

TABLE OF CONTENTS

<u>Section</u>	<u>Page</u>
1.0 INTRODUCTION AND SUMMARY.	9
2.0 IONIZING RADIATION EFFECTS ON MOS DEVICES AT CRYOGENIC TEMPERATURES.	12
2.1 Introduction and Background.	12
2.2 Experimental Methods and Results	15
2.2.1 Measurements of Flatband Shifts at 4 ⁰ K Using Optical Excitation.	15
2.2.2 Measurements of Flatband Shift at 18-20 ⁰ K	21
2.2.3 Direct Measurements of Flatband Shift at 4 ⁰ K.	29
2.2.4 Oxide Thickness Dependence of Charge Buildup.	38
2.3 Discussion and Conclusion.	42
3.0 MECHANISMS OF RADIATION EFFECTS ON EXTRINSIC SILICON DETECTORS	43
3.1 Introduction	43
3.2 Background	43
3.3 Experimental Results	54
3.4 Discussion and Summary	60
4.0 MECHANISMS OF RADIATION EFFECTS ON CHARGE-COUPLED DEVICES	66
4.1 Neutron Damage Mechanisms in Charge Transfer Devices.	67
4.1.1 Introduction	67
4.1.2 Experimental Considerations	67
4.1.3 MOS Capacitor Results	75
4.1.4 CCD Results	83
4.1.5 Discussion.	86
4.1.6 Summary	89
4.2 Additional Studies of Radiation Effects on Charge-Coupled Devices.	92
4.2.1 Introduction	92
4.2.2 Experimental Procedures	92
4.2.3 Ionizing Radiation Effects	96
4.2.4 Neutron Effects	107
4.2.5 Summary	115

TABLE OF CONTENTS (Continued)

<u>Section</u>	<u>Page</u>
5.0 NEUTRON DAMAGE COEFFICIENT FOR SILICON DEPLETION REGIONS, . . .	116
5.1 Introduction	116
5.2 Analytical Considerations.	116
5.3 Comparison of Calculations with Experimental Data.	121
5.4 Discussion and Conclusions	130
6.0 REFERENCES.	135

LIST OF ILLUSTRATIONS

<u>Figure</u>		
2-1	Schematic diagram of the experimental method for making 3-Hz CV measurements.	18
2-2	Flatband voltage shift in MOS capacitors as a function of bias applied during irradiation to 10^4 rads(Si)	20
2-3	5-Hz capacitance signal in accumulation as a function of reciprocal temperature.	22
2-4	Flatband voltage shift in MOS capacitors as a function of bias applied during irradiation to 10^4 rads(Si) at 4°K	23
2-5	Flatband voltage shift in MOS capacitors as a function of bias applied during irradiation to 10^4 rads(Si) at 77°K	24
2-6	Comparison of flatband-voltage shift data obtained at 19 and 77°K (composite of Figures 2-4 and 2-5)	25
2-7	Quasistatic CV measurement at 18°K before irradiation	27
2-8	Schematic diagram of the experimental method for measuring flatband voltage utilizing accumulation charge.	31
2-9	Quasistatic measurement of flatband voltage at 4°K using accumulation charge	31
2-10	Magnitude of the capacitance signal as a function of modulation frequency.	34
2-11	Comparison of CV curves obtained at various temperatures under differing measurement conditions.	37
2-12	Flatband voltage shift as a function of field applied during irradiation for MOS capacitors with various oxide thicknesses	39

LIST OF ILLUSTRATIONS (Continued)

<u>Figure</u>		<u>Page</u>
2-1	Flatband voltage shift at 2.4×10^6 V/cm as a function of oxide thickness (derived from Figure 2-12).	40
3-1	Band diagram for the lowest acceptor state of zinc in silicon	45
3-2	Schematic diagram of the method for making Hall mobility, resistivity, and carrier concentration measurements	55
3-3	Carrier concentration as a function of temperature for a zinc-diffused sample.	55
3-4	Results of measurements of sample resistance as a function of temperature before and after neutron irradiation for a zinc-diffused sample.	58
3-5	Results of measurements of sample resistance as a function of temperature for a sulfur-diffused sample before and after neutron irradiation	59
3-6	Level diagram for gold in silicon, showing the deep acceptor level, the deep donor level, and the tri-gold shallow acceptor state.	61
3-7	Results of measurements of carrier concentration as a function of temperature for a gold-diffused sample before and after neutron irradiation.	62
4-1	Schematic of an MOS capacitor on n-type silicon with an applied bias V_g more negative than the flatband voltage	69
4-2	Zerbst plot for an unirradiated MOS capacitor	71
4-3	Dark output voltage versus integration time for an unirradiated CCD.	73
4-4	Storage time degradation in neutron-irradiated MOS capacitors.	76
4-5	Generation lifetime degradation in neutron-irradiated MOS capacitors.	77
4-6	Surface generation velocity increase in irradiated MOS capacitors.	78
4-7	Storage time versus reciprocal temperature for irradiated and unirradiated MOS capacitors on an n-type substrate.	82

LIST OF ILLUSTRATIONS (Continued)

<u>Figure</u>		<u>Page</u>
4-8	Generation lifetime and surface generation velocity versus reciprocal temperature for irradiated and unirradiated MOS capacitors on an n-type substrate.	83
4-9	Change in dark output voltage due on both pulsed and steady-state neutron bombardment for CCDs irradiated in an un-powered mode	84
4-10	Normalized dark current density versus reciprocal temperature with neutron fluence as a parameter	90
4-11	Block diagram of and pin identification for the Fairchild CCD 311.	93
4-12	Schematic diagram of the circuit used in radiation testing of the CCD 311	94
4-13	Drive circuit for the Fairchild CCD 311.	95
4-14	Timing diagram for the CCD 311	97
4-15	Pin connections for the CCD 311 during irradiation	97
4-16	Differential amplifier used with the CCD 311 to eliminate the reset pulse at the output.	98
4-17	Drive amplifiers used with the CCD 311	98
4-18	Schematic diagram of the Hughes Aircraft buried-channel CCD	99
4-19	Radiation-induced change in dark output voltage for the Hughes Aircraft CCD	99
4-20	Change in dark output voltage versus ionizing dose for the Hughes Aircraft CCD	100
4-21	Dark current density versus ionizing dose for the Fairchild CCD 311	102
4-22	Dark current density versus ionizing dose for Hughes Aircraft CCDs	103
4-23	Change in dark current density versus ionizing dose for a Hughes Aircraft CCD	104
4-24	Change in dark current density versus ionizing dose	105
4-25	Illustration of charge buildup in the field oxide for a CCD	106

LIST OF ILLUSTRATIONS (Continued)

<u>Figure</u>		<u>Page</u>
4-26	Change in dark current density versus neutron fluence for the Fairchild CCD 311.	108
4-27	Dark current density versus time following pulsed neutron bombardment for the Fairchild CCD 311 (Device J6).	109
4-28	Dark current annealing factor versus time for the Fairchild CCD 311.	111
4-29	Dark current density versus time following pulsed neutron bombardment for the Fairchild CCD 311 (Device J3).	112
4-30	Dark current annealing factor versus time for the Fairchild CCD 311	113
5-1	Neutron-induced change in reciprocal generation lifetime for MOS capacitors on bulk n- and p-type silicon	119
5-2	Calculated values of the neutron-induced change in generation current density as a function of depletion region width for three temperatures	120
5-3	Change in dark current density versus neutron fluence for Spectronics PIN diodes	124
5-4	Change in dark current density versus neutron fluence for a Hewlett-Packard PIN diode.	125
5-5	Change in dark current density versus neutron fluence for United Detector Technology PIN diodes.	126
5-6	Change in dark current density versus neutron fluence for EG&G PIN diodes.	127
5-7	The quantity $(J_d - J_{d0})/x_d$ versus neutron fluence for various PIN diodes	131

LIST OF TABLES

<u>Table</u>		<u>Page</u>
2-1	Comparison of 3-Hz and quasistatic measurements of flatband voltage shift at 20°K after a 10 ⁴ -rad irradiation at 4°K	28
2-2	Additional comparison of 3-Hz and quasistatic measurements of flatband voltage shift (dose = 10 ⁴ rads(Si)).	28
2-3	Sequential measurement of flatband shifts at 4°K and 20°K. . .	36

LIST OF TABLES (Continued)

<u>Table</u>		<u>Page</u>
4-1	Experimentally determined damage coefficients.	79
4-2	Comparison of values for $d(J_d - J_{d0})/d\phi$ derived from data obtained by various workers.	88
4-3	Comparison of measured and calculated "permanent" changes in dark current density for irradiated CCD 311s.	114
5-1	Active area, pre-irradiation capacitance under reverse bias, and calculated depletion-layer width for PIN photo-diodes studied by Kalma and Hardwick	123
5-2	The ratio of calculated to experimental values of the quantity $J_d - J_{d0}$ at various neutron fluences based on information in Figures 5-3 to 5-6.	128

SECTION 1.0

INTRODUCTION AND SUMMARY

This report describes results of an investigation of radiation effects on semiconductor devices used in electro-optical sensor applications. Emphasis is placed on determining the basic mechanisms of the interaction of radiation with such devices with a view toward gaining understanding of benefit to developers of radiation-tolerant devices. Section 2.0 describes results of a study of ionizing radiation effects on silicon MOS devices at cryogenic temperatures. In Section 3.0, findings of an investigation of the mechanisms of radiation effects on extrinsic silicon detector material are presented. Section 4.0 describes results of a study of neutron- and ionizing-radiation effects on charge-coupled devices. In Section 5.0, the topic of a neutron damage coefficient appropriate for silicon depletion regions is addressed. The remainder of the present section summarizes major findings reported in this document.

A study of ionizing radiation effects on silicon MOS devices was performed at temperatures ranging from 4 to 77°K. Emphasis was placed on comparing behavior at 4°K with that at 77°K for the purpose of determining whether electron trapping is important at the lower temperature. Various experimental techniques were employed to obtain appropriate pre- and post-irradiation electrical data on the MOS capacitors employed as test vehicles. Conventional C-V measurement techniques are inapplicable at 4°K because of carrier freeze-out. It is therefore necessary to generate sufficient majority carriers to maintain charge neutrality as the silicon substrate is swept from accumulation to depletion. This was accomplished here by two approaches: 1) use of optical excitation; 2) use of the Co^{60} gamma rays employed for irradiation as a source of carriers, thereby permitting C-V measurements during bombardment. Comparison C-V measurements were made at 18-20°K using solely thermal excitation of carriers. It is the compelling conclusion of this work that charge buildup at 4°K in irradiated SiO_2 films can be described exclusively in terms of hole trapping since results observed at 77°K, which previously have been successfully modeled on this basis, are identical to the lower-temperature findings. Strictly speaking, this conclusion should be modified to apply specifically to the case of the wet oxides studied and to the particular irradiation conditions employed (steady-state ionizing radiation--20 minute time scale-- 10^4 rads(Si)). It remains a possibility that significant electron trapping may be observed on

shorter time scales, and this issue should be addressed. We also raise the possibility that electron trapping and transport in SiO_2 may be dependent on oxide processing conditions.

An investigation of the basic mechanisms of radiation effects on extrinsic silicon detectors was initiated. Such devices are becoming technologically important because of their suitability for the fabrication of monolithic focal-plane arrays to be utilized in infrared imaging applications. The work reported here constitutes the beginning of an effort that will continue in a subsequent program during 1979. We first provide a detailed background discussion of radiation effects on extrinsic silicon. Experimental results obtained on neutron-irradiated Si:S , Si:Zn , and Si:Au are then presented. Hall measurements were performed as a function of temperature before and after bombardment in order to determine carrier removal rates. It was found that the introduction rate of compensating defects depends strongly on the depth within the forbidden gap of the intentional dopant level. Specifically, a donor level 0.19 eV from the conduction band (sulfur) appears to be compensated nearly as effectively as a shallow donor (arsenic). On the other hand, the carrier removal rate was found to be considerably smaller for an acceptor level 0.31 eV from the valence band (zinc). Interpretations of the data obtained to date are given, as are suggestions for relevant future investigations in this area.

A detailed study of radiation effects on charge-coupled devices has been performed, with emphasis placed on examining changes in dark current density produced by bombardment with neutrons and with ionizing radiation. Devices from two manufacturers were examined: CCDs and MOS capacitors from Hughes Aircraft (HAC) and CCDs from Fairchild Semiconductors (CCD 311). The MOS capacitors were used to obtain a neutron damage coefficient appropriate for describing increases in the generation-center density in silicon depletion regions. Capacitors were also employed to obtain gamma-ray damage coefficients associated with increases in surface generation velocity at the SiO_2 -Si interface. The rate of increase in dark current density for neutron-irradiated CCDs was measured and found to be very similar for HAC and Fairchild CCDs (3.5×10^{-11} nanoamps per fission neutron for the Fairchild device). A discussion is presented which indicates that a moderate reduction in the operating temperature of a CCD should substantially reduce its sensitivity to the production of dark current by neutron bombardment. The HAC CCDs studied were found to be quite sensitive to the effects

of ionizing radiation when irradiated under power. Short-term annealing measurements were performed in which dark current density in the CCD 311 was monitored as a function of time following pulsed neutron bombardment. As an example, at 20 sec after irradiation the dark current annealing factor was ~ 1.7 . This means that, at a given fluence, the neutron-induced increase in dark current density is a factor of 1.7 larger at 20 sec after bombardment than it is at some much longer time (such as 30 minutes).

In the MOS capacitor studies mentioned above, a generation-lifetime damage coefficient (K_g) was obtained that is appropriate for introduction of damage in silicon depletion regions by neutron bombardment. The value obtained, 7.0×10^6 n-sec/cm², appears to apply for depletion regions in both n- and p-type silicon at room temperature and also is a good value for use over a moderate temperature range (~ 240 to $\sim 370^\circ\text{K}$, the range studied). We explored the possibility that this damage coefficient might be useful for predicting the effects of neutron bombardment on silicon devices. We have found that leakage current data obtained for various neutron-irradiated silicon devices, including CCDs, PIN diodes, and JFETs, can be described reasonably well using a model which incorporates the unique value of K_g obtained in this investigation. Agreement between calculations and experimental results is within a factor of ≤ 2 in most cases, which suggests that the calculational approach employed is suitable for making reasonably accurate estimates of neutron-induced increases in dark current for silicon devices.

SECTION 2.0

IONIZING RADIATION EFFECTS ON MOS DEVICES AT CRYOGENIC TEMPERATURES

2.1 INTRODUCTION AND BACKGROUND

The transport properties of holes in silicon dioxide films grown on silicon were the subject of study in our laboratory several years ago,¹⁻³ and the mechanisms of transport are now reasonably well understood, at least to the point where predictions can be made for the performance of MOS devices operated at cryogenic temperatures.^{4,5} The hole conduction process was found to be governed by traps distributed in energy and space. This process was therefore strongly thermally activated, so that near-permanent trapping of holes occurs at low-to-moderate applied fields at cryogenic temperatures (77°K).

In the above studies, which were performed at 77°K or above, electrons were found to be transported through the SiO₂ films on a time scale short compared to the experimental resolution (10 μsec). Consequently, there was no evidence of trap-limited conduction for electrons. Moreover, previous studies of electron transport through SiO₂ films revealed that the electron mobility was quite high for amorphous material (on the order of 20 cm²/V-sec), and exhibited a decrease with increasing temperature, which is consistent with dominance by scattering processes rather than activation processes.⁶ It thus appeared that electron transport was of a fundamentally different character than hole transport. Electrons are apparently governed by their intrinsic, or scattering-limited, mobility whereas holes drift with their characteristic scattering-limited mobility only on a time scale of nanoseconds before being trapped. It is also possible, however, that trap-limited conduction of electrons might manifest itself at temperatures low compared to the previous region of measurement. If that is in fact the case, then operation of devices at such temperatures at which electrons are semipermanently trapped could serve as a partial remedy for the problem of positive charge buildup at cryogenic temperatures.⁴ The compensation of trapped holes by trapped electrons could have practical merit even if it were transient. In any case, the possibility of such trapping in SiO₂ films deserved examination.

To make it plausible that electron trapping at low temperatures might be observable, it is worthwhile to discuss the hole conduction process qualitatively in more detail. The trap-limited conduction process has been successfully

modeled by two very different approaches. One is based on a multiple-trapping picture, in which holes transported through an oxide film under the influence of an applied field incur a probability of being trapped in states which are distributed in energy within the band gap.⁷ The deeper states have longer de-trapping times, so that a given hole population which is suddenly introduced progressively distributes itself in the deeper states, thus reducing the apparent mobility with time, and giving rise to exceedingly "dispersive" transport. The trap density of states which fits the data for the oxide studied in detail in our laboratory is a simple one in which the density is an exponentially declining function of depth in energy from the band edge.⁷ Such a density of states function has the virtue of being physically reasonable for a disordered solid.

The alternative model for the description of hole transport is the purely statistical stochastic transport model of Scher and Montroll, as applied to the case of SiO_2 films by McLean et al.⁸⁻¹⁰ That model, referred to as Continuous Time Random Walk (CTRW), does not presuppose a physical mechanism for the origin of the dispersion in carrier transport. In particular, it has been shown to encompass the multiple-trapping model as a particular case under certain conditions.¹¹ In general, however, the dispersion in transport can arise from a number of possible mechanisms. A generalized description has the advantage that all manner of observed dispersive transport processes can be treated within the same framework, but one difficulty is that the parameters of such a model are not easily associated with unique physical interpretations.

R. C. Hughes has likewise treated the hole transport problem in SiO_2 films in terms of the CTRW model, and ascribed deviations from that model at early times to the manifestation of intrinsic hole mobility prior to trapping.¹² This intrinsic mobility is also found to be thermally activated, and to be relatively small compared to electron mobility. The activation energy of about 0.16 eV is taken to imply polaronic hopping motion. McLean et al.⁹ observed charge transport governed by activation energies of less than 0.1 eV at low temperatures which were likewise interpreted in terms of polaron motion. The higher temperature behavior is governed by activation energies similar to those observed in an oxide studied at Northrop³ (~ 0.4 eV).

If it can be established that the hole transport data necessarily imply a

spread in the density of states at the valence band edge of a certain magnitude, then it is possible to argue that the same mechanisms give rise to a distribution of states at the conduction band edge, although the width in energy may be different. In the multiple-trapping model of hole transport, the trap energy levels which are found are measured with respect to the valence band edge, and the implication is that the density of states falls off exponentially from this edge, with a spread on the order of 0.4 eV. On the other hand, a number of different mechanisms of trap-limited transport could be subsumed under the CTRW model. If the polaron model is valid--and the weight of evidence in papers referenced above appears to be strongly in favor of small-polaron formation for holes--then the dominant activation energies characterizing transport (0.4 eV) would be interpreted in terms of the polaron binding energy. A spread in the observed activation energies could be interpreted in terms of a distribution of band-tail states ascribable to disorder, but an interpretation in terms of a site-dependence of the polaron binding energy may be more appropriate, in which case no inference could be readily drawn for the density of states at the valence band edge. However, even in the event that no appeal can be made to our knowledge about the valence band edge, general arguments can be given for expecting at least some tail in the density of states at the conduction band, and these are given below.

It is helpful to recall at this point that the oxides which were originally fitted in terms of the multiple-trapping model and the CTRW model, respectively, were in fact quite different in their dispersive transport behavior. The oxide studied at Northrop³ indicated a wide distribution of energy levels, whereas the oxides which yielded the best fit to the one-parameter CTRW model showed very little spread in activation energies.⁹ The implication is that processing differences between different oxides could result in a considerably different spread of the density of states at the valence band edge, and, by implication, at the conduction band edge.

It has been argued above that a spread of energies at the valence band edge has similar implications for the conduction band edge, and yet it is clear from the electron transport behavior already observed that the "scale" of this spread is very different in the two cases. Molecular orbital theory can be used to explain this difference. Electronic structure calculations have been performed on quartz which showed that changes in the Si-O-Si bond angle introduce significant changes in the valence band edge.¹³ A distribution of such bond angles, as is likely to be present in amorphous SiO₂, is therefore sufficient to explain the

spread of energies implied by the multiple trapping picture (0.4 eV). The effect of this variation in bond angle on the conduction band edge is considerably reduced, according to the molecular orbital picture. Similar conclusions may be drawn from another study of the electronic structure of amorphous SiO_2 , quartz and cristobalite.¹⁴ The effect of bond angle variations on the valence band density of states is greater than that of topological disorder. By contrast, the conduction band density of states reveals a relatively larger influence of disorder.

In addition to the above very general arguments, we may cite the observation of a tail in the conduction-band density of states by means of photon-assisted tunneling measurements of electrons from aluminum into the SiO_2 conduction band.¹⁵ A Gaussian tail of width 0.1 eV gave a fit to the data in most cases, except for an unannealed oxide, where a width of 0.25 eV was indicated. A profound influence of processing on the apparent band tail is suggested by these findings. The magnitude of the tail, however, is such that one would expect to see trapping-dominated mobility even at room temperature, unless the tail states are likewise "extended" states, or characteristic only of the interface. It is possible in the latter case that the applied field is sufficient to promote electrons (which have tunneled into such tail states) into extended states of the bulk.

The above considerations justify the attempt to ascertain the existence of shallow electron trapping. That the trapping must be shallow is clear from the observation of scattering-limited conduction at room temperature on the one hand, and the fact that trapping does not manifest itself at times $< 10 \mu\text{sec}$ near 77°K on the other.³

In the present study, charge buildup measurements under gamma irradiation were employed to reveal whether compensation of trapped holes by electrons occurs at 4°K . A number of different experimental methods were utilized and these will be discussed in turn, along with the results obtained with each.

2.2 EXPERIMENTAL METHODS AND RESULTS

2.2.1 Measurements of Flatband Shifts at 4°K Using Optical Excitation

Charge buildup measurements were performed on room-temperature radiation-hard oxides grown pyrogenically at 925°C to various thicknesses by Hughes Aircraft Company (Lot KA-09). Dry oxide films (1000°C growth) had previously been characterized in our laboratory at 77°K .^{3,4} Standard capacitance-versus-voltage

data were obtained at 1 MHz in that case to determine the charge buildup via shifts in the flatband voltage. Corresponding measurements were now required at 4°K. In the latter case, however, carrier freeze-out renders conventional techniques inapplicable. It is therefore necessary to generate in some manner sufficient majority carriers to maintain charge neutrality conditions in the bulk as the gate voltage is swept from accumulation to depletion. That is, the dielectric relaxation frequency ($= \rho\epsilon$, where ρ is the resistivity and ϵ the dielectric constant) must be sufficiently high for the majority carriers to follow the applied ramp waveform. This requires a silicon resistivity of no more than about 10^{11} ohm-cm, or a carrier concentration on the order of 10^{13} cm⁻³. A second criterion is imposed by the requirement that the majority carriers must be able to maintain equilibrium conditions of depletion width. That is, the rate of capture and emission of majority carriers for the shallow donor sites must be sufficiently rapid.*

In the initial experiment of this study, optical excitation was used to furnish majority carriers, and, to minimize the degree of excitation required, C-V measurements were made at 3 Hz rather than 1 MHz. In practice, the optical signal level was increased until the 3-Hz capacitance signal in accumulation nearly saturated, and thus the dielectric relaxation frequency increased to approximately 3 Hz. The optical excitation was furnished by an incandescent filament (removed from a flashlight bulb) which was placed in proximity to the sample (about 3 mm). The sample and filament were placed in a helium exchange gas environment to permit variation of sample temperature, and this prevented premature oxidation of the filament.

Samples were exposed to a total dose of 10^4 rads ($\pm 10\%$) in the exposure room of the Northrop Co-60 source. This required a period of 20 minutes, not including a period of about 5 minutes for raising, and 5 minutes for lowering, the source. Irradiation was performed in the dark, and the optical signal was employed only during periods of measurement. Detection of the 3-Hz signal was

*The limiting modulation angular frequency is given by $\omega = c_n(n + n_1)$, where c_n is the (electron) capture probability, n is the equilibrium electron concentration, and n_1 is the electron concentration if the Fermi level were at the shallow donor energy level position. No requirements are placed on equilibrium with respect to minority carriers (Ref. 16).

by means of an Ithaco 391A heterodyne lock-in detector. Insufficient phase stability was observed for the internal reference of that lock-in (due to prevailing line voltage transients) and an HP-3310A (or B) was employed instead, in conjunction with a voltage regulator.

The sample holder provided for the simultaneous irradiation of four capacitors. These were measured sequentially starting four minutes after the source descent was begun, at which time the dose rate was negligible. Due to the use of 3-Hz modulation, filter time constants larger than 1 sec had to be used, requiring low ramp rates. About one minute was required to obtain one CV-curve. In order to forestall any field-induced transport during the measurement time, sample biases were reduced on all four devices at the same 4-minute point. During the measurement itself, biases were kept sufficiently low that field-induced hole transport did not occur. For the typical sample thickness of 970 Å, the bias was held to 2V (2×10^5 V/cm), just sufficient to display the flatband shifts which were typically on the order of one volt. The circuit for the experiment described is shown in Figure 2-1. Sample temperature measurements were made by means of a carbon resistor and a platinum resistor.

Since the majority carriers are frozen out at 4°K, the device equivalent circuit at this temperature is that of a capacitor with a dual dielectric of SiO₂ and silicon. It is important to establish what fraction of the applied bias appears across the oxide in such a device. It was hypothesized that under irradiation the induced conductivity of the silicon would be far greater than that of the SiO₂, and that therefore the applied bias would be dropped almost entirely across the oxide. The narrower band gap of silicon results in a pair generation effectiveness which is five times greater than that of SiO₂. Both carriers are mobile in silicon, and the mobility ratio is in excess of 10³ with respect to estimated electron mobilities in SiO₂. The electric field strength is a factor of five greater in the SiO₂ than in silicon by virtue of differences in dielectric constant. On the other hand, the silicon thickness is considerably greater than that of the oxide (by a factor of 10³), and little can be said about relative lifetimes in the two materials a priori. During the course of the experiments a direct test of the relative conductivities under irradiation confirmed that the bias is indeed dropped entirely across the oxide, and this test is discussed below.

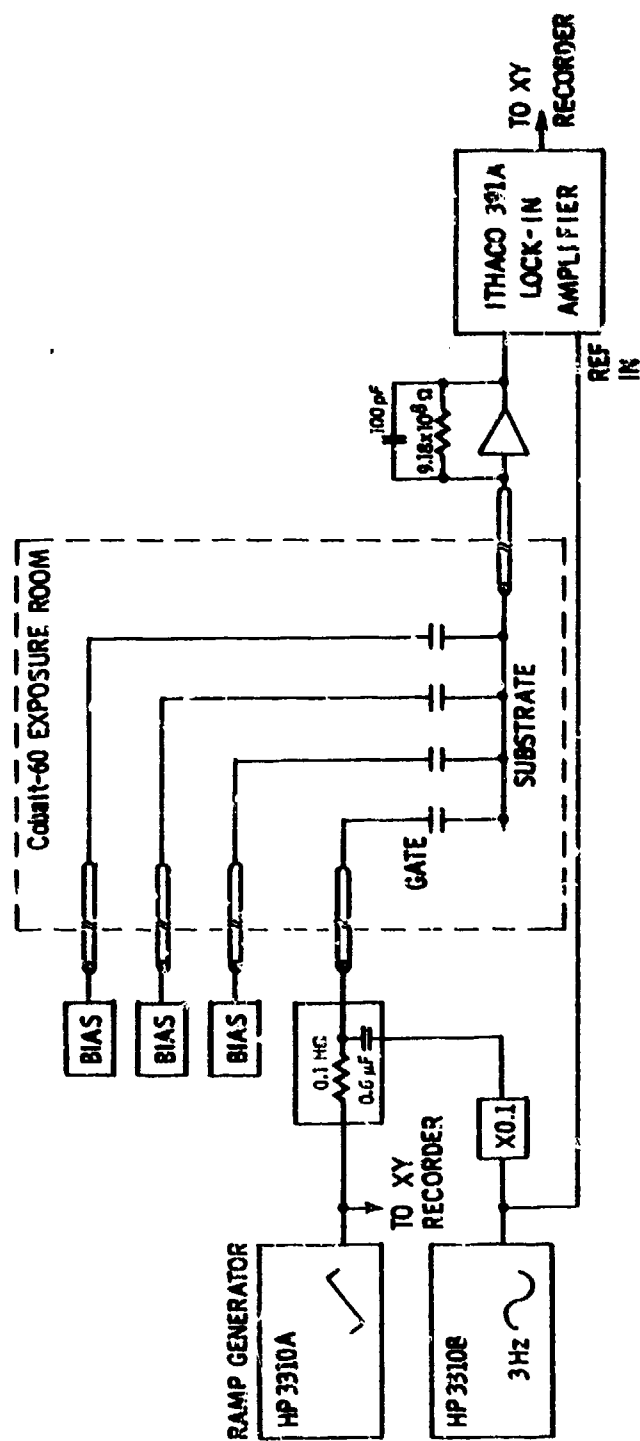


Figure 2-1. Schematic diagram of the experimental method for making 3-Hz CV measurements.

Results of measurements of flatband shift after 10^4 rads (Si) irradiation at 4°K are shown as a function of gate bias in Figure 2-2 for a sample of 970 \AA thickness. Shown on the same figure are comparable data taken at 77°K using the same experimental method (but no optical excitation). These latter data have been previously described successfully in terms of a field-dependant charge yield at low field intensities, and hole transport out of the oxide at high field intensities.⁴ In that previous modeling of transport, it was assumed that all electrons were swept out of the oxide prior to measurement. The agreement of the sets of data at the two temperatures suggests strongly that no significant electron trapping occurs at 4°K on the time scale of the measurement.

Several questions may be raised about the validity and generality of this finding. There is first of all the possibility that the optical excitation also resulted in local heating of the sample. The temperature-sensing resistor was located some 5-6 mm away from the dual-in-line package to which the device was bonded. Whereas it indicated a temperature of the sample mount of no more than 6°K during measurement, the proximity of the optical source to the device makes it difficult to rule out some local heating of the oxide film with respect to the sample holder. An upper bound of less than 19°K for the resultant sample temperature is implied by the fact that carrier excitation was optical rather than thermal in nature. Thermal excitation of sufficient carriers to permit a CV measurement would have required a silicon temperature of about 19°K . The conclusion that the excitation was in fact optical rather than thermal was based on the observation that the power which had to be supplied to the filament to obtain the required excitation in the silicon gradually increased over time, suggestive of gradual oxidation of the filament. Since the thermal resistance between the filament and the device should not be a function of time, the excitation mechanism had to be optical rather than thermal.

A second question about this measurement concerns possible excitation of electrons out of shallow traps by means of the optical signal used to generate the majority carriers. The fact that we did not observe any change in flatband shift during the course of measurement, however, suggests that excitation and sweep out of trapped charge would have to occur on a time scale short compared to a minute, implying inordinately large photoionization cross sections for

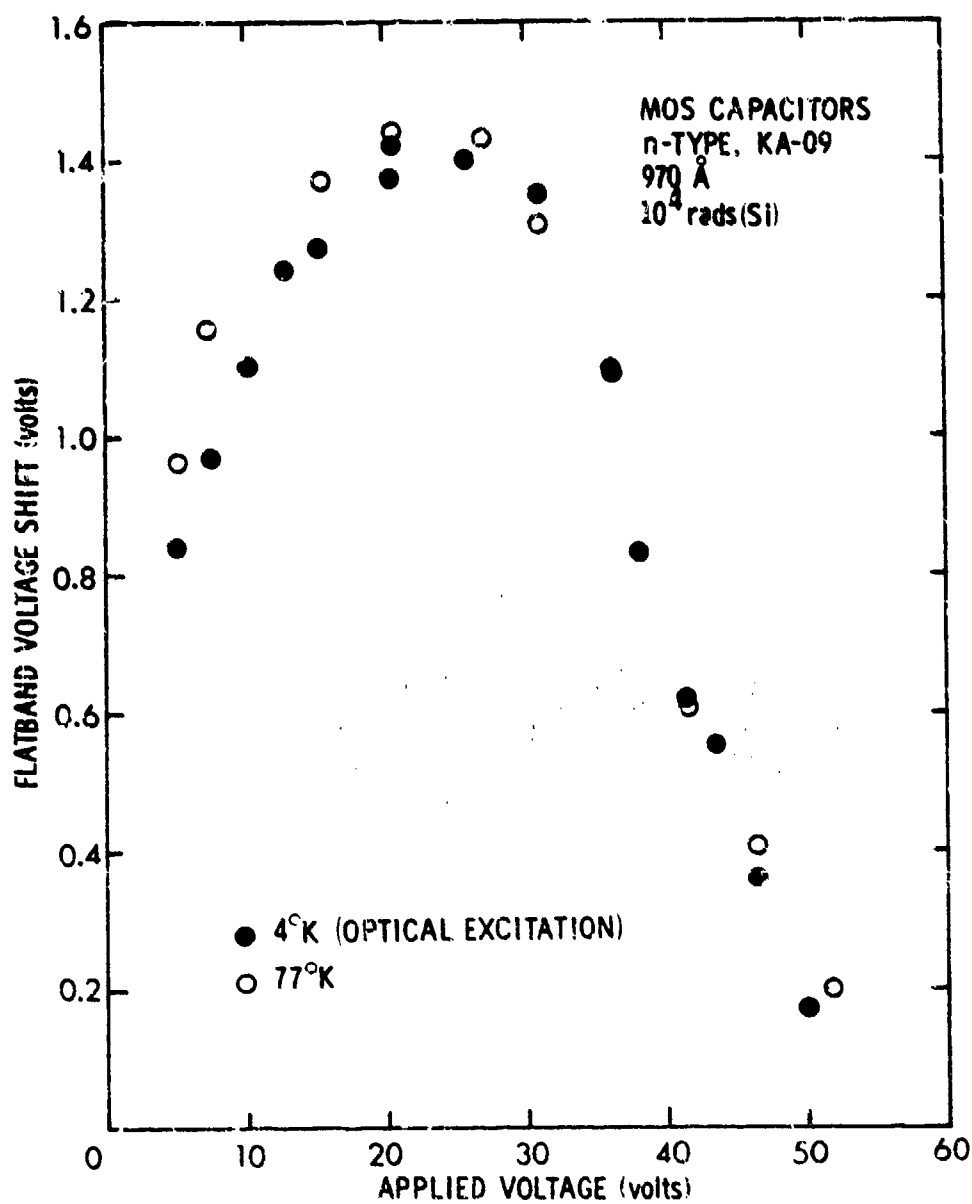


Figure 2-2. Flatband voltage shift in MOS capacitors as a function of bias applied during irradiation to 10^4 rads(Si). Data obtained at 4°K using optical excitation and at 77°K without optical excitation are shown.

such traps. A third possibility is that any shallow electron traps may be subject to field-enhanced excitation much more readily than the deeper hole traps. Whereas this cannot be ruled out, it can be stated simply that if electron trapping does not prevail at typical sample biases, then it holds no practical interest in any case.

2.2.2 Measurements of Flatband Shift at 18-20°K

The concern about possible optical excitation out of electron traps motivated an alternative approach in which excitation of the requisite majority carrier concentration was achieved thermally. The irradiation was still performed at 4°K, and the sample temperature subsequently raised just enough to permit CV-measurement at 3 Hz. Preliminary to this measurement, the 5-Hz capacitance signal in accumulation was measured as a function of temperature in order to ascertain the temperature dependence of the majority carrier concentration, or, more directly, of the dielectric relaxation frequency. These data were obtained with an Ithaco 395 narrowband voltmeter, which is preferred here by virtue of the fact that it yields the magnitude of the signal independent of signal phase. (The magnitude is derived from the vector of sum of the outputs of two phase-sensitive detectors in quadrature.) 5 Hz was the lowest frequency of operation at which phaselock to the reference could be maintained. Results are shown in Figure 2-3. Saturation of the capacitance signal is seen to require about 19-20°K for this sample. Results of measurements made using thermal excitation during measurement are shown in Figure 2-4. Comparison data taken at 77°K are shown in Figure 2-5, and the composite of these data sets is illustrated in Figure 2-6. Again, results indicate no significant difference between the charge buildup observed at 77°K (where electrons clearly do not play a role) and that observed after 4°K irradiation.

On the basis of these results, one may draw the conclusion that electron trapping does not play a role in charge buildup at 19-20°K on the time scale of the present experiments. This temperature is just sufficient to excite a small fraction of the shallow phosphorus donor levels located 0.045 eV from the conduction band. The fraction ionized may be determined as follows: the dielectric relaxation frequency of 3 Hz at operating temperature implies a carrier concentration in the bulk of $2 \times 10^3 \text{ cm}^{-3}$, on the assumption of $2 \times 10^4 \text{ cm}^2/\text{V-sec}$ mobility. The net donor doping concentration is $2 \times 10^{15} \text{ cm}^{-3}$, yielding an ionized fraction of 10^{-12} . We would expect similar fractional ionization

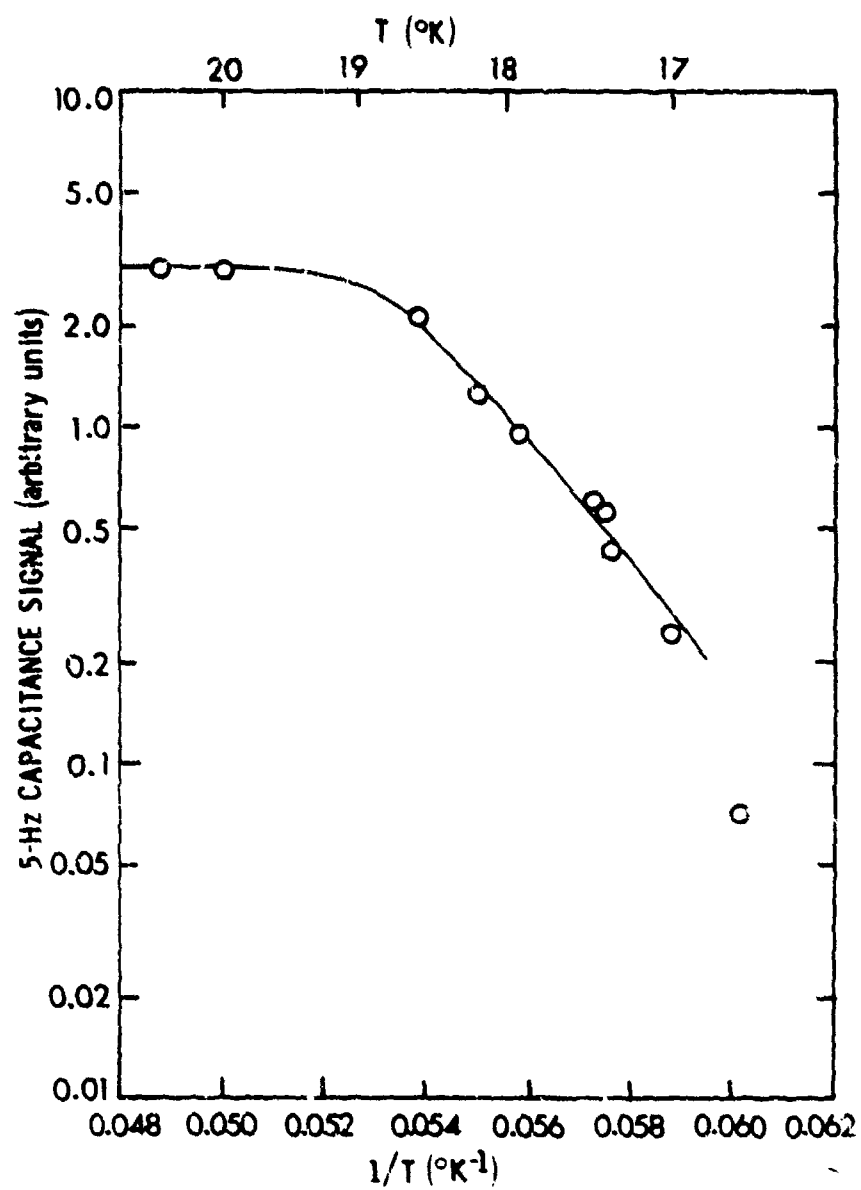


Figure 2-3. 5-Hz capacitance signal in accumulation as a function of reciprocal temperature. The fall-off at low temperature governed by dielectric relaxation is illustrated.

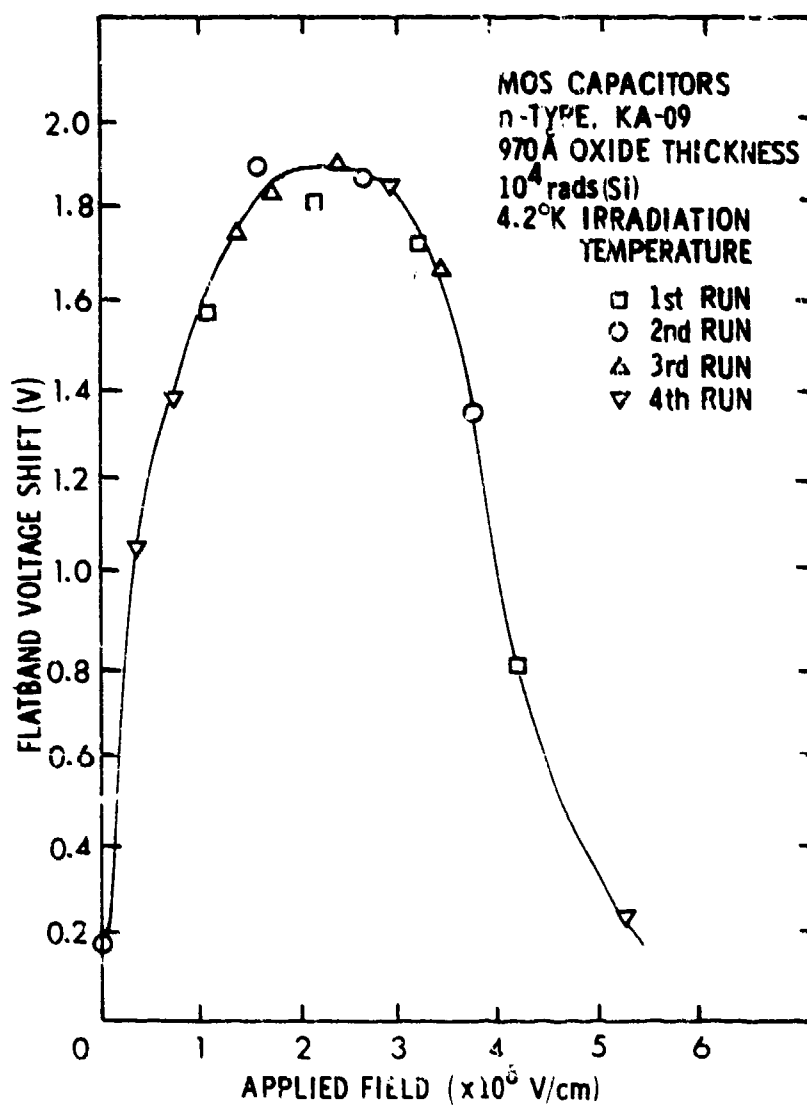


Figure 2-4. Flatband voltage shift in MOS capacitors as a function of bias applied during irradiation to 10^4 rads(Si) at 4°K. Measurements were made using thermal excitation (19-20°K).

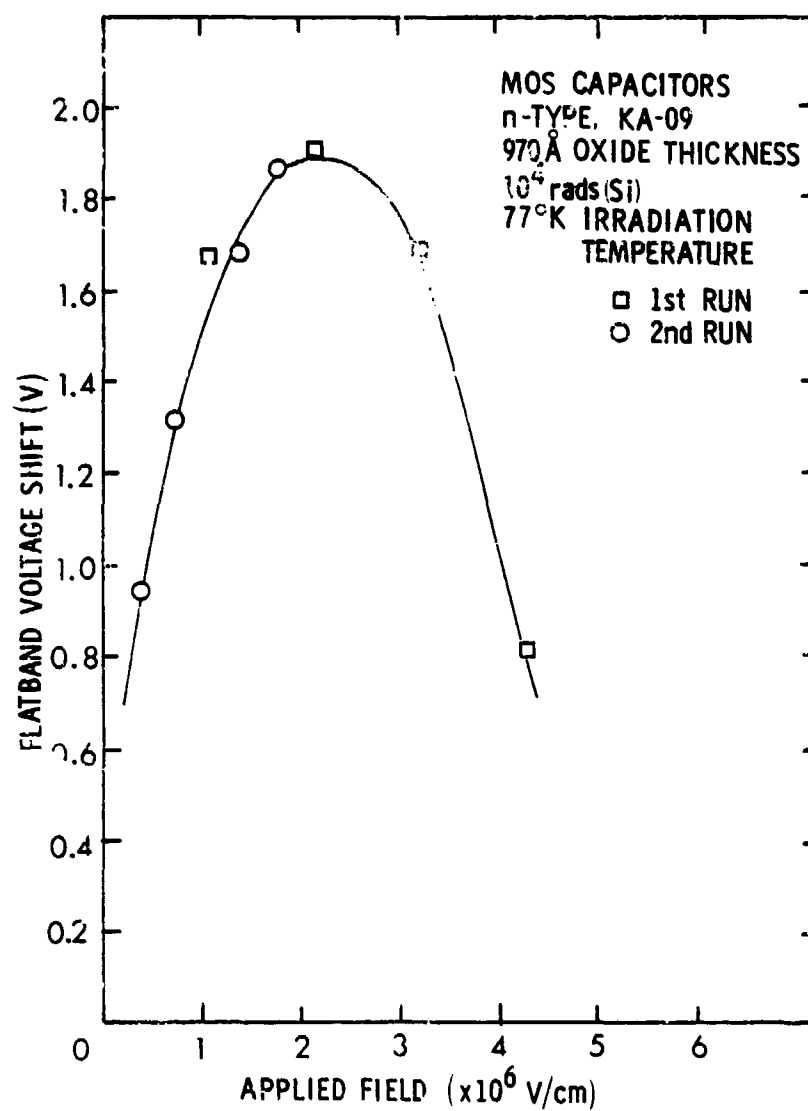


Figure 2-5. Flatband voltage shift in MOS capacitors as a function of bias applied during irradiation to 10^4 rads(Si) at 77°K.

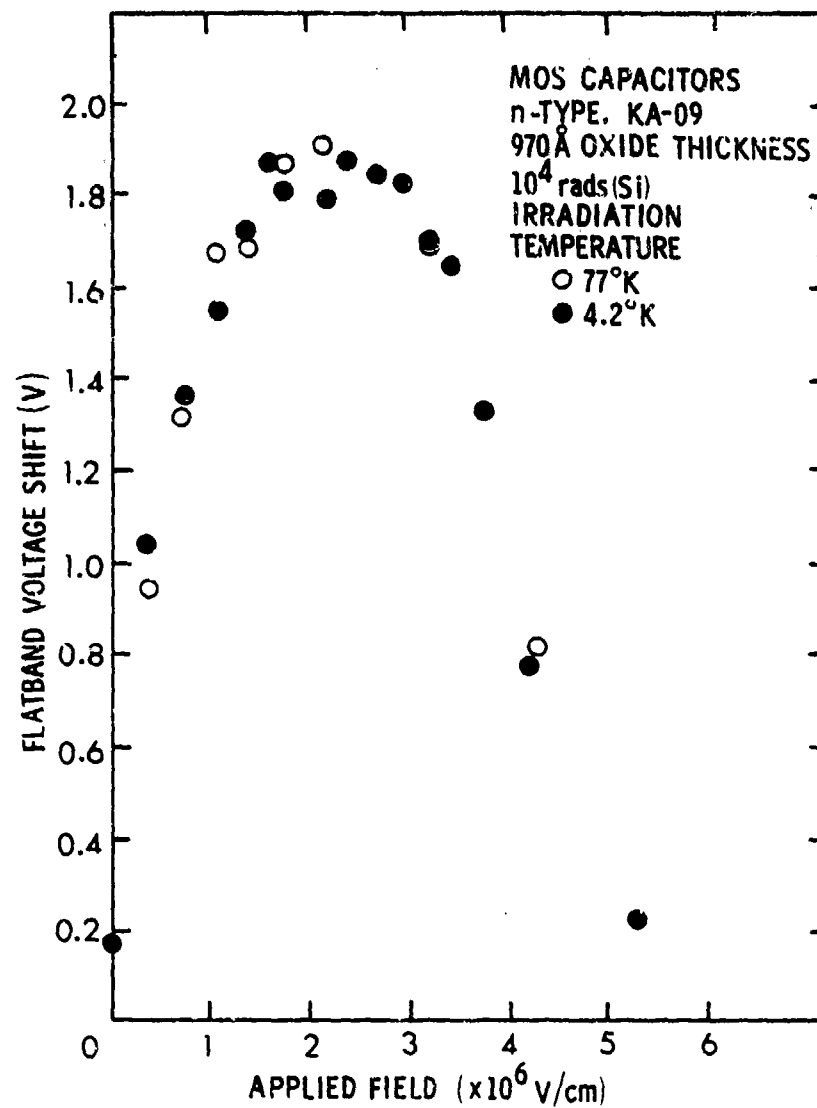


Figure 2-6. Comparison of flatband-voltage-shift data
 obtained at 19 and 77°K (composite of Figures
 2-4 and 2-5).

of traps of such energy level position with respect to the conduction band in the SiO_2 if density of states factors were the same. The latter affects the argument quantitatively to some degree, but we can state within the bounds of this approximation that electron traps on the order of 40 meV or deeper are not emptied significantly by raising the sample temperature to 19°K for measurement. We have therefore ruled out the existence of a significant population of electron traps (i.e., significant relative to the density of hole traps) deeper than about 40 meV in this oxide by the present test.

We were required to operate at 19°K for the purpose of achieving a dielectric relaxation frequency of 3 Hz to accommodate CV measurements. The same information may be obtained by quasistatic techniques, as first described by Kuhn.¹⁷ In this measurement, the majority carrier current is measured as the MOS capacitor is swept between accumulation and depletion. The condition for the validity of such data is that the dielectric relaxation frequency be high enough for the majority carriers to follow the ramp. The signal bandwidth is thus reduced, permitting reduction of the sample temperature commensurately. If the same ramp rate is used as in the above measurement, the signal bandwidth is reduced an order of magnitude with respect to the 3-Hz CV method, and reference to Figure 2-3 shows that this permits operation at a temperature of about 17°K .

The experiment was therefore repeated for a number of sample biases using the quasistatic method. Results of a pre-irradiation run are shown in Figure 2-7 for a sample of 970 Å oxide thickness. The capacitance voltage curve shows two dips between the accumulation bias condition and flatband. A dip can result from the depopulation of shallow dopant levels as the Fermi level crosses the dopant energy level position. The appearance of two dips in this case was not explained. The dips were not observed post-irradiation. Likewise, they were not observed under 3-Hz modulation, presumably due to overmodulation in that case.

Results of flatband voltage shifts using the quasistatic method were compared with 3-Hz modulation data taken at 20°K . The data are summarized in Table 2-1. Good agreement between the two methods was found; the differences that do exist were unsystematic, and indicative of the basic reproducibility of our methods.

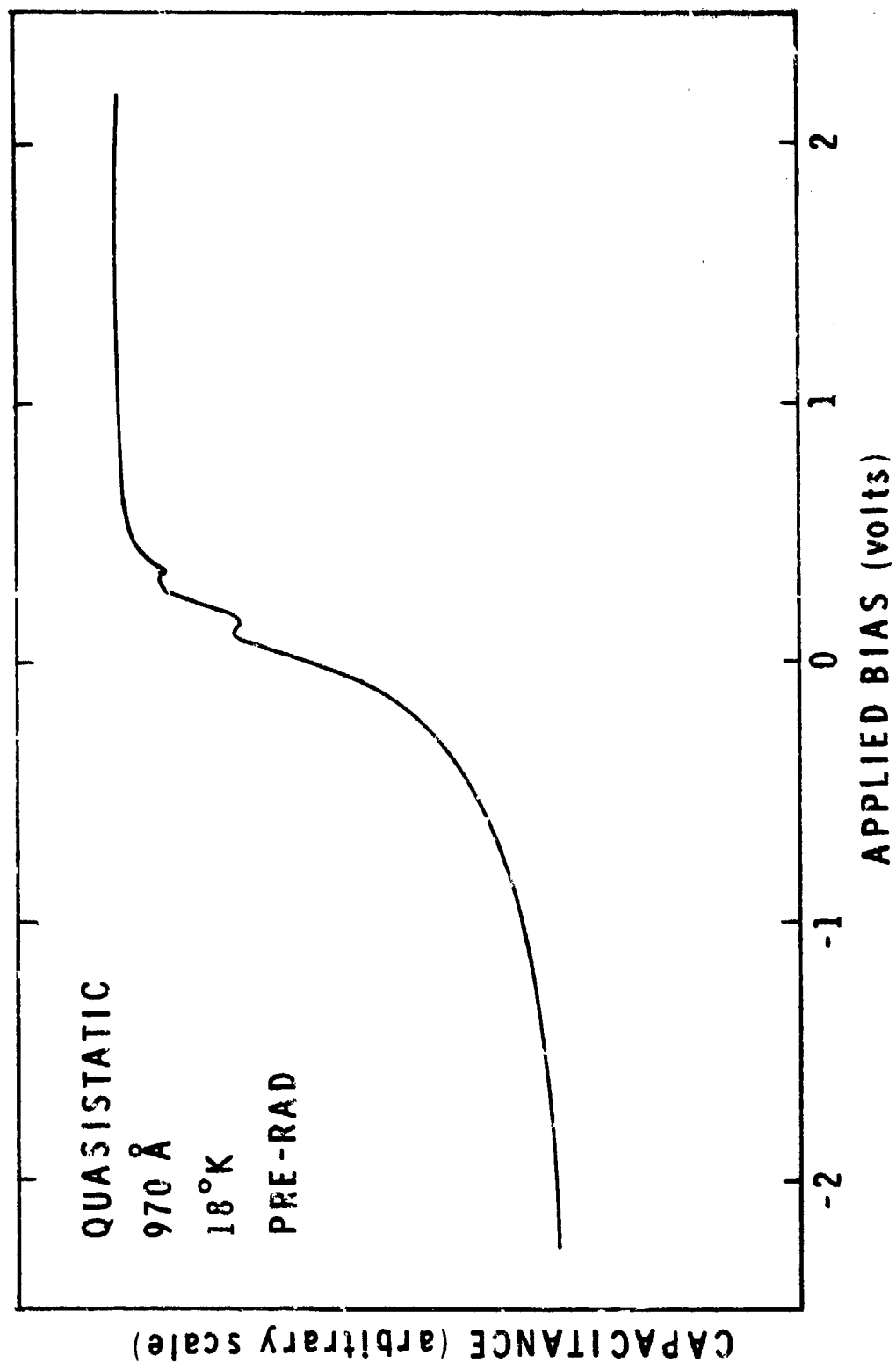


Figure 2-7. Quasistatic CV measurement at 18°K before irradiation.

Table 2-1. Comparison of 3-Hz and quasistatic measurements of flatband voltage shift at 20°K after a 10⁴-rad irradiation at 4°K.

Device #	Applied Field	Flatband Voltage Shift (Volts)	
		Quasistatic	3-Hz
1	1.06 x 10 ⁶	1.53	1.55
2	2.12 x 10 ⁶	1.82	1.79
3	3.2 x 10 ⁶	1.72	1.70
4	4.26 x 10 ⁶	0.74	0.78

A second measurement was therefore made, in which the quasistatic data were taken at the lowest convenient temperature. Under conditions of a sweep rate no less than 100 mV/sec, hysteresis in the quasistatic CV curve mandated an operating temperature of no less than 18°K. Results obtained under these conditions are shown in Table 2-2, where they are compared to 3-Hz data taken at 20°K before and after irradiation. After the latter measurement, the quasistatic value was again obtained at 18°K. The data are once again in good agreement, although in this instance the 3-Hz value of flatband shift tends uniformly to be somewhat smaller than the quasistatic value. That this is unrelated to charge rearrangement between 18 and 20°K is confirmed by the reproducibility of the quasistatic measurements performed both before and after the 3-Hz measurement at the higher temperature (Table 2-1). We may therefore conclude that the results of measurement at 18°K are identical to those obtained at 20°K. The range of electron trap energy levels which could be effective in charge buildup is thus even further restricted.

Table 2-2. Additional comparison of 3-Hz and quasistatic measurements of flatband voltage shift (dose = 10⁴ rads (Si)).

Device #	Applied Field x 10 ⁶ V/cm	Flatband Voltage, V _{FB}					ΔV _{FB}	
		Pre-Rad		Post-Irradiation				
		3-Hz (20°K)	Quasi- static (18°K)	Quasi- static (18°K)	3 Hz (20°K)	Quasi- static (18°K)	Quasi- static (18°K)	3-Hz (20°K)
1	1.61	-.150	-.151	+1.51	+1.47	+1.50	1.66	1.62
2	2.12	-.120	-.129	+1.61	+1.57	+1.60	1.74	1.69
3	2.68	-.062	-.153	+1.69	+1.68	+1.69	1.84	1.74
4	3.23	-.184	-.190	+1.43	+1.41	+1.43	1.62	1.59

2.2.3 Direct Measurements of Flatband Shift at 4°K

The first experimental attempt to perform a 4.2°K experiment utilized the fact that majority carrier charge for sensing the transition between accumulation and depletion can be made available from the charge stored at the interface under accumulation bias conditions. The experimental method is as follows: The capacitor is brought to equilibrium in accumulation prior to irradiation by momentarily raising the sample temperature to 19°K under accumulation bias. The sample temperature is then lowered to 4.2°K. As the temperature is decreased, the majority carriers freeze out throughout the silicon bulk, but the accumulation charge remains in the conduction band in a thin region, on the order of 100 Å or so, at the surface. To establish the pre-irradiation flatband voltage, the bias is swept from accumulation to inversion. At flatband, all of the majority-carrier charge in the accumulation layer will have diffused into the silicon bulk, and the resulting current transient can be sensed in the external circuit in the usual configuration for quasistatic capacitance measurement. Once the charge has dissipated, however, it cannot be restored (in finite time!) at that temperature, so the measurement is one-shot. After restoration of the appropriate accumulation bias, irradiation of the sample is initiated. The capacitor may either be brought to equilibrium charge distribution again at 19°K prior to irradiation at 4°K, or the irradiation may proceed directly at the latter temperature, in that the carriers generated by the irradiation will restore the capacitance to equilibrium in accumulation promptly.* After irradiation, the flatband voltage may again be sensed by sweeping the bias once from the irradiation bias to depletion.

* The statement that such equilibration does take place under gamma irradiation is closely allied with the earlier assertion that the applied bias is dropped entirely across the oxide even in the carrier freeze-out temperature regime. That this is in fact the case was demonstrated by an experiment in which the charge transport through the oxide was measured under bias at the prevailing gamma dose rate. A current of 2.5×10^{-10} A was measured at 41.3V bias (4.26×10^6 V/cm). This implies an effective insulator resistance of 1.65×10^{11} ohms. Since the observed current is far larger than that which could arise from carrier generation within the oxide, it is in fact dominated by currents generated within the associated cabling and sample mounts, which are likewise exposed to the gamma source. Thus, the above value of resistance represents an overestimate of the induced conductivity of the oxide. Turning now to the silicon, the observed dielectric relaxation frequency of 120 Hz indicates a resistance of 10^7 ohms. The resistance ratio of greater than 10^4 implies that the bias is applied exclusively across the oxide. A second argument can be given from the data themselves. The agreement of the bias dependence of flatband shift at 4°K with that at 77°K is proof, a posteriori, that identical bias conditions must have existed across the oxide in both cases.

In an initial measurement of the pre-irradiation flatband voltage by this method, results were found to differ from our expectations in several respects. In the first place, the observed signal was found to be considerably smaller than expected. The current waveform was therefore dominated strongly by capacitor displacement current. The capacitor dielectric in this case consists not only of the SiO_2 but of the silicon bulk, yielding a total device capacitance somewhat less than 1 pF. To compensate this displacement current, a bucking circuit was added, and the resulting experimental design is illustrated in Figure 2-8. Data obtained with this circuit are shown in Figure 2-9, where curve (a) shows the current waveform after the interface has been brought to equilibrium in accumulation, and curve (b) shows a subsequent trace in which accumulation charge is absent. The difference between the two curves is due to the accumulation charge, and the bias at which the charge disappears should yield the flatband condition. The magnitude of the observed charge was found to be considerably less than that which would be observed if the majority carriers were to transit the whole silicon bulk. One possible explanation for this is in terms of trapping of the majority carriers in ionized donor sites. A certain concentration of compensating acceptors inevitably exists in the material, and an equal concentration of shallow donors will therefore have yielded their charge to these compensating sites. A good estimate of such compensation in Czochralski material is $3 \times 10^{13} \text{ cm}^{-3}$. The capture cross section at ionized donor sites is quite large,¹⁸ so that carriers are readily trapped. Numerically, it is found that the charge released from the interface is approximately equal to the number of ionized donors, under the above estimate. The mean transit distance of carriers is therefore predicted to be on the order of one-half of the silicon thickness. The observed signal current was small compared to the value expected on this basis, and other mechanisms must be operative. It is possible, for example, that mobile carriers are trapped not only at ionized donor sites but also at neutral sites, leading to a shorter transit distance. The result in any event is the buildup of space charge in the silicon, since the detrapping times are large compared to experimental time scales. The measured flatband voltage is thus determined as much by the fixed charge existing within the silicon as that existing within the oxide. It becomes clear that this experiment requires more refined treatment. Such analysis would have been performed but for the availability of a more direct experimental option. Under the circumstances, this experimental approach was abandoned, and is

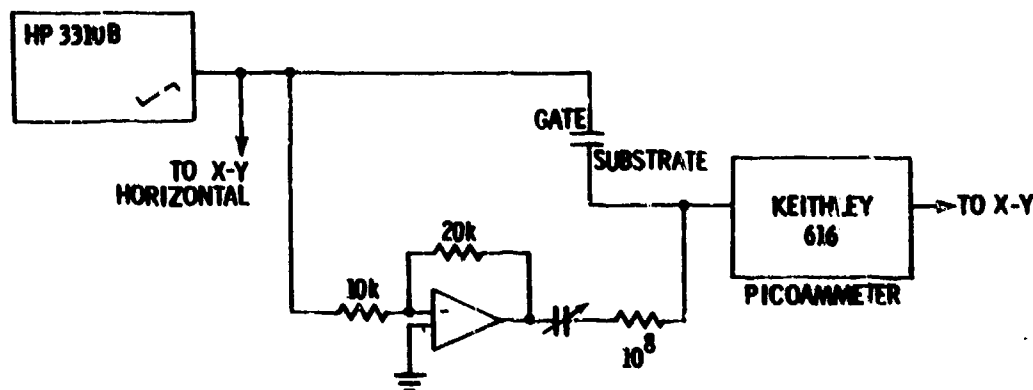


Figure 2-8. Schematic diagram of the experimental method for measuring flatband voltage utilizing accumulation charge. The method is essentially a quasistatic measurement with a bucking circuit to compensate for the prevailing displacement current transient.

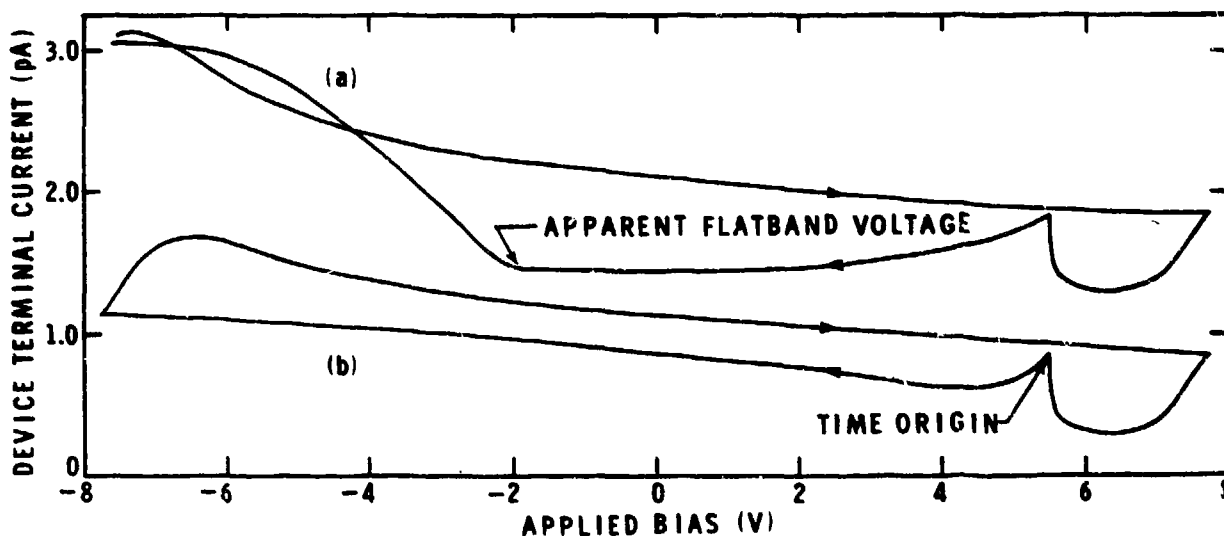


Figure 2-9. Quasistatic measurement of flatband voltage at 4°K using accumulation charge. Shown are results with accumulation charge present (Curve a) and without such accumulation charge (Curve b). The difference in curve shapes is ascribed to the accumulation charge, and the break in the curve taken to yield the flatband voltage.

reported here for the reason that it does constitute a useful tool for the characterization of semiconductors in the freezeout regime when suitably analyzed.

An unambiguous method of establishing whether electron trapping exists at 4°K which is unobservable at 18-20°K consists in measuring any charge transport which occurs under bias as the sample temperature is raised to the higher temperature after irradiation. This relatively more straightforward method was employed to ascertain that no significant electron trapping occurred in these oxides at 4.2°K. The experimental method consisted in irradiation of capacitors under bias, with maintenance of the bias as the source is lowered (i.e., dose rate \rightarrow zero), and subsequent measurement of charge transport as the sample temperature is raised from 4 to 20°K. The sample bias is held constant throughout. A Keithley 616 was used in the charge integration mode to yield charge directly; also, current was measured using a Burr-Brown 3523L electrometer operational amplifier. The total charge ρ (coul/cm³) generated by an ionizing dose γ (rads (Si)) in the oxide can be calculated from the known pair creation energy of 18 eV. The relationship is⁴ $\rho = 1.26 \times 10^{-6} \gamma$. At the applied bias of about 25V used in this experiment, nearly all of this charge would be collected in the absence of trapping; i.e., the probability of geminate recombination is small.⁴

In the first experiment, four capacitors were connected in parallel to enhance the signal-to-drift ratio. The devices were exposed to a dose of 5×10^3 rads(Si). The maximum possible trapped electron charge therefore amounts to about 9×10^{-10} C. If all of this charge were to be transported through the oxide, the charge measurement in an external circuit would be half of this, or 4.5×10^{-10} C. The amount of charge actually measured when the temperature was raised came to about 7×10^{-12} C. If this residual charge were indeed due to electron trapping, the trapped fraction is clearly too small to be of practical significance. It is not in fact possible to ascribe the observed charge exclusively to electrons released from traps during the temperature excursion since it is known that a hole trap distribution exists, and it is possible that some holes are released from shallow traps as well. So the measured charge places an upper limit on the possible electron trapping, and this limit is indeed a very low one.

Since this experiment was critical to our conclusions, it was subsequently repeated with fresh devices. Irradiation was to 10^4 rads (Si), and the charge transport observed on a single device amounted to 4×10^{-12} C, or 1.8% of the maximum possible charge. A measurement of another capacitor on the same chip after an additional irradiation yielded a value of 9.4×10^{-12} C. Although the quantity of charge measured is not highly reproducible, the conclusion remains firm that electron trapping on the time scale of the experiment (20 minutes) is insignificant. This experimental method would be quite useful to examine the possibility of radiation-induced shallow electron traps, by extension of the measurement to larger doses, but this was not done.

An additional experimental method for CV-measurement at 4°K was pursued in our desire to make the experiment as direct as possible, and the conclusion rigorous. Advantage was taken of the fact that the carrier concentration required to perform low-frequency CV-measurements can be generated by the ionizing radiation itself. The generation rate of the Co-60 gamma source was 3×10^{14} carriers/cm³ sec for our conditions, and with an estimated carrier lifetime of 10^{-10} sec (both majority and minority carrier lifetimes need to be considered here), a carrier concentration of 3×10^4 cm⁻³ was estimated, leading to the expectation of a rather low dielectric relaxation frequency (about 7 Hz). Initial measurements were therefore made under gamma irradiation with an excitation frequency of 1 Hz using the Ithaco 391A lock-in. The conditions of measurement were not auspicious, since gamma irradiation of the long cable runs to the sample holder gave rise to considerable noise. The resulting CV-curves were not promising for the recovery of flatband voltage. Operation at the low frequency of 1 Hz is expected to yield the typical low-frequency capacitance curve, in which the minority carriers are able to maintain equilibrium with the modulation in inversion, resulting in the observation of the oxide capacitance both in accumulation and in inversion. Measurements at higher frequencies were expected to yield the high-frequency capacitance, and this was confirmed. Signal-to-noise ratios also improved at higher frequencies. To establish the magnitude of the dielectric relaxation frequency under the given generation rate, measurements were then made of the capacitance signal in accumulation as a function of frequency using the Ithaco 395 lock-in, and the results are shown in Figure 2-10 for the frequency regime of 5 Hz to 2 kHz. The fit to the data indicates a dielectric relaxation frequency of about

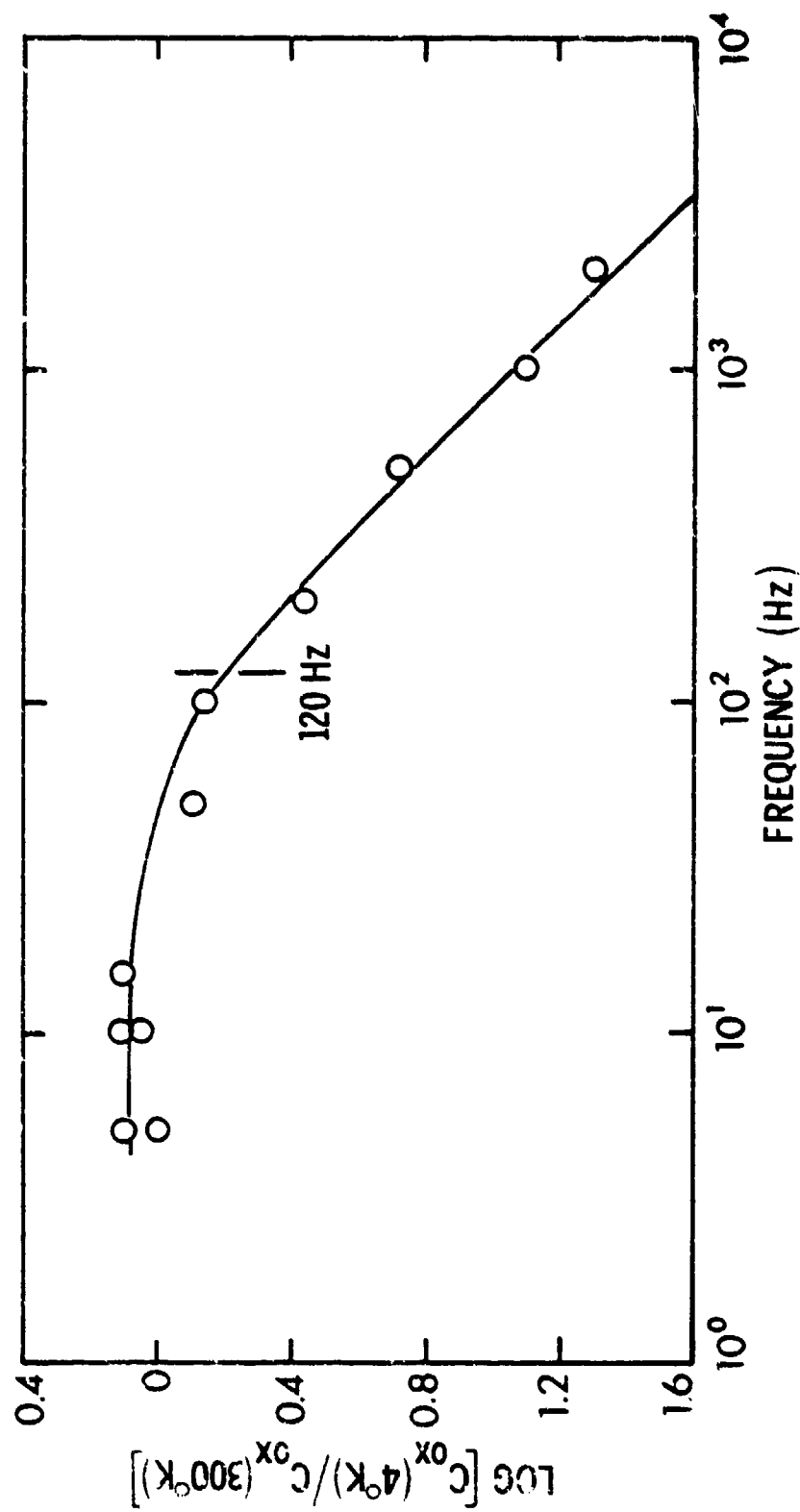


Figure 2-10. Magnitude of the capacitance signal as a function of modulation frequency.
This plot permits determination of the dielectric relaxation frequency.

120 Hz. Measurements were therefore made of CV-curves using 100 Hz modulation, and the curves obtained were free of significant noise.

Values of shifts in the flatband voltage at 4°K obtained using the above technique were found to be lower than those obtained using the conventional 3-Hz CV-measurement at 20°K. Comparisons were made for two oxide thicknesses and for a number of gate biases. The observed shifts ranged from 0.60 to 0.83 of the corresponding conventionally measured values. The possibility existed that the measurement method involved a certain constant error, and one irradiation was therefore performed to a dose of 4×10^4 rads to yield a larger absolute shift. The 4°K measurement again yielded a value which was about 0.83 of the conventionally measured one. These results prompted the revival of the hypothesis that some electron trapping might have been present and responsible for this reduction in net charge buildup. An additional experiment was therefore undertaken to resolve this conflict with our previous findings. It was supposed that since the experimental method employed here is unconventional, some difficulties relating to the method itself might have given rise to the discrepancy.

A sequence of measurements was made post-irradiation in which the flatband voltage was first measured under gamma excitation at 4°K, then the sample temperature was raised to 20°K and the flatband voltage remeasured conventionally. Finally, the temperature was once again dropped to 4°K, and the source raised to remeasure the flatband voltage at 4°K. Results of this sequence of tests are shown in Table 2-3 for two runs. The flatband shifts measured at 4°K are once again smaller than those measured at 20°K, but the significant finding is that these lower values are reproduced after the sample has been taken to 20°K, and any (hypothetically) trapped electrons have been released. The explanation for the observation of a lesser shift at 4°K therefore must lie elsewhere than with electron trapping, and our earlier conclusion stands confirmed. It may be noted that whereas the flatband shift at 4°K was reproduced very well before and after the "anneal", the reproducibility from run to run is quite poor. The randomizing variable has not been identified and the issue was not pursued since the principal purposes of the experiment had been accomplished. Some additional comments on this technique are in order, however.

Table 2-3. Sequential measurement of flatband shifts at 4°K and 20°K.

First Run:

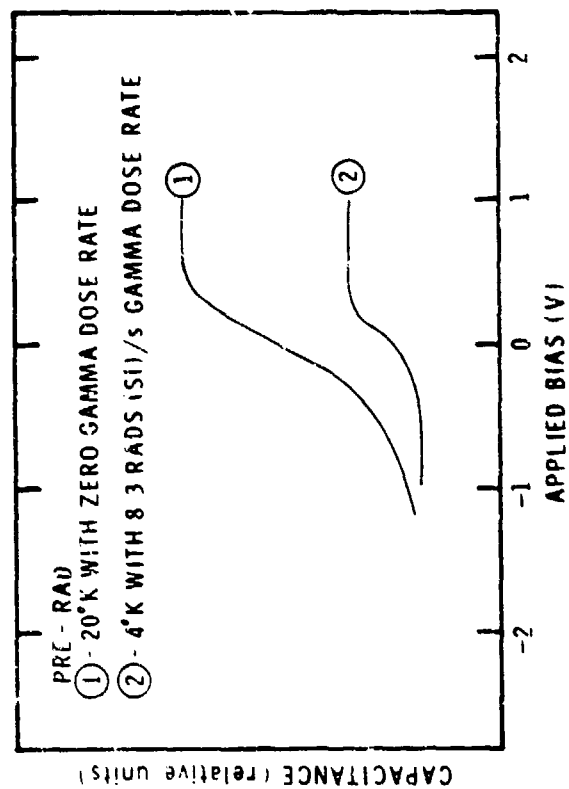
1. ΔV_{fb} (4°K, under gamma excitation, 100 Hz): 1.060V
2. ΔV_{fb} (20°K, thermal excitation, 100 Hz): 1.275V
3. ΔV_{fb} (4°K, under gamma excitation, 100 Hz): 1.060V

Second Run:

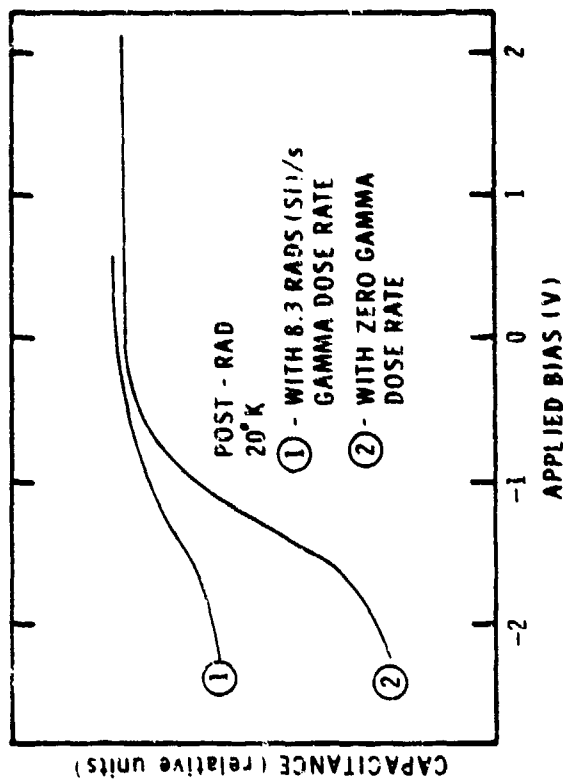
1. ΔV_{fb} (4°K, under gamma excitation, 100 Hz): 0.762V
2. ΔV_{fb} (20°K, thermal excitation, 100 Hz): 1.077V
3. ΔV_{fb} (4°K, under gamma excitation, 100 Hz): 0.762V

It had been clear from the outset that this experimental approach was fraught with pitfalls. The gamma dose rate is clearly sufficient to affect the capacitance-voltage curve by charge-up of existing interface states. If the difference in observed flatband shift may be ascribed to such effects, then it is not unreasonable to suggest that a dose rate does exist which on the one hand permits CV-measurements to be made at tractable modulation rates, and on the other hand produces only small perturbations of the capacitance-voltage relationship. If a dose rate on the order of 10% of the prevailing dose rate had been used, for example, an operating frequency of 30 Hz would still have been feasible, and the prompt--as opposed to cumulative--effects of the gamma dose rate on the observed flatband condition would be reduced an order of magnitude, to quite manageable proportions. This is particularly true when it is noted that one need not operate with such small flatband shifts as those to which we have restricted ourselves in this experiment. Unfortunately these speculations were not tested, but are nevertheless presented as a possible avenue for the examination of oxides under carrier-freezeout conditions.

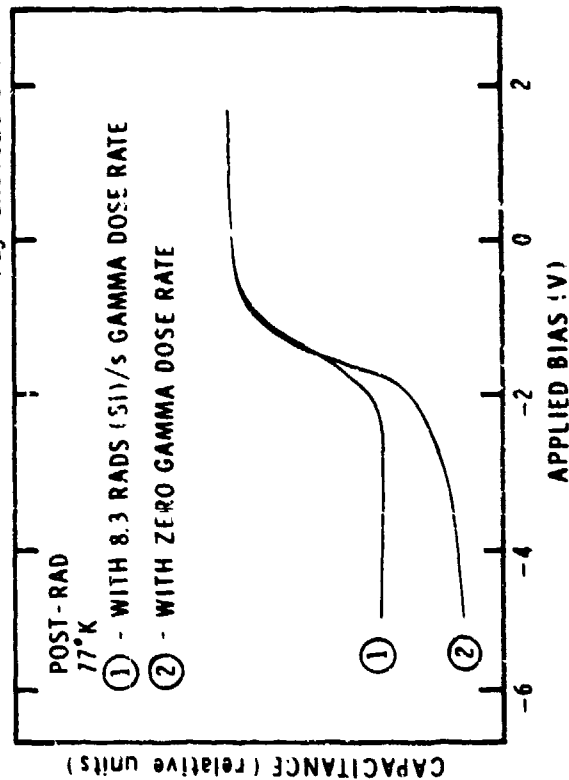
In an attempt to understand gamma-ray effects on capacitance-voltage relationships, measurements with and without gamma excitation were compared at various temperatures, and the results are shown in Figure 2-11. In Figure 2-11a, comparison is made of a CV curve obtained at 4°K under gamma irradiation with a 20°K CV curve obtained without gamma irradiation. The flatband voltages in both cases are approximately the same in this pre-irradiation measurement. The signal amplitude in accumulation is not the same in the two cases, however, despite the use of an identical modulation amplitude and the use of a modulation frequency



(a) Data obtained at 4 and 20°K with and without gamma-ray excitation.



(b) Data obtained at 20°K with and without gamma-ray excitation.



(c) Data obtained at 77°K with and without gamma-ray excitation.

Figure 2-11. Comparison of CV curves obtained at various temperatures under differing measurement conditions.

(100 Hz) less than the dielectric relaxation frequency. This could be due to voltage division between the silicon bulk resistance and the lock-in amplifier input impedance, but that possibility was not checked. When CV measurements made at 20°K with and without gamma excitation are compared (Figure 2-11b), a broadening of the capacitance step is observed which is indicative of charge-up of interface and/or bulk states that are susceptible to charge exchange on the experimental time scales. The curve obtained under gamma flux has the character of a low-frequency CV curve, so that the inversion capacitance is never exhibited. When 1-MHz CV measurements made at 77°K with and without gamma excitation are compared (Figure 2-11c), the effect of the gamma flux is simply to maintain the inversion layer in equilibrium.

2.2.4 Oxide Thickness Dependence of Charge Buildup

Using the conventional low-frequency capacitance method described above, samples with identically grown oxides but different oxide thickness were characterized in terms of flatband voltage shift as a function of gate bias. (Wafers were etched back to obtain the different oxide thicknesses.) The results are shown in Figure 2-12. The scatter is indicative of the experimental resolution under the given conditions of long cable runs, etc. The thickness dependence of the maximum rates of charge buildup is shown in Figure 2-13, where data points corresponding to a field strength of 2.8×10^6 V/cm are replotted from Figure 2-12. The observed thickness-squared dependence is consistent with uniform charge buildup within the oxide, as is characteristic of higher-temperature behavior as well (prior to significant hole transport).

The maximum charge buildup which is expected to occur if all the holes are trapped in the oxide near their point of generation and all the electrons are swept out may be determined as follows.⁴ For uniform charge distribution, the shift in flatband voltage ΔV_{fb} is given by

$$\Delta V_{fb} = \left(\frac{q}{2\epsilon} \right) t_{ox}^2 \quad (1)$$

The maximum number of free electron-hole pairs induced by a given dose is 7.9×10^{12} pairs/cm³ rad (employing 18 eV per pair). We therefore obtain

$$\Delta V_{fb} = 1.8 \times 10^6 \gamma t_{ox}^2 \quad (2)$$

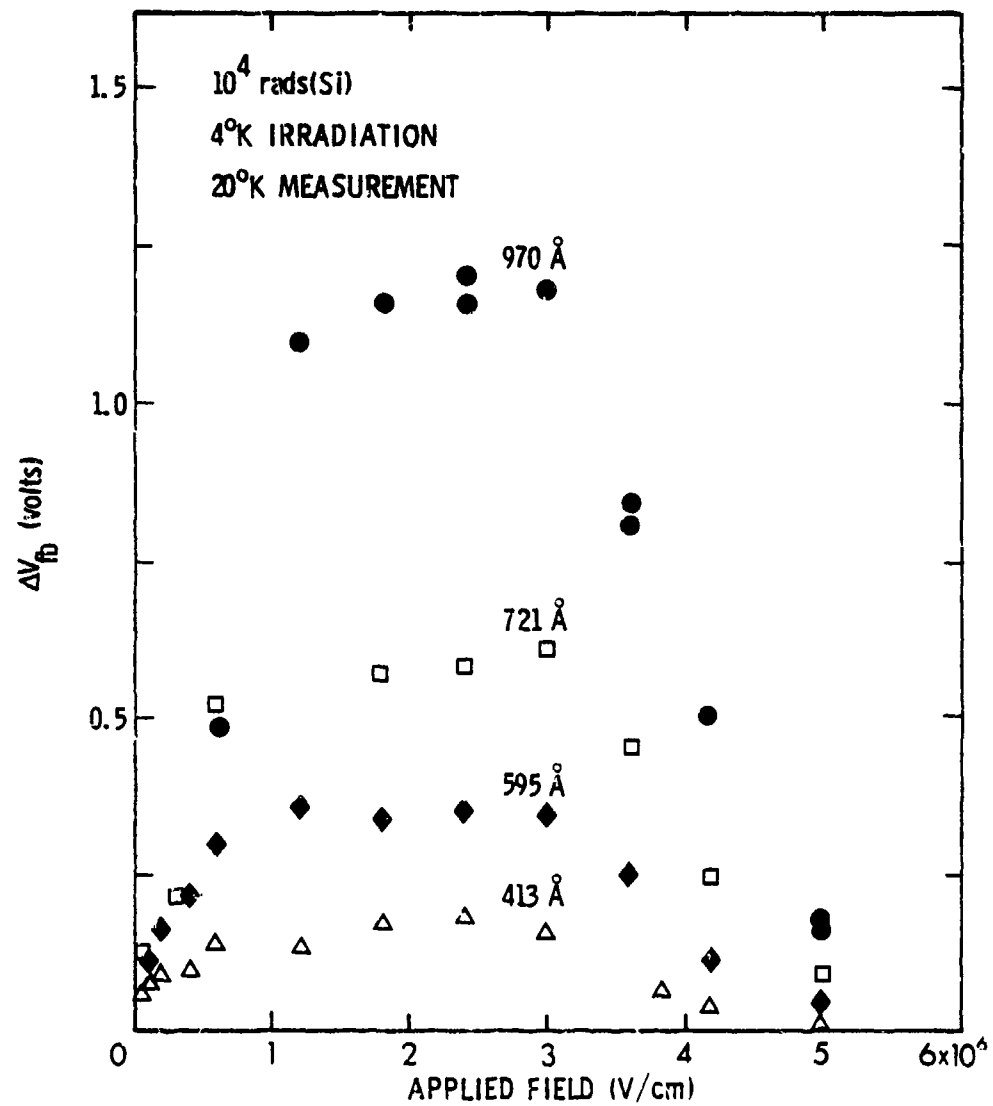


Figure 2-12. Flatband voltage shift as a function of field applied during irradiation for MOS capacitors with various oxide thicknesses. Irradiations were performed at 4°K and CV measurements then made at 20°K .

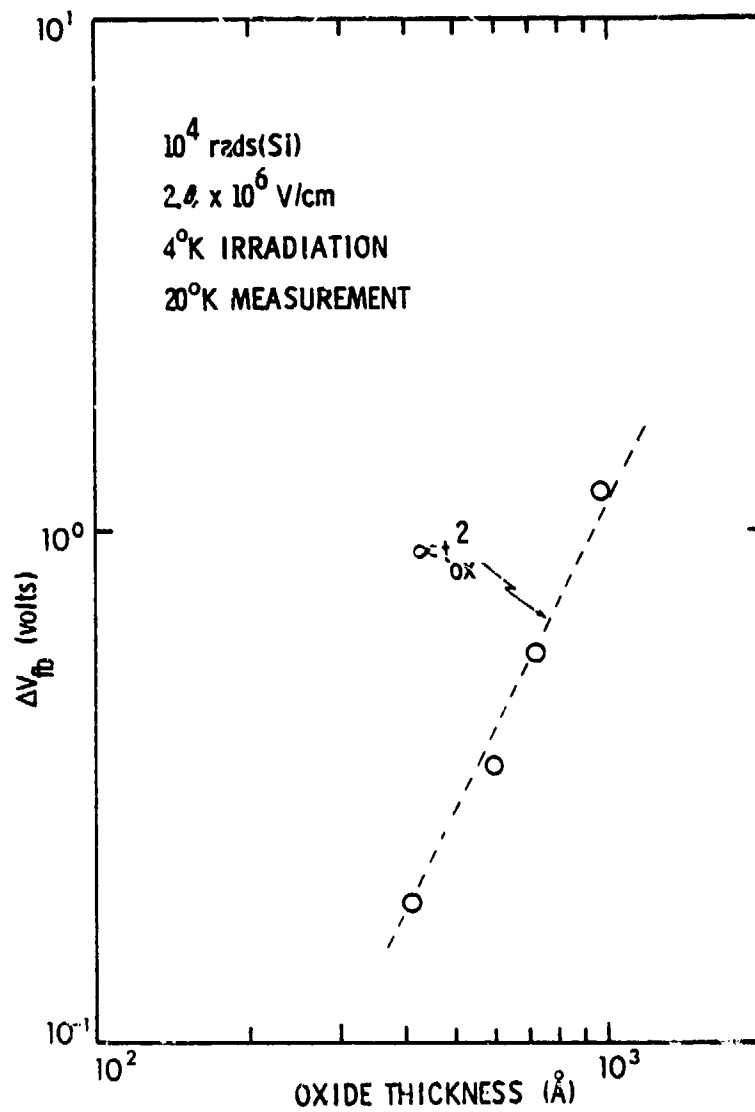


Figure 2-13. Flatband voltage shift at $2.4 \times 10^6 \text{ V/cm}$ as a function of oxide thickness (derived from Figure 2-12).

For an oxide thickness of 970 Å, this yields a maximum possible shift of 1.71V for a dose of 10^4 rads(Si). The observed maximum shifts of 1.25V in Figure 2-12 and 1.45V in Figure 2-2 are somewhat less than the maximum possible value due to field-induced transport of charge on the time scale of the measurement, which is already significant at field strengths of 3×10^6 V/cm. Previous modeling of such hole transport data⁴ at 77°K also indicates that the charge yield is less than 100% at this field strength. The net effect is that a charge of about 80% of the maximum value is expected, or a peak flatband shift of about 1.4V. The data are in reasonable agreement with this expectation.

The data of Figure 2-6 indicate a much larger flatband voltage shift than the two figures discussed above. The peak value of about 1.9V is clearly in excess of the maximum theoretical shift. A scale factor error is indicated, since the data are otherwise well-behaved. The principal point here is the correspondence between the 4°K and the 77°K data, the latter being well understood, and this purpose is still served despite any uncertainty in scale factor.

Dosimetry for all measurements was performed by means of an ionization gauge calibrated for Co-60 gammas. The gauge was placed at the sample position in the absence of the dewar, and the absorption by the dewar needed to be determined. This was accomplished in two ways. First, the absorption was measured by means of TLD's, and determined to be 11%. In view of the uncertainty in TLD dosimetry, which was taken to be 10%, this value is not too meaningful. A second measurement was made using charge buildup itself as a dosimetric technique. Charge buildup was measured in the experimental samples at 77°K at 1 MHz in the helium dewar, and the measurements were repeated in a glass dewar, for which the absorption was negligible ($\leq 2\%$). By this latter method, the dewar absorption factor was found to be negligible as well, and this latter measurement was accepted as the more accurate.

A second measurement was made to ascertain whether dose enhancement prevailed at the sample position. The sample had originally been covered with a thin (30 mil) layer of aluminum to assure dose equilibrium, but a small hole had been cut into the shield to admit the optical signal during the early runs. The helium exchange gas chamber was made of stainless, so the possibility of some dose enhancement could not be overlooked. An additional run was made, therefore, in which the aluminum shield was replaced with one without an aperture, and identical results in terms of flatband shift were obtained.

2.3 DISCUSSION AND CONCLUSION

It is the compelling conclusion of the present work that charge buildup at 4°K in irradiated SiO₂ films can be described exclusively in terms of the hole trapping behavior which has already been successfully modeled at higher temperatures (notably 77°K).^{4,5} Strictly speaking, this conclusion should be modified to apply specifically to the case of the wet oxides studied and to the particular irradiation conditions (steady-state ionizing radiation--20 minute time scale). It remains a possibility that significant electron trapping may be observed on shorter time scales, and this is a matter which should be further investigated. It seems highly likely on general principles that trap-limited electronic conduction should be observed on some time scale at these low temperatures. If this time scale is sufficiently long, it would still be of technological interest as a means of compensating for trapped holes on that time scale.

It has not been mentioned thus far that shallow electron traps in oxides have been the subject of study by others. Most recently, shallow neutral electron traps have been studied in SiO₂ films by thermally stimulated current measurements.¹⁹ The distribution in energy of such traps was found to be about 300 meV below the conduction band, with an uncertainty of about 50 meV, and a half-width of the distribution of about 200 meV. These findings are not in conflict with those reported here. The electron traps in question have very low capture probabilities, and were found under conditions of electron injection which exceeded by three to four orders of magnitude the charge generated in the present penetrating-irradiation experiments. Under conditions in which both electrons and holes are available for trapping, we have found the residual trapped electron charge after a 20-minute low-temperature irradiation to be a small fraction (no more than about 4% in the present oxides) of the trapped hole charge. As a final point, we have raised the possibility that electron trapping and transport in SiO₂ may be dependent on oxide processing. This possibility should be considered in further studies.

SECTION 3.0

MECHANISMS OF RADIATION EFFECTS ON EXTRINSIC SILICON DETECTORS

3.1 INTRODUCTION

Extrinsic silicon detectors are becoming technologically important because of their suitability for the fabrication of monolithic focal plane arrays. By appropriate choice of dopant, the desired spectral region can be covered, ranging from the 1-2 μm range for the deep gold level to about 30 μm for arsenic or boron. Operation of the detectors is confined to the temperature regime in which the carriers are substantially frozen out, which ranges from slightly below 0°C for the gold acceptor, to about 10°K for boron and arsenic.

Extrinsic silicon detectors make it possible to take advantage of the well-established silicon integrated circuit fabrication technology to incorporate both detector elements and associated readout electronics in a monolithic structure. Intrinsic detectors, by contrast, generally require coupling of the optically generated signal into silicon readout devices, such as CCD's. Progress is being made in the development of MIS technologies for InSb and other candidate intrinsic detector materials, which would permit monolithic focal plane arrays using these other materials. However, the criteria which must be satisfied by a charge-coupled device suitable for the infrared are far more stringent than those which apply in the visible region, and the problems in that case have been formidable enough. The reason for this is simply that the signal of interest is generally a small perturbation on the total, or background, optical signal. As an example, in thermal imaging, small temperature differences must be made discernible, and thus comparably small differences in optical flux must be measurable. A 1°K temperature difference yields a 1.8% difference in photon flux at a detector sensitive out to 12 μm , for example. If a 100-element CCD is envisioned to couple out the detected signal sequentially, then the requirements on permissible carrier transfer inefficiency are manifestly stringent. Thus, there is considerable interest in extrinsic silicon detector arrays.

This section describes results of an investigation of the mechanisms of radiation effects on extrinsic silicon detectors. The work reported here

constitutes the beginning of an effort that will continue in a subsequent program during 1979. We first provide a background discussion of radiation effects on extrinsic silicon, followed by presentation and discussion of experimental results.

3.2 BACKGROUND

Radiation effects on extrinsic silicon detectors are best discussed in terms of the various optical and transport parameters governing operation of such devices, and we review these briefly. For specificity, the discussion will be in terms of zinc as a dopant. Zinc introduces an acceptor level at about 0.31 eV above the valence band, as established by means of carrier concentration versus temperature measurements. At temperatures sufficiently low, the zinc levels are substantially unionized, and susceptible to optical excitation of holes into the valence band. This is shown schematically in Figure 3-1. The probability of optical absorption and resultant carrier excitation is referred to as the quantum efficiency, $\eta(\lambda)$, and is given in terms of the optical absorption coefficient, $\alpha(\lambda)$, and the reflection coefficient, $r(\lambda)$, by the equation

$$\eta(\lambda) = \frac{(1 - r(\lambda))(1 - e^{-\alpha(\lambda)d})}{1 - r(\lambda) e^{-\alpha(\lambda)d}} , \quad (1)$$

where d is the sample thickness. This equation is straightforwardly derived under the assumption of normal incidence, uncoated surfaces, and with inclusion of multiple internal reflections. The absorption coefficient, in turn, is given by

$$\alpha(\lambda) = \sigma(\lambda) N_{\text{Zn}^0} , \quad (2)$$

where $\sigma(\lambda)$ is the spectral photoionization cross section and N_{Zn^0} is the number density of unionized zinc impurities. Photoionization cross sections typically fall in the range of 10^{-15} to 10^{-17} cm^2 , and the solubility limits for typical desirable dopants typically fall in the range of 10^{15} - 10^{17} cm^{-3} , so that absorption lengths at the peak response wavelength tend to fall in the range of 0.1-10 mm for practical impurities. For simplicity, we may assume that the sample thickness is less than the absorption length, and that the absorption

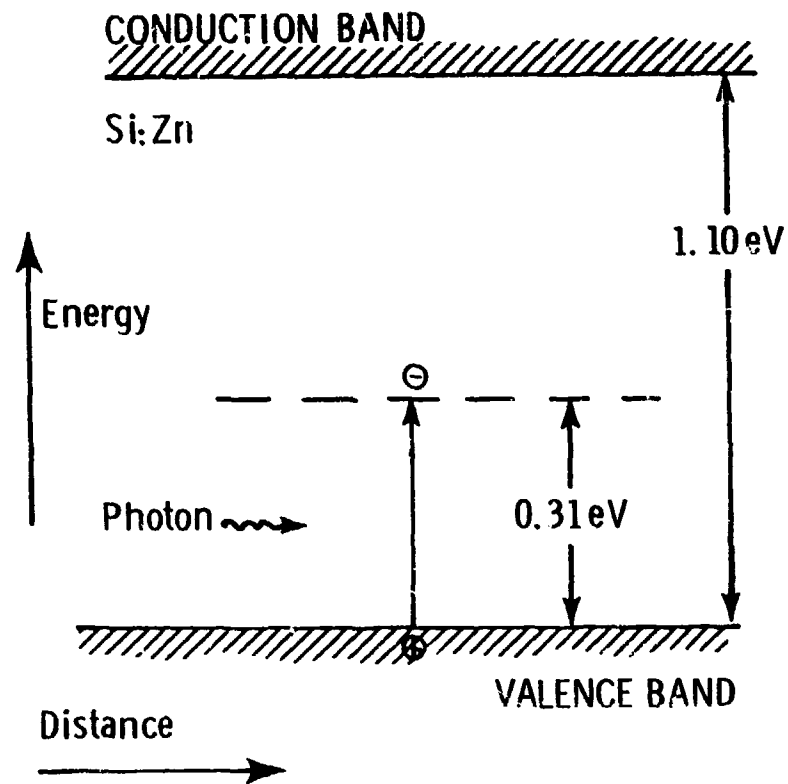


Figure 3-1. Band diagram for the lowest acceptor state of zinc in silicon. (A second, deeper acceptor state exists when this level is filled.)

is thus uniform throughout the sample. The quantum efficiency then reduces simply to

$$\eta(\lambda) = \sigma N d . \quad (3)$$

The optically excited carriers, majority carriers in this case, undergo transport under an applied field E by an amount given in the mean by the Schubweg, or transit distance, $\mu\tau E$, where μ is the carrier mobility and τ the majority carrier lifetime. If the contacts on the sample are nonblocking and injecting, then majority carriers swept out at one electrode may be replaced at the other, so that the excited carriers contribute up to their whole Schubweg to the transport even if it exceeds the sample thickness. A photoconductive gain G is thus defined, given by $(\mu\tau E)/d$, where d is the separation between electrodes. The quantum yield is then defined as the ratio of the number of mobile carrier transits across the photoconductor to the number of incident photons. Under the assumption that the sample thickness is considerably less than the absorption length, and the absorption thus uniform throughout the sample, the quantum yield is given by

$$\text{Quantum Yield} = \eta G = \eta \mu \tau E / d . \quad (4)$$

A related quantity in terms of which detectors are typically characterized is the current responsivity, R_I , which is the device signal current normalized to incident optical power:

$$R_I(\lambda) = q \eta(\lambda) G / h\nu = q \lambda \eta(\lambda) G / hc , \quad (5)$$

where h is the Planck's constant, c is the velocity of light, and $h\nu$ is the energy of the incident photon of wavelength λ .

To permit observation of the photoinduced carrier density, detectors are operated in the carrier freezeout regime in which the thermally generated carrier concentration is less than or equal to that generated by the background photon flux. The theoretical limit imposed on the detection of an optical signal superimposed on the optical background is given by generation-recombination (g-r) noise in the detector. This noise source derives from the statistical fluctuation in generation-recombination events, and the statistics are

independent of whether the generation process is predominantly thermal or optical. Under conditions in which the optically induced carrier density dominates the thermally induced density, the operation of the detector attains its limiting, i.e., background-limited (BLIP), value. A concrete treatment of g-r noise must be based on certain assumptions with regard to detector specifications, to which attention is now turned.

In general, extrinsic silicon detectors for thermal imaging in the 8-14 μm regime employ one of the shallow III-V dopants, such as arsenic. Residual acceptors in such material act to compensate, or ionize, the intentional donor impurity, reducing the concentration available for photoionization, and decreasing the carrier lifetime since all the ionized donor sites are recombination (or, preferably, trapping) sites for excited majority carriers. The majority carrier lifetime is thus given, to good approximation, by

$$\tau = \frac{1}{c_n N_{\text{As}^+}} = \frac{1}{\sigma_n v_{\text{th}} N_{\text{As}^+}} \quad (6)$$

for the assumed case. Here c_n is the capture probability at ionized arsenic sites, the concentration of which is given by N_{As^+} , σ_n is the capture cross section, and v_{th} the thermal velocity. As a practical matter, boron is the principal residual acceptor impurity in such material, and the ionized donor concentration is approximately equal to the residual boron concentration.

For the case of a practical arsenic-doped detector, therefore, the carrier concentration temperature dependence may be described in terms of a two-level model involving merely the intentional donor level of concentration N_D and the residual acceptor level, of concentration N_A . The charge balance equation yields²⁰

$$\frac{n_0 (n_0 + N_A)}{\beta N_C (N_D - N_A - n_0)} = \exp(-E_a/kT) \quad (7)$$

Here E_a is the ionization energy of the donor level, N_C is the conduction band density of states, β is the statistical weight of the donor level, and n_0 is the equilibrium carrier concentration at temperature T . In the freeze-out regime, this equation reduces to the simpler form

$$n_0 = \frac{N_C N_D}{\beta N_A} \exp(-E_a/kT) \quad (8)$$

The carrier concentration is seen to be governed by the ratio of donor to acceptor concentrations.

For deeper impurities, which are suitable for near-infrared detection, the above discussion needs to be modified only slightly. Referring again to the case of the zinc acceptor, it is clear that residual boron will dominate the carrier concentration temperature dependence unless it is completely compensated by a donor (typically shallow). Any excess compensation will serve to ionize the zinc level partially. If the intentional dopant concentration is sufficiently large compared to the residual boron dopant concentration, then a two-level analysis will once again be adequate. We have, in general,

$$\frac{\beta p_0 (p_0 + N_D)}{N_V (N_A - N_D - p_0)} = \exp(-E_a/kT) \quad (9)$$

which reduces at low temperature to the familiar form

$$p_0 = \frac{N_V N_A}{\beta N_D} \exp(-E_a/kT) \quad (10)$$

and at high temperature to

$$\frac{\beta p_0^2}{N_V (N_A - p_0)} = \exp(-E_a/kT) \quad (11)$$

where it is assumed that $N_A > p_0 \gg N_D$. Here N_D is the net compensation, given by $N_D = N_{As} - N_B$. In the extreme high-temperature limit, we have, of course, $p_0 = N_A$, independent of statistical weight (strictly speaking, $p_0 = N_A - N_D$). Intrinsic carrier concentration has been neglected.

The above equations reveal that a complete specification of the carrier concentration as a function of temperature yields the intentional dopant concentration, the concentration of compensating impurity, and the statistical weight. Hall measurements as a function of temperature are employed to yield this information, as will be discussed further below.

For extrinsic detector material which is partially compensated (this covers all cases of interest), van Vliet²¹ has shown that the spectral intensity of the fluctuations in device current which arise from the generation-recombination process is given per unit frequency interval by

$$S(f) = \frac{4I^2}{N_0} (1 - \xi) \left(\frac{\tau}{1 + \omega^2 \tau^2} \right) \quad (12)$$

where I is the quiescent sample current, N_0 is the total number of carriers undergoing transport in the sample, ξ is the fractional ionization, and ω the angular frequency. In the freeze-out regime ξ is negligible. The rms fluctuation of current in the time domain is given by

$$\langle i^2(t) \rangle = \int_0^\infty S(f) df = \frac{I^2}{N_0} (1 - \xi) \approx \frac{I^2}{N_0} \quad (13)$$

It is apparent from these equations that an explicit lifetime dependence is revealed only in the spectral dependence of the fluctuations, not in the rms value of the fluctuations in the time domain. The equations are applicable to the case of thermal imaging or near infrared detection, in which the quiescent carrier concentration is a well-defined quantity, i.e., the fluctuations are less than the mean value. For low-background applications, a different formulation is appropriate.

As a practical matter, almost all extrinsic silicon detectors currently under development are characterized by majority carrier lifetimes which are quite short, on the order of microseconds at best. (This excludes detectors which employ a doubly-charged acceptor, such as $Zn^{=}$, for photoexcitation). The frequency domain of interest is that given by frame times in a practical case, or by circuit RC limitations in the present experimental context. In either event, the domain of interest is less than 5×10^4 Hz, for which the condition $\omega\tau \ll 1$ is well satisfied. In this regime, the noise current in a bandwidth Δf about frequency f is given by

$$i_n^2(f) = S(f)\Delta f = \frac{4I^2\tau}{N_0} \Delta f \quad (14)$$

Substituting for the current in terms of N_0 and photoconductive gain G , we have

$$i_{n,rms} = 2qG \left(\frac{N_0}{\tau} \right)^{\frac{1}{2}} (\Delta f)^{\frac{1}{2}} . \quad (15)$$

The quiescent carrier concentration is comprised of a thermally generated component n_{th} and an optically generated component n_s , in terms of which we have

$$i_{n,rms} = 2qG \left(\frac{n_{th} + n_s}{\tau} \right)^{\frac{1}{2}} (V)^{\frac{1}{2}} (\Delta f)^{\frac{1}{2}} , \quad (16)$$

where V is the detector volume. It is seen to be physically immaterial whether the noise arises from thermally or optically generated carriers.

The limits of detection which are imposed by material parameters are generally expressed in terms of detectivity (D), the reciprocal of the noise equivalent power (NEP). The latter quantity is simply

$$NEP = i_{n,rms}/R_I ,$$

where R_I is the responsivity, given by Equation (5). The specific detectivity, or D^* , is defined as the detectivity normalized to unit area of illumination and unit bandwidth, giving

$$D^* = (NEP)^{-1} (A)^{\frac{1}{2}} (\Delta f)^{\frac{1}{2}} = R_I (A \Delta f)^{\frac{1}{2}} / i_{n,rms} . \quad (17)$$

Thus,

$$D^* = \frac{\lambda}{2hc} \eta(\lambda) \left(\frac{\tau}{n_{th} + n_s} \right)^{\frac{1}{2}} \left(\frac{1}{d} \right)^{\frac{1}{2}} . \quad (18)$$

Uniform absorption over the sample volume is assumed. The absence of photoconductive gain from this equation should be noted. This signifies that the limits of detection are influenced by photoconductive gain only insofar as amplifier noise is important. Under conditions of $n_s \gg n_{th}$, and writing n_s as $\eta(\lambda)\phi(\lambda)\tau/d$, where $\phi(\lambda)$ is the photon flux density, we obtain

$$D^* = \frac{\lambda}{2hc} \left(\frac{\eta(\lambda)}{\phi(\lambda)} \right)^{\frac{1}{2}} . \quad (19)$$

This basic equation has been developed here on the one hand because its

elegant simplicity deserves once again to be appreciated, and on the other hand, because a number of treatments of it in the literature are not without error, or start with assumptions that are no more self-evident than the result. The detectivity is seen to depend only on the wavelength, the quantum efficiency, and the background flux density. The wavelength dependence stems simply from the normalization to incident power.

For various applications, figures of merit for detectors other than the detectivity are more appropriate. It is generally more relevant to define the detection limits in terms of minimum resolvable temperature difference or the noise equivalent flux density. The appropriate figures of merit for extrinsic detectors have been treated by Nelson²² and by LoVecchio²³ for the near-IR applications. However, from a basic mechanisms standpoint, D^* remains a useful figure of merit. Peak quantum efficiencies are typically on the order of 0.1. Unity quantum efficiency is rarely achieved due to limited solubilities and low photoionization cross-sections. If quantum efficiencies are much less than 0.1, the detector is generally not of practical use.

The background flux density is usually not confined to the wavelength of interest, as assumed in Equation (19), but is broadband and governed principally by the cutoff wavelength of the detector, λ_c , given by the energy conservation criterion as

$$\lambda_c = \frac{1.24 \text{ } \mu\text{m}}{E_a \text{ (eV)}} \quad (20)$$

For the detectivity at the peak response wavelength (λ_p) under conditions of broad background, for example, we would have

$$D^*(\lambda_p) = \left(\frac{\eta(\lambda_p)}{\phi_{B,eff}} \right)^{1/2} \lambda_p / 2hc \quad (21)$$

where the effective background flux density $\phi_{B,eff}$ is given by

$$\phi_{B,eff} = \frac{1}{\sigma_p} \int_0^\infty \phi_B(\lambda) \sigma(\lambda) d\lambda \quad (22)$$

Additional insight may be gained by considering the dependence of n_s and n_{th} , respectively, on material parameters. We may write (for donor-type dopants)

$$\begin{aligned} n_s &= N_D \phi_{B,eff} c_p \tau \\ &= \frac{N_D}{c_n N_A} \int_0^\infty \phi_B(\lambda) c(\lambda) d\lambda \end{aligned} \quad (24)$$

where it has been assumed that $\tau = (c_n N_A)^{-1}$. Comparison of this equation with Equation (8) for n_{th} reveals that both quantities depend on the compensation ratio, N_D/N_A . From the standpoint of detector noise alone, then, it is found that the temperature at which background-limited conditions of operation are reached under a given background is independent of the degree of compensation, and this latter parameter is again seen to be significant only with respect to amplifier noise limitations. With respect to radiation effects on detectors, this implies a considerably different sensitivity to detector parameters for the case of medium-background thermal imaging or near-infrared detection compared to low-background conditions of operation, where amplifier noise is more likely to be dominant. With this brief introduction, the effects of neutron irradiation on extrinsic detectors are now briefly discussed in terms of their permanent effects.

It is useful to distinguish between the effects of neutrons on extrinsic detectors which affect the performance permanently, or cumulatively, and those effects which are transient. The relevant time scale for the former is that of a mission, for example. The time scale of interest for the latter is on the order of frame times. A typical detector array will be employed with compensation for quiescent background, or dark, signals and with normalization of responsivity differences between detector elements. The relevant time scale in that event is that with which the reference values for the detector elements are updated in memory.

The detector material parameters which undergo permanent change under neutron radiation are those of mobility, majority carrier lifetime, and dark resistivity. The lifetime and mobility impact the photoconductive gain directly. The mobility is governed by ionized impurity scattering, neutral impurity

scattering, and phonon scattering. Neutron irradiation introduces both donor and acceptor levels deep within the gap, and these serve as additional compensation in both resistivity types, thus increasing the concentration of charged centers which thus contribute to the most effective scattering mechanism at low temperature.

The majority carrier lifetime is determined by all possible processes which remove the carrier from the band, and is more appropriately referred to as a trapping time, since recombination across the bandgap is generally not involved. For thermal imaging detectors utilizing the shallow III-V dopants, such trapping occurs principally at the ionized shallow levels, via the Lax giant-trap, or phonon-cascade, mechanism.¹⁸ Trapping in excited states of neutral impurities appears also to be important at low temperatures (on the order of 10^0K) where the probability of thermal reexcitation from such levels becomes negligible.²⁴ For the case of near-IR detection, where deeper dopants are involved, the importance of trapping at excited states of neutral centers has not, to our knowledge, been definitively established. It would appear that at the higher temperature of operation characteristic of those detectors, thermal detrapping from such shallow excited states would render such trapping processes unimportant.

The dark resistivity of detectors may also be altered by neutron irradiation. In the case of the shallow dopants, any neutron-induced level will be deeper than the intentional dopant level. For the case of arsenic, as an example, any such levels which are acceptor-type will be compensating. An experimental determination of such compensation has already been made, and a carrier removal rate of about 16 per neutron/cm² was determined.²⁵ The effect of this is to increase the device impedance at a given temperature, according to Equation (9), and to decrease the lifetime. The impedance change in this case is innocuous. The impact on lifetime depends on the pre-irradiation compensation level. If, for example, the detector were characterized initially by a compensation of $1.6 \times 10^{13} \text{ cm}^{-3}$ boron, then a fluence of 10^{12} n/cm^2 would result in a reduction in lifetime by a factor of two. In the case of deep impurities, matters may be considerably different. The neutron-induced level spectrum of acceptors and donors may extend closer to the bandedge than the intentional dopant level. In that event, the net carrier removal rate may be considerably reduced below that which is observed for the shallow dopants. In the extreme

case, however, it is possible that neutron-induced levels which are shallower than the intentional dopant will govern the resistivity. In that event, lower operating temperatures would be required to reach the BLIP limit of carrier concentration than those implied by the impurity activation energy (Equations (8) and (10)). Since our interest extends to the deeper impurities as well as the shallow ones, this possibility has been experimentally examined, and results are given below. An additional reason for examining the permanent neutron irradiation effects for each dopant which might be employed in extrinsic detection is that the possibility of complex formation between the intentional dopants and neutron-induced defects may be revealed.

3.3 EXPERIMENTAL RESULTS

The first experimental task undertaken consisted of the determination of neutron effects on silicon doped with deep-level dopants as a complement to measurements previously performed to determine the carrier removal rate in arsenic-doped silicon.²⁵ The dopants studied were zinc, sulfur, and gold. The case of zinc, which has already been mentioned (see Figure 3-1), is that of a relatively deep acceptor. The sulfur level of interest is the donor level at about 0.19 eV from the conduction band, and the gold level of interest is the acceptor level near midgap. The case of gold is more of interest from a theoretical standpoint rather than as a practical detector material.

The carrier removal rate has been determined in these materials by Hall measurement of the carrier concentration as a function of temperature in the freeze-out regime. This requires measurement under conditions in which the sample impedance is quite high, and for that purpose the conventional Hall measurement method has been suitably modified. The apparatus is shown in Figure 3-2. Dog-eared samples are used, in preference to Van der Pauw geometry, because the field-strength in the active region is more uniform, and unambiguously known. This is of potential significance for resistivity measurements since majority carrier lifetimes may exhibit field dependences. The Hall and resistivity voltages are sampled by means of electrometer operational amplifiers of 10^{13} -ohm input impedance. These amplifiers are maintained under constant-temperature conditions within the cryostat, minimizing input capacitance, microphonics, and pick-up. Measurement of the carrier concentration as a function of temperature over the range from that at which carriers are totally

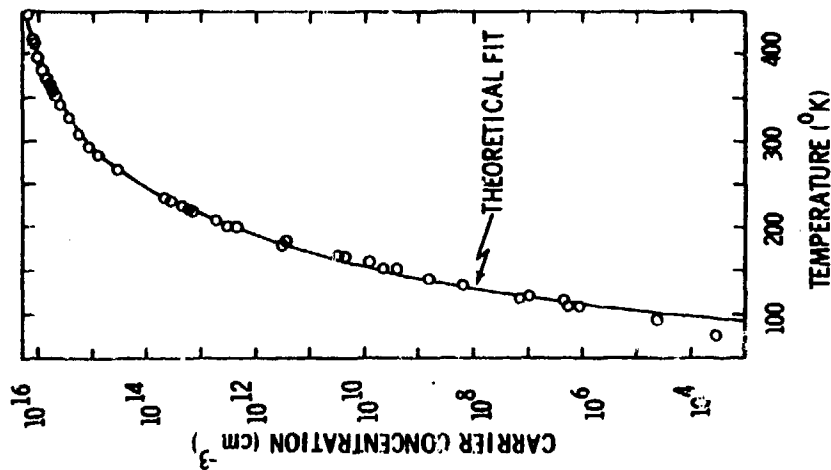


Figure 3-3. Carrier concentration as a function of temperature for a zinc-diffused sample. The data are fitted with a theoretical curve using the following parameters: $E_a = 0.31$ eV, $\beta = 2$, $N_{Zn} = 5.6 \times 10^{16} \text{ cm}^{-3}$, $N_D = 1.6 \times 10^{15} \text{ cm}^{-3}$.

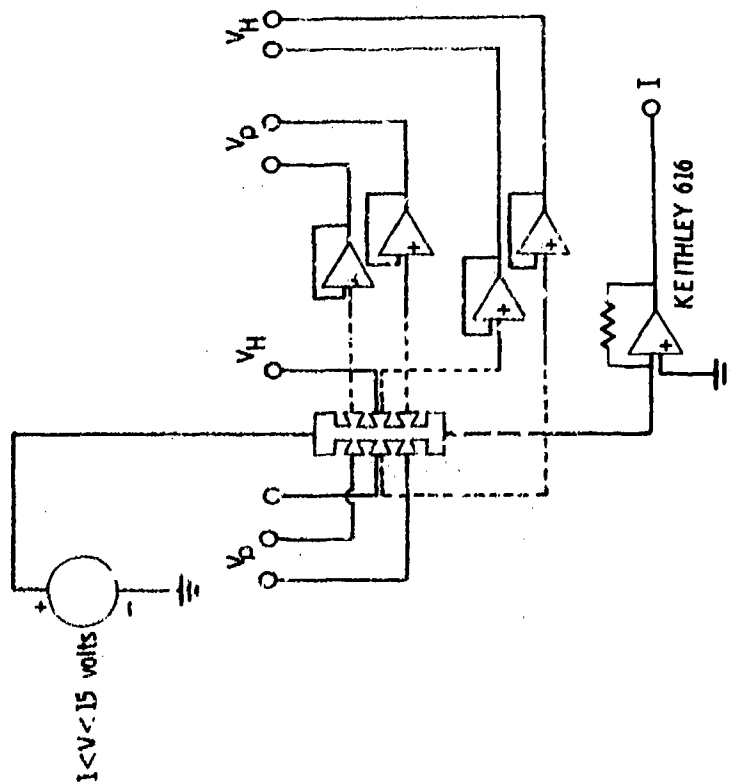


Figure 2-2. Schematic diagram of the method for making Hall mobility, resistivity, and carrier concentration measurements. At high sample impedance, voltages are measured with non-inverting operational electrometer amplifiers (Burr-Brown 3523) which have a high input impedance (10^{13} ohms). At low sample impedance, voltages are measured directly to eliminate offset voltage errors from the measurements.

ionized to that at which they are totally frozen out permits determination of the electrically active fraction of the intentional dopant, the concentration of compensating species, and the statistical weight, by fitting of Equations (7) or (9) to the data. In general, such determinations are subject to considerable uncertainties with regard to the compensation level and the statistical weight. Typical data taken on a zinc-doped sample are shown in Figure 3-3, and are useful to illustrate the point. The figure shows carrier concentration over the range of about 10^3 to more than 10^{16} cm^{-3} . The low-temperature carrier concentration is determined by both the compensation and the statistical weight. The steepness of the curve in this region, however, makes manifest the experimental difficulty of obtaining precise values. The curve-fit is sensitive to the choice of statistical weight only in the intermediate regime, i.e., where fractional ionization ranges between 10^{-3} and 10^{-1} . A fit to this curve was obtained with a choice of statistical weight of unity, and the values $N_{\text{Zn}} = 10^{16}$ cm^{-3} and $N_{\text{D}} = 10^{14}$ cm^{-3} were determined. With a choice of statistical weight of two, a slightly better fit was obtained, with the parameters $N_{\text{Zn}} = 5.6 \times 10^{16}$ cm^{-3} and $N_{\text{D}} = 1.6 \times 10^{15}$ cm^{-3} .²⁶ With a choice of $\beta = 4$, we find $N_{\text{Zn}} = 7.5 \times 10^{16}$, and $N_{\text{D}} = 8.8 \times 10^{14}$. An additional variable in the fit is, of course, the activation energy. A value of 0.31 eV was employed in all cases above. It is apparent that the availability of data over 13 orders of magnitude does not assure the absence of ambiguities in the fit, most particularly with regard to the very important compensation level. Since the experimentally observed quantity is the fractional change in compensation, our purpose is served only if the initial compensation level is well-known in our specimens.

The difficulties of establishing an accurate value of compensation level are not entirely experimental. The fit presupposes that only a single level is important in the determination of the carrier concentration, in addition to any levels which are compensating. The existence of excited states of the impurity, and of other impurity levels in lower concentrations, impact this simple picture. For this reason, it is preferred that bounds may be placed on the permissible values of the compensation level and the statistical weight initially. This is done by studying material over a range of initial resistivities. If these resistivities are sufficiently low, then it may be assumed that compensation levels will not undergo significant change in the process of diffusion of the intentional impurity, unless complexes form with that impurity. In this

manner, a statistical weight of two had previously been determined for zinc.²⁷ This approach was taken in the present work, and the material studied was therefore heavily compensated, and not typical of detector-grade material.

Results of measurements of the temperature dependence for a zinc-doped specimen, both before and after neutron irradiation, are shown in Figure 3-4. The zinc concentration had been determined to be $9 \times 10^{16} \text{ cm}^{-3}$ for this material by previous measurements of carrier concentration at high temperature. The pre-diffusion carrier concentration was determined from resistivity measurements to be $2.3 \times 10^{15} \text{ cm}^{-3}$ of phosphorus. The irradiation was performed at dry ice temperature, and the sample kept at that temperature except for one hour at room temperature just prior to measurement.

The observed changes in sample resistivity under irradiation with up to $6 \times 10^{14} \text{ n/cm}^2$ are seen to be quite small. If the pre-Zn-diffusion carrier concentration is taken to be the compensation level, a carrier removal rate of about $2 \text{ cm}^2/\text{n}$ is indicated for the first irradiation, and a value of about $5 \text{ cm}^2/\text{n}$ for the second irradiation. Since the observed change is not large compared to our experimental resolution, there remains some uncertainty in these values. Nevertheless, it appears that the carrier removal rate is considerably smaller for this deeper level than for a shallow level like arsenic. A better comparison would of course be provided by boron, but we know of no such data.

Data for neutron-irradiation-induced compensation of the sulfur donor level at 0.19 eV below the conduction band is shown in Figure 3-5 for two irradiations. The sulfur concentration in this sample had been determined to be 8.5×10^{15} by resistivity measurements at room temperature, where the sulfur level is completely ionized, and the pre-diffusion carrier concentration had been determined to be $1.4 \times 10^{15} \text{ cm}^{-3}$ of boron, likewise from resistivity measurements. Conditions of irradiation were as before. Once again, resistivity changes are found to be small, and the calculated values of compensation rate thus subject to some error. The value determined for the first run is $28 \text{ cm}^2/\text{n}$ and for the second, $9 \text{ cm}^2/\text{n}$. The second value is clearly the more reliable. It is roughly comparable, though somewhat less, than the value of $16 \text{ cm}^2/\text{n}$ found for the shallow arsenic level by Kalma.²⁵ If the difference is indeed real, then it implies that the effective acceptor concentration is less for

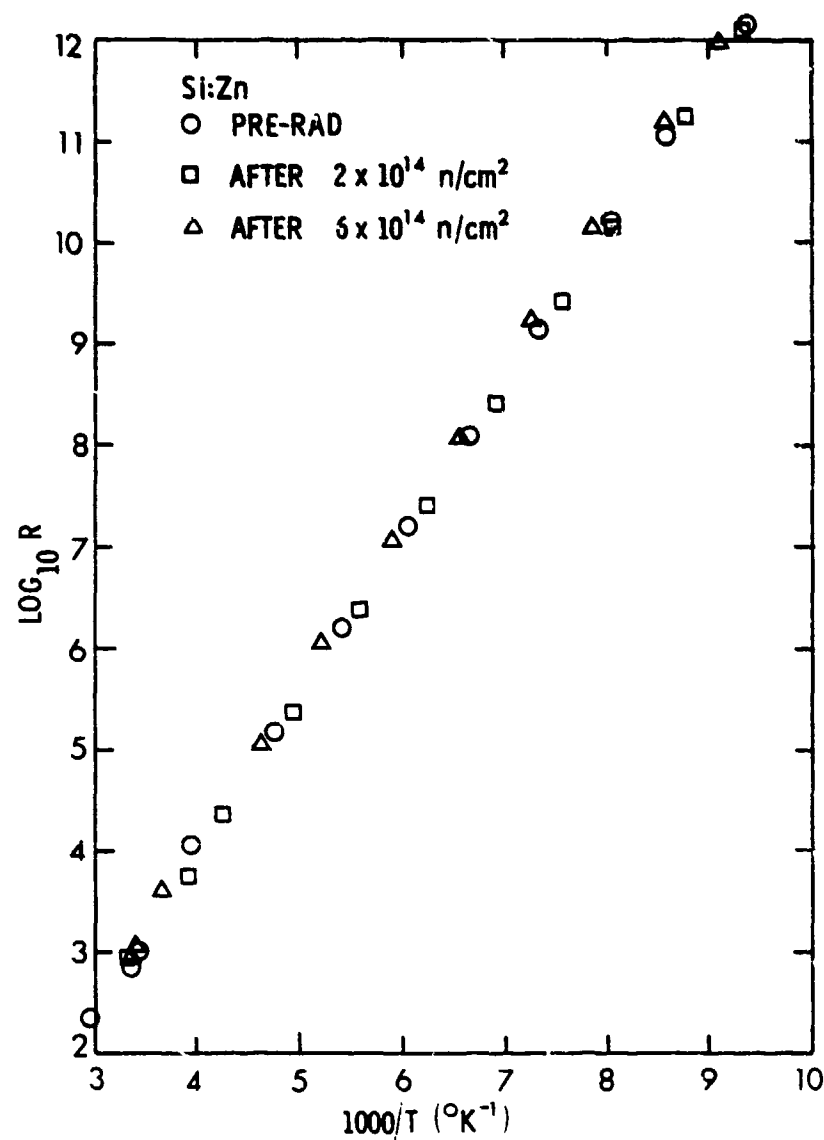


Figure 3-4. Results of measurements of sample resistance as a function of temperature before and after neutron irradiation for a zinc-diffused sample. The zinc concentration is $9 \times 10^{16} \text{ cm}^{-3}$ and the phosphorus concentration is $2.3 \times 10^{15} \text{ cm}^{-3}$.

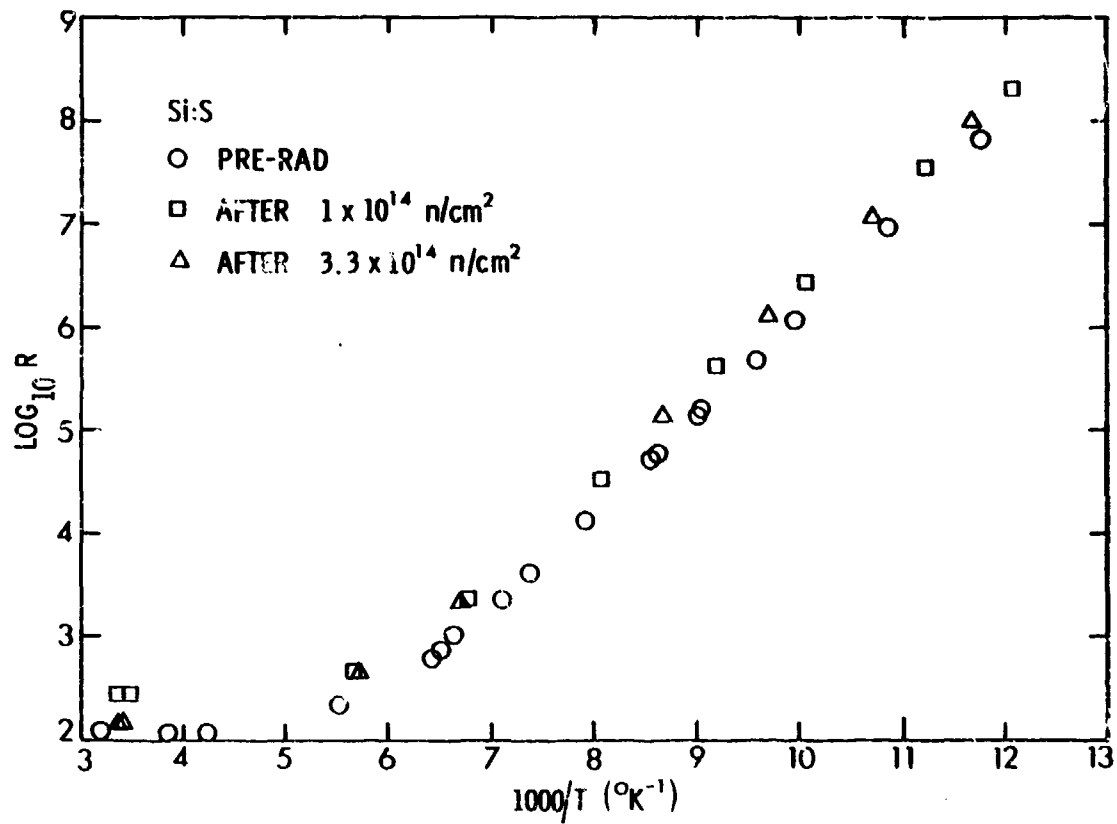


Figure 3-5. Results of measurements of sample resistance as a function of temperature for a sulfur-diffused sample before and after neutron irradiation. The sulfur concentration is 8.5×10^{15} cm⁻³ and $N_A = 2.3 \times 10^{15}$ cm⁻³.

sulfur than for arsenic, i.e. a fraction of the neutron-induced acceptor levels lie shallower than the sulfur level.

A more extreme case of a deep level is represented by the gold acceptor state, which lies near midgap. The gold level structure is illustrated in Figure 3-6. A complication arises in this case because of the existence of a tri-gold shallow acceptor, in a concentration proportional to $(N_{Au})^3$. Sufficient donors have to be available to compensate this shallow level. A gold-diffused sample was prepared in which these conditions were met, and the level governing the resistivity temperature dependence was therefore the deep acceptor state. The gold concentration was determined to be $8 \times 10^{16} \text{ cm}^{-3}$.

Results of measurements of the carrier concentration as a function of temperature before and after neutron irradiation are shown in Figure 3-7. The effective activation energy governing the temperature dependence is seen to be reduced with fluence. Since the apparent low-temperature activation energy is different after the two runs, it is probably not reasonable to associate it with a particular level. If such material were to be used in a detector application in a neutron environment, the operating temperature would have to be chosen appropriate to the observed unpinning of the Fermi level from the deep gold acceptor level.

3.4 DISCUSSION AND SUMMARY

The essential finding of the first experiments undertaken in this study of extrinsic silicon detector materials is that the effective carrier removal rate, or equivalently the introduction rate of compensating defects or defect complexes, depends strongly on the depth within the gap of the intentional dopant level. The neutron-irradiation-produced level spectrum is distributed throughout the bandgap, so that essentially all of the defects of the appropriate type (acceptor or donor) are compensating with respect to shallow dopants, and only a fraction is effective for the deeper levels.

Specifically, the evidence thus far accumulated is to the effect that a donor level at 0.19 eV from the conduction band (sulfur) is compensated nearly as effectively as a shallow donor (arsenic). Thus, few acceptor states are introduced within the range of 0.045 to 0.19 eV from the conduction band, a result

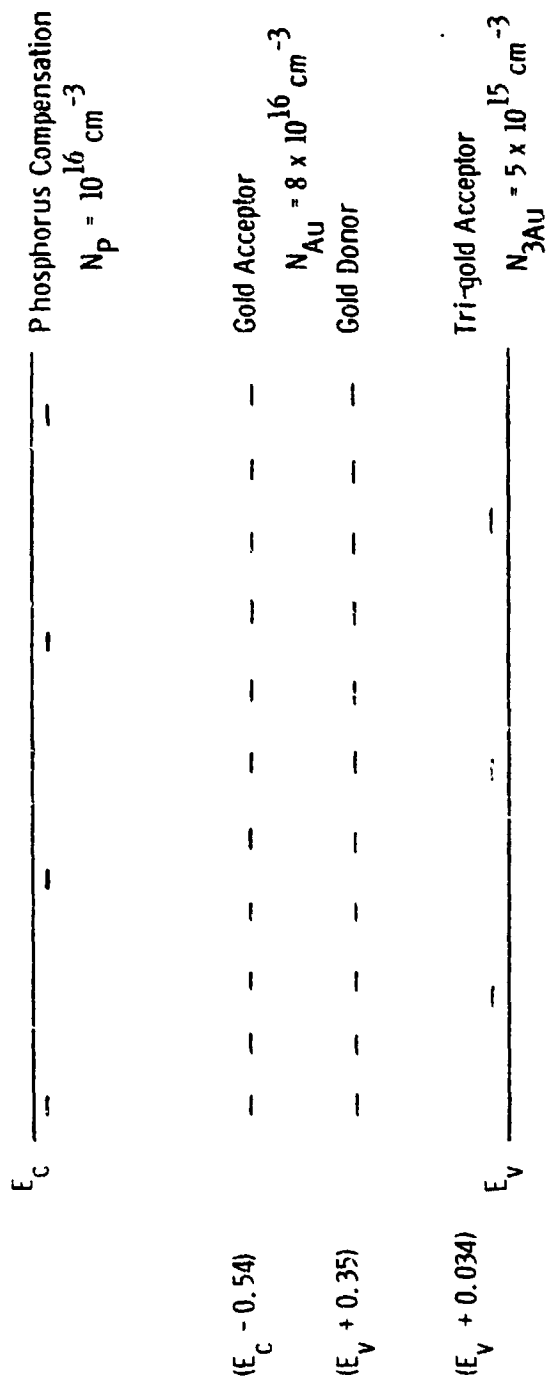


Figure 3-6. Level diagram for gold in silicon, showing the deep acceptor level, the deep donor level, and the tri-gold shallow acceptor state. Values for respective concentrations for the sample employed in this study are indicated.

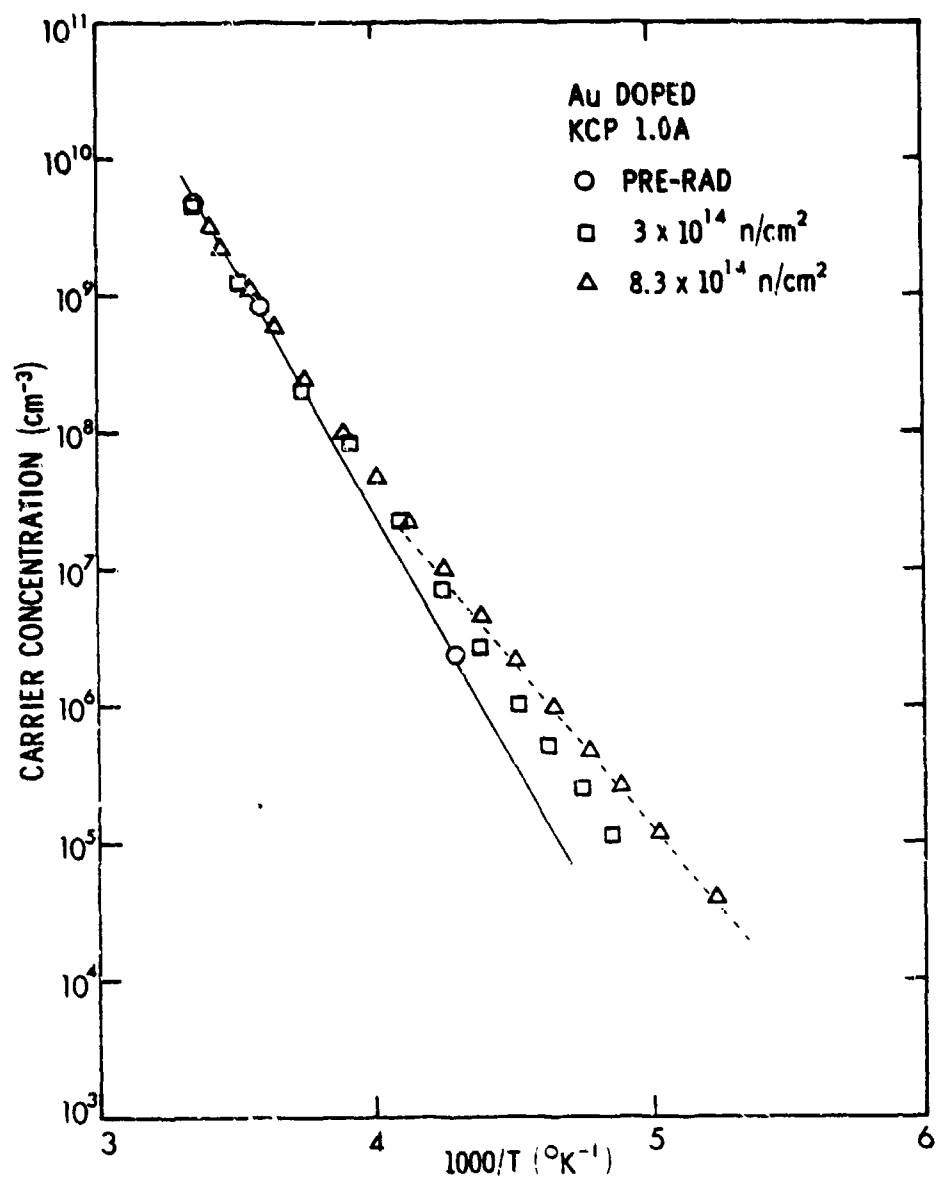


Figure 3-7. Results of measurements of carrier concentration as a function of temperature for a gold-diffused sample before and after neutron irradiation. The gold concentration is 8×10^{16} cm⁻³ and the phosphorus compensation is 1×10^{16} cm⁻³.

which is not too surprising. The carrier removal rate is found to be considerably smaller for the case of an acceptor level at 0.31 eV from the valence band (zinc). It would be helpful in the interpretation of these data to have available the comparable data for a shallow acceptor, which will hopefully be acquired later in the program. Under the circumstances, one can say only that either the donor introduction rate is considerably less than the acceptor introduction rate, or that the neutron-induced donor distribution extends to levels shallower than 0.31 eV in considerable measure.

The results for the gold level near midgap indicate that the net effect of both the donor and acceptor distributions (in energy) introduced by neutrons is to unpin the Fermi level from midgap. The Fermi level appears to be moved toward the conduction band, as may be seen by the following argument. The conductivity of the specimen employed was n-type, even though the dominant level was the acceptor level near midgap. This is consistent with calculations of resistivity at room temperature for gold- and phosphorus-doped silicon by Thurber et al.²⁸ There it is shown (following Bullis²⁹) that as the gold concentration is increased, for a given phosphorus concentration, the resistivity goes through a maximum near which the conductivity converts to p-type (by virtue of the tri-gold acceptor). In the present case, the room temperature resistivity remains approximately the same during the irradiation, and the specimen remains n-type. A shift in the Fermi level toward the valence band would have led to an increase in resistivity before a decrease would have been observed at higher fluences. A decrease in resistivity to pre-irradiation values would also have been accompanied by type conversion, which was not observed.

There are other methods of obtaining information about the distribution of neutron-induced levels within the energy gap. These measure changes in occupancy of deep traps, as in the depleted region of a p-n junction, to indicate trap properties such as energy level position and capture rates, as well as trap concentrations.³⁰ These techniques have the drawback that they are not equally sensitive experimentally to all types of traps. Typically, such methods are sensitive to traps in only one-half of the bandgap, making it necessary to study the other half in a sample which is fabricated differently, and thus not directly comparable. It is therefore useful to have available

information such as obtained here. Another point of difference is that other techniques look at the dominant traps, whereas in the present experiment, tails of distributions may have profound effects.

The simplest model which accounts for the fact that neutron-irradiation is compensating in its effect on both n-type and p-type (shallow-dopant) material is that of an acceptor level slightly above midgap, and a donor level slightly below.³⁰ The acceptor states would thus always be available to compensate shallow donors, and vice versa. By virtue of the complex nature of neutron damage, such levels are likely to be distributed somewhat in energy. If, then, the donor distribution extends significantly above the midgap gold level, the effect would be to unpin the Fermi level. An alternative explanation postulates the existence of a complex involving the gold center, in which case our conclusions about the distribution of neutron-induced levels would have less than general validity.

Having dwelt on the interpretation of the data for the gold level, we should recall that this is unlikely to be considered a practical detector material, and that our interest here is in forming a coherent picture. The data taken on the other samples, however, may have more relevance to actual detectors. In practical detectors, levels of compensation are typically much smaller than those characterizing the specimens employed here ($\sim 10^{15} \text{ cm}^{-3}$). Detectors for low background applications must operate with the minimum achievable compensation consistent with uniformity requirements. For high background applications, matters are different in that one may wish to design for a specific value of compensation, or dark resistance, not necessarily the minimum. Even in that event, however, compensation levels would be much closer to 10^{13} cm^{-3} than to 10^{15} cm^{-3} . If a value of 10^{13} cm^{-3} is assumed to prevail, then at a carrier removal rate of $10 \text{ cm}^2/\text{n}$, the responsivity of the detector would degrade by a factor of two under a fluence of 10^{12} n/cm^2 . The fact that the given specimens did not appear to undergo significant change under much higher neutron fluences than this is strictly due to the manner in which we chose to do the experiment, for the reason discussed earlier.

It is noteworthy that the carrier removal rates measured here for sulfur and previously for arsenic²⁵ are much higher than the carrier removal rates measured at room temperature for shallow dopant material. The latter were

measured to be between about 1.5-3 for n-type material, and about 3 for p-type material, using the same irradiation facility employed in the present measurements.³¹ Room temperature irradiations were employed, whereas dry ice irradiation was used here, and 10⁰K irradiations were used for arsenic. The data for sulfur were analyzed without regard for mobility changes under irradiation. These could have modest impact on the values determined for net carrier removal rate. In subsequent experiments, it is anticipated that better values will be obtained for carrier removal rate, since the carrier concentration and the mobility will both be measured, and since responsivity measurements will be made that will yield corroborative information about the rate of introduction of compensating defects. The measurements will also be made upon irradiation at detector operating temperature, so that immediate comparison of pre- and post-irradiation values will be possible without an intervening change of sample temperature.

The above data will be taken as a matter of course on all the detector materials to be studied. However, the primary focus of subsequent studies will be the response to transient illumination, rather than permanent damage effects. Regarding the latter, the present work has achieved its basic purpose in that there appears to be no profound consequence of neutron irradiation on near-infrared extrinsic detectors employing relatively deep dopants that is not explainable in terms of the introduction of compensating species. The exception is the gold acceptor level lying near the midgap, where an unpinning of the Fermi level is observed.

The interest in pursuing studies of response to transient extrinsic illumination of the deep impurities in addition to that of the shallow dopants stems from the fact that neutron-induced defects may result in profound changes in the recombination, or trapping, properties of detectors. Any levels which are shallower than the intentional dopant level will be subject to much larger probabilities of thermal reexcitation of trapped carriers than would hold for the latter. Such trapped carriers may therefore be read out during subsequent frame times, leading to contrast reduction and image retention. This may be thought of in terms of "temporal cross-talk", by analogy to spatial cross-talk in a two-dimensional array. In the case of shallow dopants, this problem does not arise, since bandwidth-limiting of the optical input signal can be used to insure that the deeper levels are never excited.

SECTION 4.0

MECHANISMS OF RADIATION EFFECTS ON CHARGE-COUPLED DEVICES

This section describes results of studies of radiation effects on charge-coupled devices. Emphasis is placed on determining the basic mechanisms underlying the various observed phenomena. Work performed during the first half of this program is described in Section 4.1; Section 4.2 presents results of additional work which was performed during the second half. The primary focus was on examination of radiation-induced increases in dark current density. Test vehicles employed include MOS capacitors and CCDs fabricated by both Hughes Aircraft and Fairchild Semiconductor. The MOS capacitors were used to obtain a neutron damage coefficient appropriate for describing increases in the generation-center density in silicon depletion regions. The rate of increase in dark-current density for neutron-irradiated CCDs was measured and comparison then made with results of calculations. The effect of a moderate reduction in operating temperature on the response of CCDs to neutron bombardment is described. Examination of the effects of ionizing radiation on CCDs revealed an anomalous increase in dark current density for Hughes Aircraft devices at relatively low total doses. At high doses, observed increases in dark current are attributed to introduction by Co^{60} gamma rays of generation centers in the depletion-region bulk and at the SiO_2 -Si interface. Results of short-term annealing studies on CCDs following pulsed neutron bombardment are also presented.

4.1 NEUTRON DAMAGE MECHANISMS IN CHARGE TRANSFER DEVICES

4.1.1 Introduction

Charge transfer devices (CTDs) are finding increased application for various electronic functions, including analog signal processing, digital data storage, and image sensing. Included in this class of integrated circuits are charge-coupled devices (CCDs) and charge-injection devices (CIDs). Charge transfer devices are fabricated using silicon MOS technology, and thus are susceptible to the transient and permanent effects of ionizing radiation. Certain electrical properties of CTDs will also degrade due to displacement damage produced by neutron bombardment. In this section, results of a study of the basic mechanisms of neutron effects on CTDs are presented.

Several investigations of the influence of neutron bombardment on the operation of CCDs have been made in the past few years.³²⁻³⁶ The primary effects are: (a) an increase in dark current due to the introduction of generation centers; (b) a decrease in charge transfer efficiency due to the introduction of trapping centers. Emphasis in the present investigation was placed on examining the mechanisms of dark current increases. As an aid to obtaining mechanistic information, neutron effects on MOS capacitors, which are the basic cells of a CID, were studied extensively. The MOS capacitors were used as test vehicles in the determination of damage coefficients that are applicable to the radiation response of CCDs. Also discussed in this section is the degree of radiation tolerance achievable in a neutron-irradiated CCD by a moderate reduction in device operating temperature.

4.1.2 Experimental Considerations

4.1.2.1 Devices

MOS capacitors used in this study were fabricated by Hughes Aircraft (HAC) using radiation hardening procedures. Devices were prepared on both n-type ($\sim 3 \Omega\text{-cm}$) and p-type ($\sim 0.8 \Omega\text{-cm}$) $\langle 100 \rangle$ silicon substrates with both wet and dry oxides. Wet (pyrogenic) oxidation was performed at 925°C , followed by a N_2 anneal at 925°C . Dry-oxide growth was performed at 1000°C . Circular Al

electrodes (~25-mil diameter) were evaporated from a graphite crucible; an anneal was subsequently performed at 500°C in N₂. The oxide thickness in the wet-oxide case was ~1000Å for the three lots studied, which are referred to as KA-09 (n-type), WET N (also n-type), and WET P. The thickness of the dry oxides was ~900Å for the two lots studied (DRY N and DRY P). The CCDs investigated were n-buried-channel devices also fabricated by Hughes Aircraft. These units are 128-bit analog shift registers employing a four-phase clock. They are hardened to the effects of total ionizing dose; processing details have been described previously.³⁷ (Devices studied were from two wafers (#15 and #19) of lot BN-09 which were fabricated using Mask #2128.)

4.1.2.2 Measurement Techniques for MOS Capacitors

Dark current in a charge transfer device is governed by thermal generation of carriers at centers in the depletion region and at the oxide-semiconductor interface. As noted above, the fundamental cell of a CTD is an MOS capacitor. Schroder and Nathanson³⁸ pointed out that for an MOS capacitor biased into depletion there exists a laterally depleted region in addition to that directly under the gate electrode. Figure 4-1 depicts this situation for an MOS capacitor on n-type silicon with an applied bias V_g which is more negative than the flatband voltage V_{fb} . Effects associated with the laterally depleted region have been discussed by Pierret and Small,^{39,40} and by Takino.⁴¹ In the study of silicon properties using an MOS capacitor, there are three "times" of interest: (1) depletion-region storage (or charge-up) time τ_s ; (2) minority-carrier generation lifetime τ_g ; (3) minority-carrier recombination lifetime τ_r . Storage time is defined as the time required for an inversion layer to be established in an MOS capacitor driven into deep depletion. This quantity is readily obtained from measurements of capacitance-versus-time (C-t) following application of a step voltage which drives a device into a deeply-depleted state. Establishment of an inversion layer in such a transient measurement occurs via thermal generation of carriers in the space-charge region and at the interface. Generation lifetime is a characteristic time associated with the thermal generation of carriers in the depletion region bulk. Recombination lifetime in the neutral bulk has its usual definition. In an unirradiated MOS capacitor at room temperature, τ_r and τ_g are typically on the order of microseconds whereas τ_s is on the order of seconds.

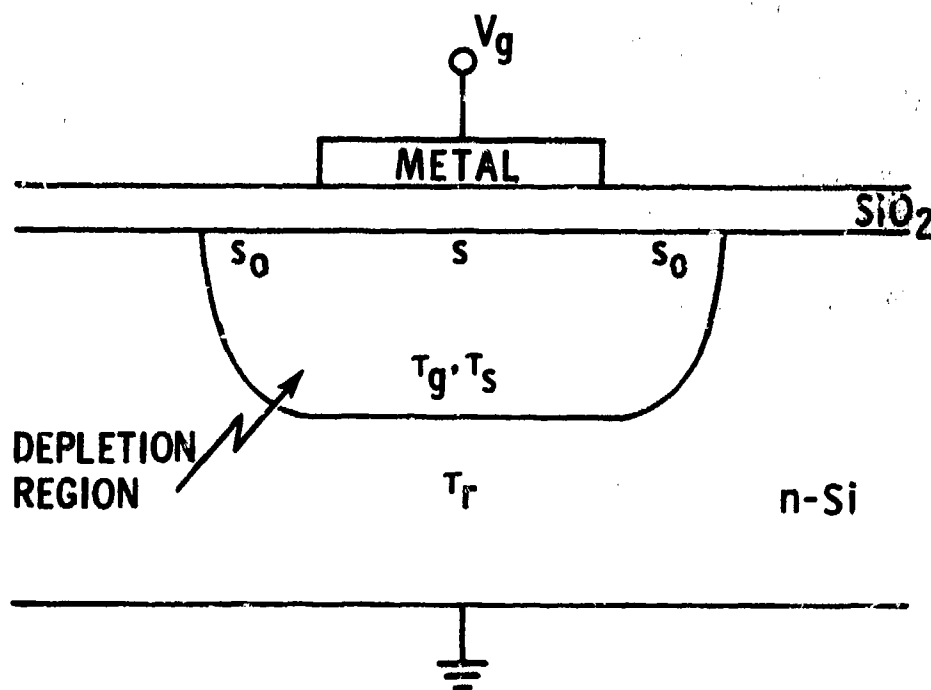


Figure 4-1. Schematic of an MOS capacitor on n-type silicon with an applied bias V_g more negative than the flatband voltage. The laterally depleted region is illustrated.

Generation lifetime is of fundamental importance because it provides a direct measure of properties of bulk generation centers, and thereby provides information regarding radiation-induced dark current increases in a CTD. To obtain τ_g , a typical approach has been to make a C-t measurement and interpret the results using Zerbst analysis.⁴² In principle, this analysis yields the generation lifetime and the surface generation velocity at the $\text{SiO}_2\text{-Si}$ interface. In practice, there are potential problems with Zerbst analysis, as discussed by various workers.^{38,40,41,43,44} A major problem is the proper separation of surface and bulk generation processes. Surface generation velocity s (and surface recombination velocity) is a function of surface potential.⁴⁵ The maximum value of s , denoted as s_0 , will occur when a surface is depleted. The value of s in either accumulation or inversion will be significantly less than s_0 . During a C-t measurement in which a device is pulsed from accumulation into deep depletion, the surface generation velocity under the gate electrode after pulsing should initially equal s_0 but will then decrease as a function of time as the inversion layer forms. This layer does not form in the laterally depleted region, however. Thus, the situation shown in Figure 4-1 exists in

which the lateral region is characterized by s_0 and the gate region is characterized by s .

In a C-t measurement, carrier generation at interface states under the gate electrode can be made negligible compared to other generation components by pulsing a device from inversion to stronger inversion instead of pulsing from accumulation to inversion.⁴⁰ In this situation, one obtains an effective generation lifetime τ_{ge} from analysis of C-t data since generation at the laterally depleted surface can still be important. The effect of the lateral component diminishes as the size of an MOS capacitor increases. In the present study, devices employed were large enough such that generation in the lateral region was unimportant. Thus, generation lifetime associated purely with the depletion-region bulk was obtained.

Measurements of storage time were made using a PAR Model 410 1-MHz CV system. Capacitors on an n-type substrate were pulsed from -5 to -10V; devices on a p-type substrate were pulsed from +5 to +10V. Storage time was defined here as the time required to reach the $[1-(1/e)]$ recovery point on a C-t curve. That is, if the inversion capacitance is denoted by C_{df} and the initial capacitance in deep depletion, by C_{do} , then τ_s is defined here as the time required for the capacitance to recover to a value equal to $C_{do} + 0.53(C_{df} - C_{do})$. (The implications of this τ_s definition on the relationship between τ_s and τ_g are discussed below.)

Generation lifetime τ_g was determined by Zerbst analysis⁴² of capacitance-versus-time data obtained in the above manner. Schroder and Nathanson³⁰ modified the analysis of Zerbst to account for carrier generation in the laterally depleted region shown in Figure 4-1. The differential equation obtained is

$$-\frac{d}{dt}\left(\frac{1}{C}\right)^2 = \frac{n_i}{N_d C_{ox}} \left(\frac{1}{\tau_g} + \frac{4s_0}{r} \right) \left(\frac{1}{C} - \frac{1}{C_{df}} \right) + \frac{2n_i s}{N_d C_{ox} \epsilon_s} \quad (1)$$

In this expression C is time-dependent capacitance, C_{ox} is oxide capacitance, N_d is donor concentration, s_0 and s are defined in Figure 4-1, and r is the radius of the MOS capacitor. The factor $[(1/\tau_g) + (4s_0/r)]$ is termed the effective generation lifetime τ_{ge} . The second term was determined to be negligible compared to the first for the present experimental conditions, so that $\tau_g (= \tau_{ge})$ was obtained.

Zerbst analysis involves obtaining C-t data and then determining the quantities

$$-\frac{d}{dt}\left(\frac{1}{C}\right)^2 \text{ and } \left(\frac{1}{C} - \frac{1}{C_{df}}\right).$$

A computer was used here to determine these quantities based on closely-spaced discrete data points from C-t plots. Figure 4-2 shows an example pre-irradiation Zerbst plot obtained in the present study. The slope of the straight-line fit shown yields τ_g and the y-intercept yields s . Note that although generation at the Si-SiO₂ interface is suppressed by driving the device from inversion to stronger inversion in a C-t measurement, finite values for s are still obtained. However, they are quite small, as anticipated (e.g., the results of Figure 4-2).

Several comments are in order. Zerbst analysis as presented above assumes a uniform doping concentration in the semiconductor. Takino⁴¹ has modified the Zerbst analysis to take into account the effects of a nonuniform

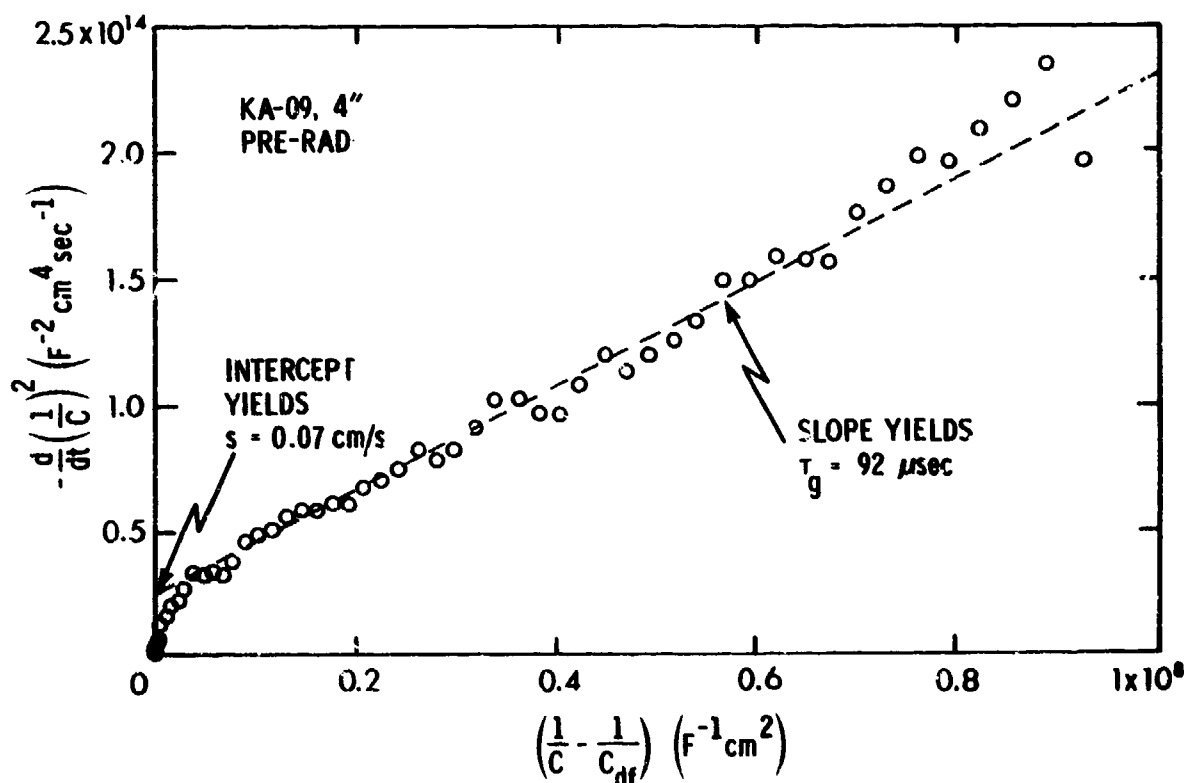


Figure 4-2. Zerbst plot for an unirradiated MOS capacitor. Values for generation lifetime and surface generation velocity are shown.

doping profile. We determined doping profiles for the present samples by appropriate computer-aided analysis of C-V curves and found them to be reasonably uniform. Even if they were somewhat nonuniform, Takino's modification would only have a second-order effect on the present experimental results.

Simmons and Wei⁴⁴ noted that the carrier generation rate during C-t measurements is not necessarily constant and that the electron and hole generation rates can differ. In particular, if the bulk generation center density (N_g) is high and if the voltage step (ΔV) applied is small, non-steady-state generation will result and Zerbst analysis will not necessarily yield an accurate generation lifetime. For the present experiments, where $\Delta V = 5V$, using the analysis of Simmons and Wei we have determined that as long as $N_g \leq 10^{13} \text{ cm}^{-3}$, the effects they discuss are unimportant. It is quite reasonable to assume that this condition holds before irradiation and after relatively low fluences of neutron bombardment since 10^{13} cm^{-3} is a rather high generation center density for silicon. As shown below, data obtained at all fluences are mutually consistent and yield a unique value of generation-lifetime damage coefficient. The indication is that we can safely ignore the effects discussed by Simmons and Wei in the present work.

4.1.2.3 Measurement Techniques for CCDs

Two methods were used in the measurement of dark current: (1) integration method; (2) continuous clocking method. In both approaches, no charge is input to the CCD; the input diode is reverse biased. In the integration technique, the shift register clocks are stopped for a fixed integration time (typically 10 to 300 msec), and then the thermally-generated dark charge is clocked to the output transistor at a relatively fast rate (typically 500 kHz). In a four-phase clock system, two adjacent phases are held high while the other two are held low. The reset line is active (i.e., high) during the integration period. The total integration time is the sum of the time during which the clocks are static and the time it takes to clock the charge to the output. Use of a high clock frequency makes the latter contribution negligible.

The continuous clocking method involves measuring the output signal with the clocks freely running at some frequency f_c . To compare this approach with

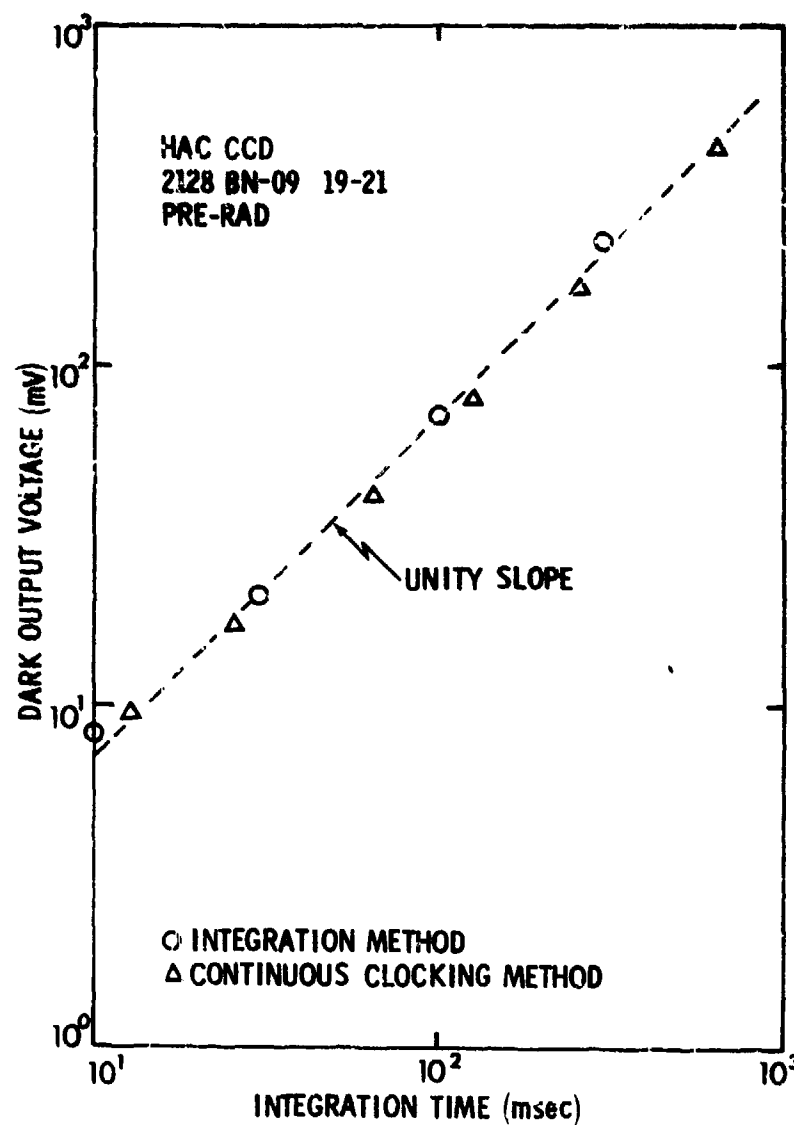


Figure 4-3. Dark output voltage versus integration time for an un-irradiated CCD. Measurements obtained by two methods are illustrated ($t_i = 128/f_c$ for continuous clocking method).

the integration method, one can convert to an equivalent integration time by the relation $128/f_c$ for the HAC CCD. That is, the integration time in this method is the time it takes to clock a single bit through the CCD. Typical data obtained by both dark current measurement techniques are shown in Figure 4-3 for an unirradiated CCD. Plotted is the measured output voltage (\equiv dark voltage V_d) versus integration time, where this time is defined in the manner described above for each method. The expected linear variation with integration time is exhibited, and the agreement between the two methods is good.

The quantity of practical interest in a CTD is the dark current density J_d . This quantity is given by I_d/A , where I_d is dark current and A is the area of one bit. (For a four-phase CCD, this area is that under four adjacent gate electrodes.) Dark current density can be expressed as

$$J_d = KV_d/At_i, \quad (2)$$

where t_i is integration time and K is a constant for a given device. To evaluate K , one needs to measure current through the CCD and the corresponding output voltage for some reference time t_{ref} . For twelve HAC CCDs, K varied from 7 to 9×10^{-13} A-sec/V. The effect of neutron bombardment on this parameter was slight for the fluences employed. The data of Figure 4-3 yield a value for dark current density of 15 nA/cm^2 ($A = 38.7 \times 10^{-6} \text{ cm}^2$).

All devices were irradiated at room temperature, which ranged from ~ 24 to $\sim 33^\circ\text{C}$. For purposes of comparison, all CCD data were corrected to 25°C using a measured dark-current temperature dependence of $\exp(-0.63 \text{ eV}/kT)$.

4.1.2.4 Irradiation Procedures

All irradiations were performed using the TRIGA Mark F reactor at Northrop Research and Technology Center. For MOS capacitors, the reactor was operated in a steady-state mode at power levels of both 5 and 50 kW. Devices being irradiated were unbiased, with their leads imbedded in conductive foam. A 2.3-inch lead shield plus a 0.25-inch boral shield were in place in the dry exposure room. An additional 2 inches of lead shielding was placed in front of each device for the purpose of enhancing the neutron-to-gamma ratio. Neutron fluences were determined using sulfur dosimeters; a plutonium-to-sulfur ratio of 11.9 was used to obtain $> 10 \text{ keV}$ fluences. Gamma dosimetry was performed using CaF_2 thermoluminescent dosimeters. For CCDs, the reactor was operated in both pulsed and steady-state modes. Shielding was the same as given above, as were the steady-state reactor operating conditions. For pulsed operation, a pulse with $\$1.90$ reactivity was used and the pulsewidth was $\sim 20 \text{ msec}$.

In order to minimize long-term annealing effects between the time of irradiation and the time of post-irradiation measurements, irradiated MOS capacitors were placed in storage at dry-ice temperature within one-half hour following irradiation. A device to be characterized post-irradiation was

removed from dry ice and left at room temperature for one and one-half hours in order to achieve stability. Measurements of C-t were then made.

4.1.3 MOS Capacitor Results

Measurements of capacitance versus time were made on MOS capacitors before and after neutron bombardment, and these data were used to obtain storage time, generation lifetime, and surface generation velocity. The following expressions were employed to define specific damage coefficients:

$$\frac{1}{\tau_s} = \frac{1}{\tau_{so}} + \frac{\phi}{K_s} \quad (3)$$

$$\frac{1}{\tau_g} = \frac{1}{\tau_{go}} + \frac{\phi}{K_g} \quad (4)$$

$$s(\text{post}) = s(\text{pre}) + K_Y^S \gamma. \quad (5)$$

In Eq. (3), τ_{so} and τ_s are values of storage time measured pre- and post-irradiation, respectively, ϕ is neutron fluence, and K_s is storage-time neutron damage coefficient. Similar definitions apply to Eq. (4). Equation (5) relates pre- and post-irradiation values of surface generation velocity; γ is the total ionizing dose received during neutron bombardment (primarily due to gamma rays) and K_Y^S is the damage coefficient associated with the increase in s due to the effects of ionizing radiation. (Typical pre-irradiation values of storage time, generation lifetime, and surface generation velocity are shown in Figures 4-2 and 4-7.)

Results of storage-time measurements for devices on both n- and p-type substrates are shown in Figure 4-4. In each case, the data are fit quite well by a unity-slope line as shown, and the damage coefficients obtained are as follows: $K_s(\text{n-type}) = 1.2 \times 10^{13} \text{ n-sec/cm}^2$; $K_s(\text{p-type}) = 5.0 \times 10^{13} \text{ n-sec/cm}^2$. The corresponding generation lifetime data obtained using Zerbst analysis are presented in Figure 4-5. Linear degradation is again observed, data for devices on n- and p-type substrates are in agreement, and the following damage coefficient is obtained: $K_g = 7.0 \times 10^6 \text{ n-sec/cm}^2$. The dashed lines shown in Figure 4-5 correspond to expected behavior for recombination lifetime, τ_r , in neutral bulk material (and the associated damage coefficient K_r) based on the following low-injection-level

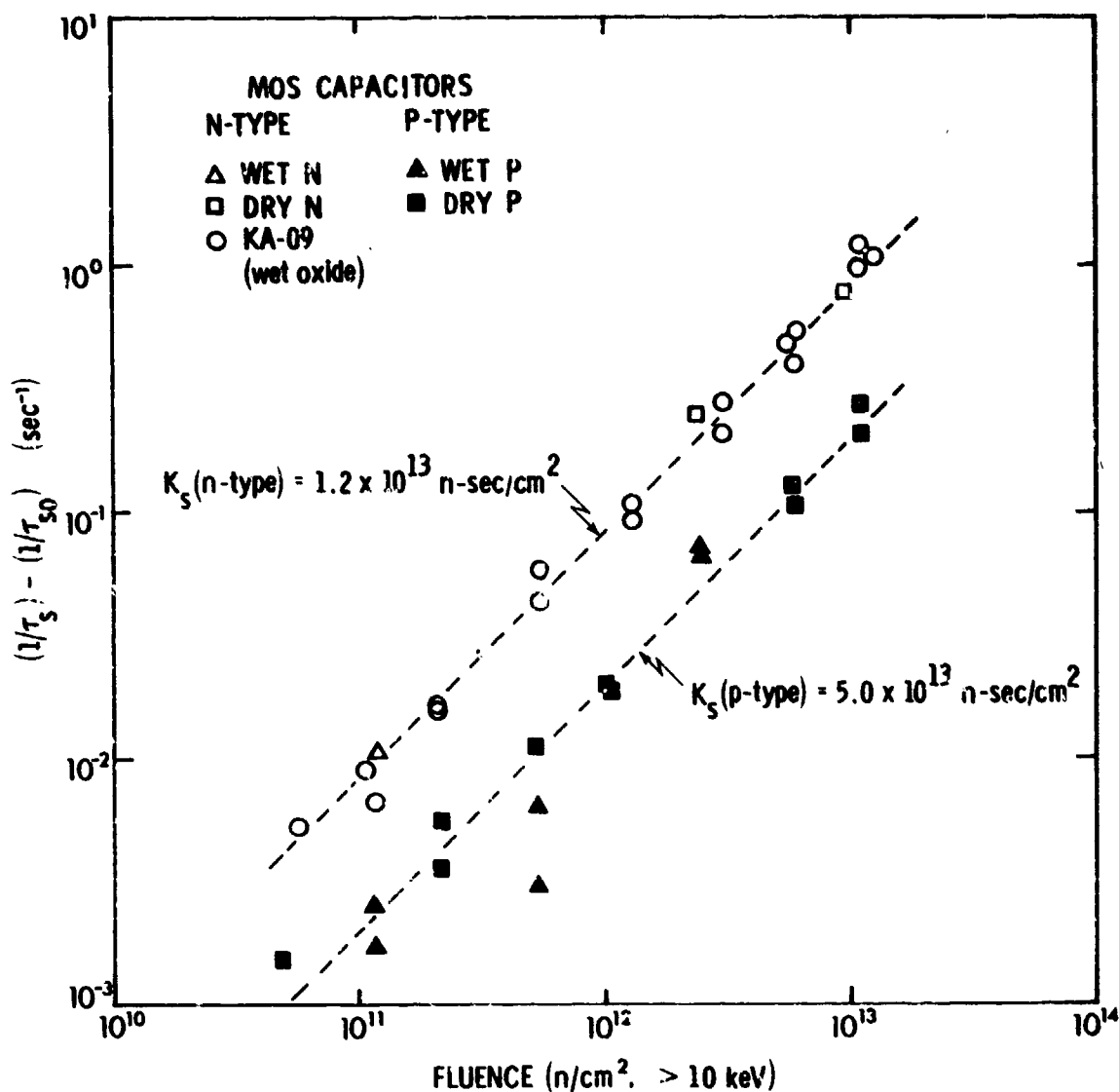


Figure 4-4. Storage time degradation in neutron-irradiated MOS capacitors. The unity-slope fits yield storage-time damage coefficients.

values:¹⁵ $K_r(\text{n-type}) \cong 1 \times 10^5 \text{ n-sec/cm}^2$; $K_r(\text{p-type}) \cong 2 \times 10^5 \text{ n-sec/cm}^2$. Thus, values for K_g/K_r are on the order of 70 and 35 for n- and p-type material, respectively. Note in Figure 4-5 that there is no dependence of the generation lifetime data on oxide growth condition. No such dependence is expected for damage introduction in the depletion region bulk. Also, the fact that results for n- and p-type material are in agreement indicates that the dominant neutron-induced generation center is the same in both cases.

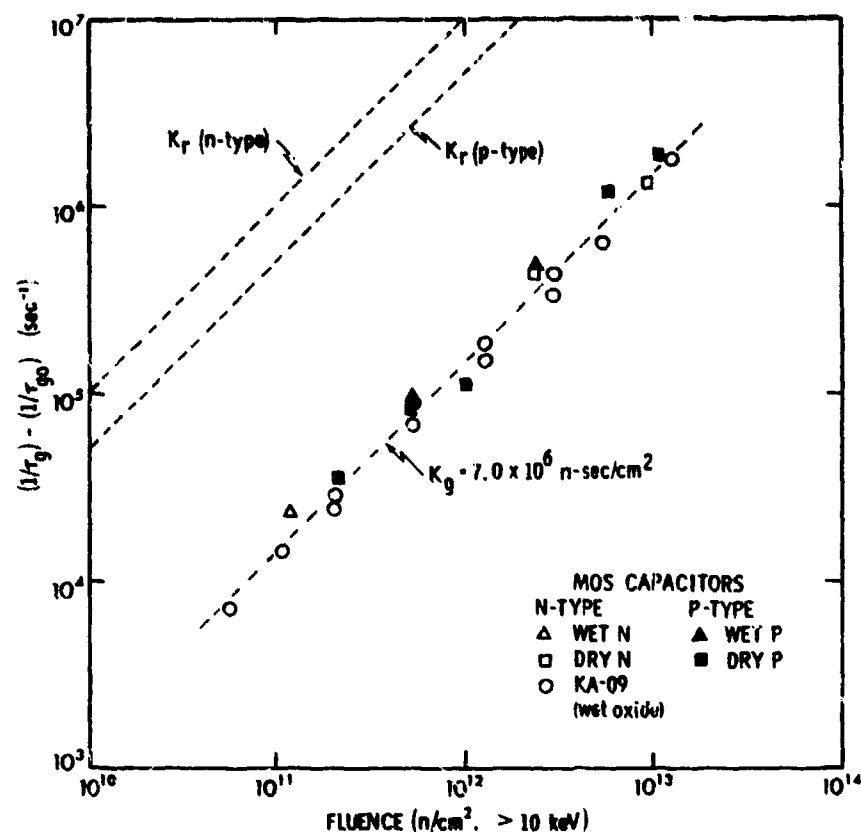


Figure 4-5. Generation lifetime degradation in neutron-irradiated MOS capacitors. The unity-slope fit yields generation-lifetime damage coefficient.

Surface-generation-velocity results are shown in Figure 4-6. Some scatter is evident but the trends are clear, and the following damage coefficients result: $K_Y^S(\text{n-type}) = 6.5 \times 10^{-3} \text{ cm/s-rad}$; $K_Y^S(\text{p-type}) = 1.5 \times 10^{-3} \text{ cm/s-rad}$. It is interesting to note that significant changes in surface generation velocity are produced by a total dose of less than 100 rads. The observed increase in s can most likely be attributed to the introduction by ionizing radiation of interface states. In previous studies by various workers on radiation-hardened oxides, such as those contained in the present devices, substantially higher total doses were required before significant changes in interface-state density were observed. This suggests that the present experimental approach may be a sensitive tool in basic studies of interface states introduced by ionizing radiation.*

*It is assumed here that the observed change in s (Figure 4-6) is an effect of ionizing radiation. However, experiments and calculations performed after the completion of this program revealed that this is actually a neutron effect. Information on this subject is contained in a paper by J.R. Srour et al. that will appear in the December 1979 issue of the IEEE Transactions on Nuclear Science.

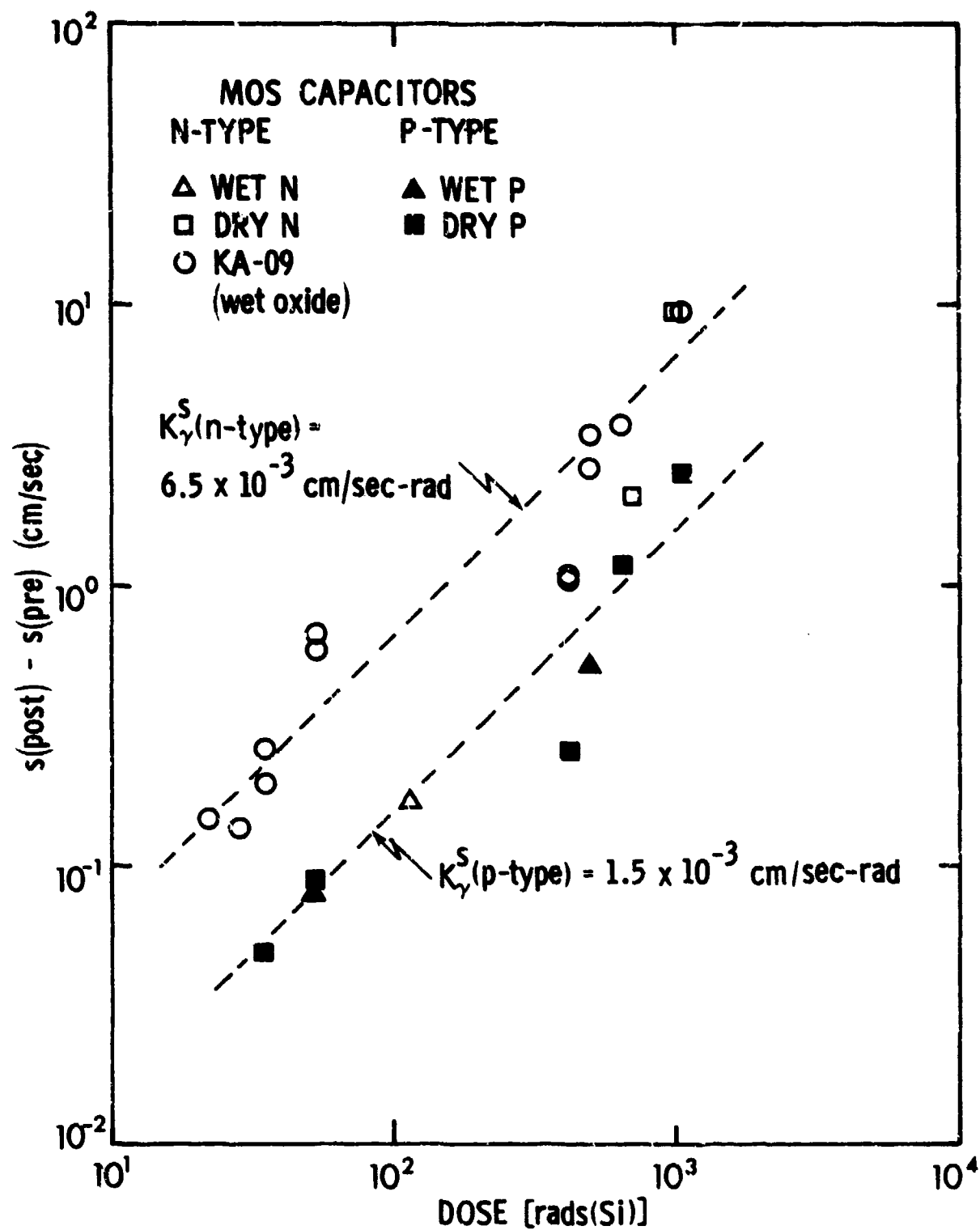


Figure 4-6. Surface generation velocity increase in irradiated MOS capacitors. The unity-slope fits yield surface-generation-velocity damage coefficients.

Table 4-1 lists the damage coefficient values obtained here and also gives previously obtained values⁴⁶ of K_r . There is more than six orders of magnitude difference between values for K_s and K_g and nearly two orders of magnitude difference between values for K_g and K_r (for n-type). The K_g versus K_r difference is considered first.

Table 4-1. Experimentally determined damage coefficients. Values for K_r are from Reference 46.

	n-type	p-type
K_s	1.2×10^{13} n-sec/cm ²	5.0×10^{13} n-sec/cm ²
K_g	7.0×10^6 "	7.0×10^6 "
K_r	1×10^5 "	2×10^5 "
K_Y^S	$\sim 6.5 \times 10^{-3}$ cm/s-rad	$\sim 1.5 \times 10^{-3}$ cm/s-rad

Heiman⁴⁷ performed a detailed analysis of a capacitance-versus-time experiment and obtained the following expression:

$$\ln \left(\frac{(C_{df}/C) - 1}{(C_{df}/C_{do}) - 1} \right) + \left(\frac{C_{df}}{C} - \frac{C_{df}}{C_{do}} \right) = - \frac{G C_{df}}{N_d C_{ox}} t. \quad (6)$$

In this equation, G is the carrier generation rate in the depletion region and the other terms were defined above. (Equation (6) differs from Eq. (4) of Heiman by the C_{ox} factor on the right-hand side, presumably due to a typographical error in his paper.) If the second term on the left-hand side of Eq. (6) is negligible compared to the first, a simple exponential solution for capacitance as a function of time results, with the time constant being equal to $N_d C_{ox}/G C_{df}$. For the present conditions, the first term dominates only during the last third of the capacitance recovery process. However, as a first-order approximation, we neglect the second term.

As noted above, τ_s was determined experimentally from the $[1 - (1/e)]$ point in capacitance recovery. However, Eq. (6) is based on recovery (or reduction) of the depletion width, i.e., on the generation of charge. This consideration results in a slight modification when comparing the present experimental results with analysis. For our conditions, recovery of the depletion width to the 63% point corresponds to recovery of capacitance to the 45% point. This consideration results in a reduction of the experimental values of τ_s and K_s by a factor of ~ 0.75 if they are to be compared with calculations using Eq. (6).

The carrier generation rate in a depletion region is given by $n_i/2\tau_g$. We therefore obtain

$$\tau_s = \frac{C_{ox}}{C_{df}} \left(\frac{2 N_d}{n_i} \right) \tau_g, \quad (7)$$

and thus

$$K_s = \frac{C_{ox}}{C_{df}} \left(\frac{2 N_d}{n_i} \right) K_g. \quad (8)$$

For the n-type devices used here, Eq. (8) yields a value for K_s/K_g of 1.0×10^6 as compared to the experimental value of 1.7×10^6 . Upon reducing the latter value by a factor of 0.75, we obtain 1.3×10^6 which is in reasonable agreement with the calculated value. For MOS capacitors on a p-type substrate, the experimental value of K_s/K_g is $\sim 7 \times 10^6$, which reduces to $\sim 5 \times 10^6$ when the 0.75 factor is applied. The calculated value for K_s/K_g in the p-type case is $\sim 7 \times 10^6$, which agrees reasonably well with the (reduced) experimental result.

We now discuss the reason for the large differences between generation-lifetime and recombination-lifetime damage coefficients. As noted above, values for K_g/K_r are ~ 70 (n-type) and ~ 35 (p-type). Qualitatively, this discrepancy is expected and two contributing factors can be cited to account for it. The first factor follows directly from consideration of a one-level Hall-Shockley-Read (HSR) model. It can be shown that for equal concentrations of recombination centers (in the neutral bulk) and generation centers (in the depletion region), the inequality $\tau_g \geq \tau_r$ must hold. If generation in the depletion region occurs

through the same level as recombination in the neutral bulk, and if this level is at midgap, then $\tau_g = \tau_r$. In general, one expects the dominant generation level to be at or near midgap but recombination is likely to be dominated by some other level, so that $\tau_g > \tau_r$, and thereby $K_g > K_r$. A second reason for expecting K_g to be greater than K_r involves the nature of neutron damage. For bulk material, neutron-produced disordered regions act as potential wells for minority carriers and enhance their recombination rate.^{48,49} The interior of such a region is near intrinsic, and thus its associated potential well will be nearly negligible in a depletion region. Defect levels introduced by neutrons will increase the carrier generation rate in a depletion region and thus decrease τ_g . However, the enhancing effect of disordered-region potential wells on bulk recombination appears to have no direct counterpart in a space-charge region. That is, no corresponding enhancement of carrier generation will occur beyond the simple addition of new generation centers. Thus, once again we expect K_g to be greater than K_r . At low injection levels, a defect within a disordered region is on the order of a factor of 5 to 10 times more effective for recombination than if it were isolated.⁵⁰ Clustered defects in a depletion region should tend, in terms of their effect on electrical properties, to resemble isolated defects. This recombination information thus suggests that the difference in values of K_g and K_r will be up to an order of magnitude larger than that expected on the basis of the above HSR argument. Taking these two effects together, the large difference noted here between K_g and K_r appears reasonable.

Measurements of storage time in MOS capacitors were made as a function of temperature for the purpose of gaining additional insight. Figure 4-7 shows storage time versus reciprocal temperature for two devices from lot KA-09. In the pre-irradiation case, band-to-band excitation is the dominant mechanism at high temperatures ($1000/T < 3.0$) as evidenced by an activation energy approximately equal to the bandgap energy. At lower temperatures, the temperature dependence is dominated by that of n_i . The activation energy at such temperatures is the same before and after bombardment which suggests that the energy level position of the dominant generation center is nearly the same in both cases.

To explore this point further, Zerbst analysis was performed on the C-t plots used to obtain the τ_s data in Figure 4-7. Results of this analysis are

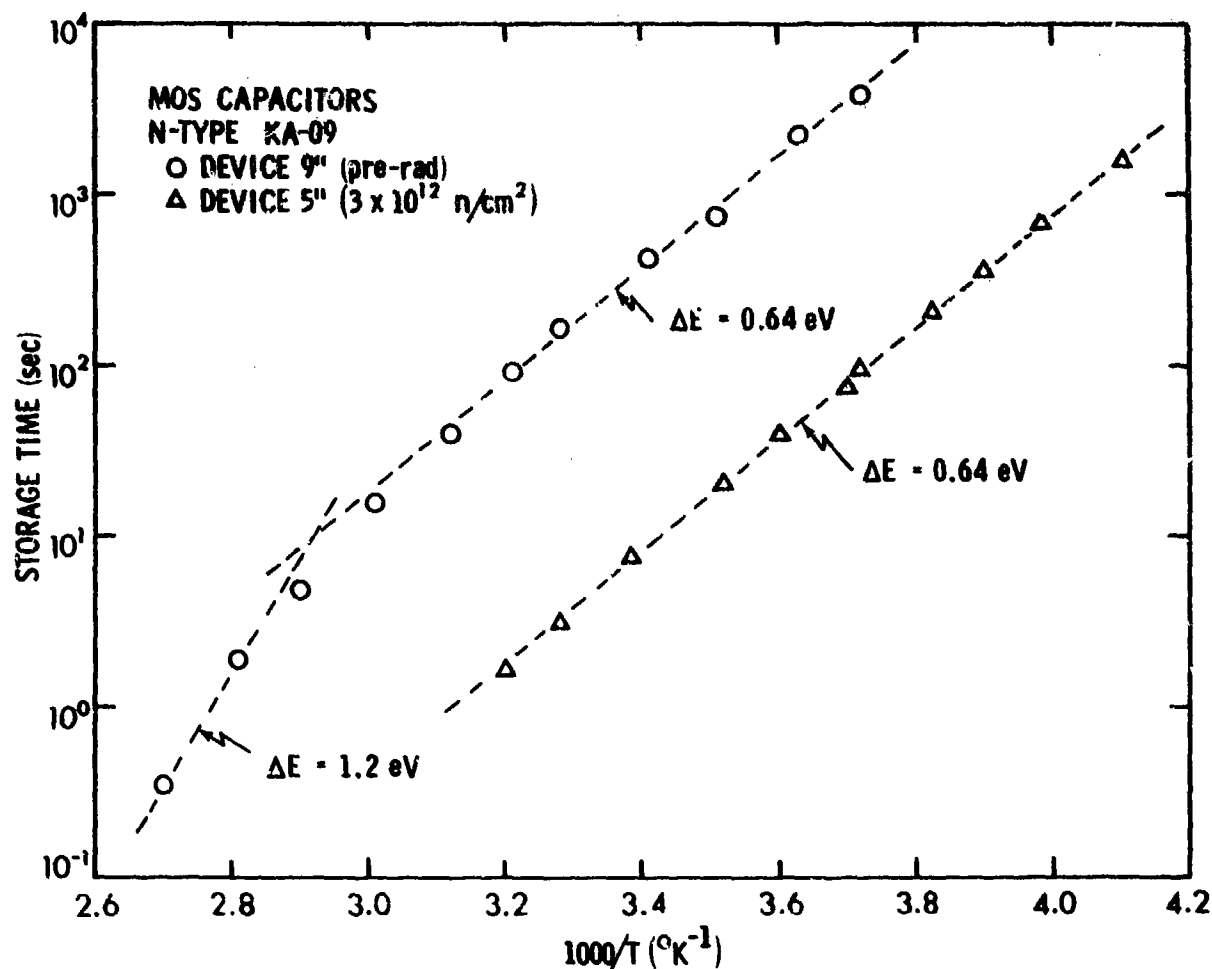


Figure 4-7. Storage time versus reciprocal temperature for irradiated and unirradiated MOS capacitors on an n-type substrate.

shown in Figure 4-8 where generation lifetime is observed to be only very weakly dependent on temperature both before and after irradiation. Such behavior is reasonable based on a one-level expression⁵¹ for τ_g :

$$\tau_g = \frac{c_p p_1 + c_n n_1}{2c_p c_n n_g n_i} \quad (9)$$

(All terms have their usual definition.) If the dominant generation level is at midgap, then $n_1 \cong p_1$ and the temperature dependence of n_1 (or p_1) will be equal to that of n_i . Therefore, this strong temperature dependence cancels, leaving only that of the capture probabilities. Capture probability temperature dependences typically are rather weak. The weak temperature dependences shown in Figure 4-8

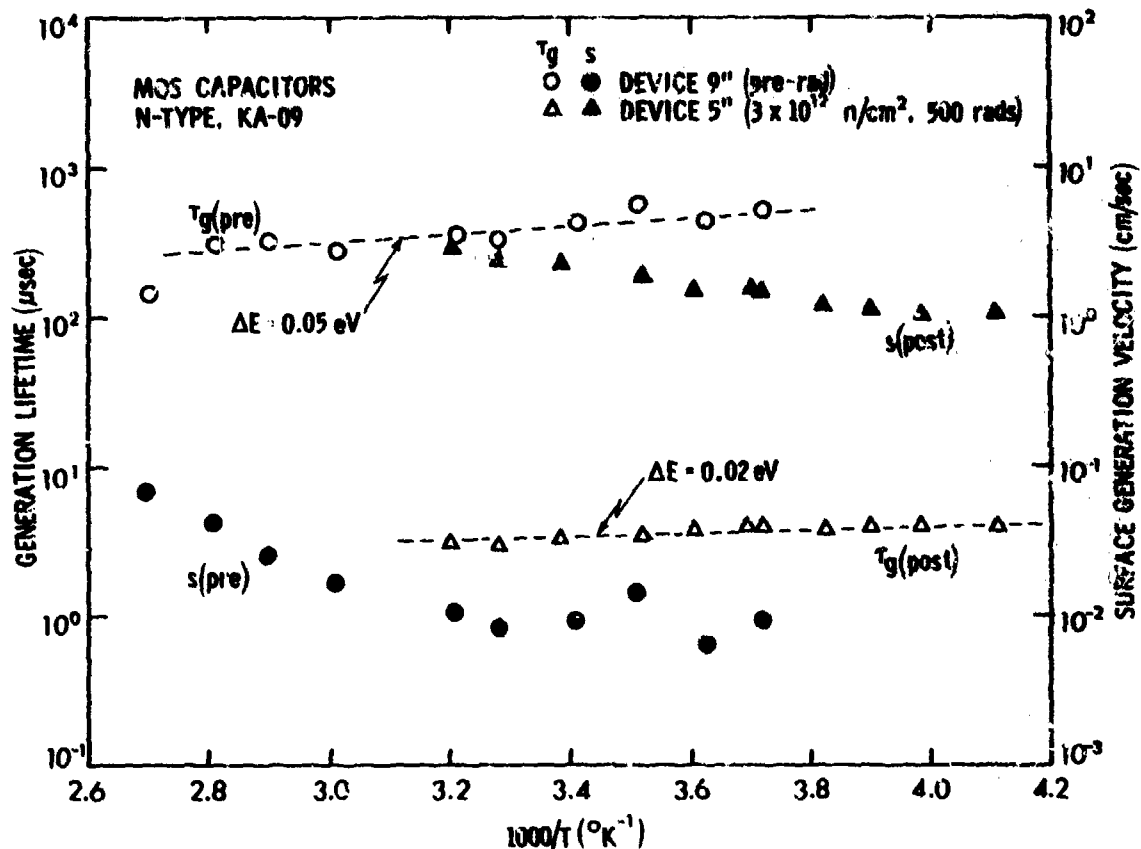


Figure 4-8. Generation lifetime and surface generation velocity versus reciprocal temperature for irradiated and unirradiated MOS capacitors on an n-type substrate.

are thus attributable either to capture probabilities or to a slight deviation of the dominant generation level from midgap. Since there is no strong difference between the temperature dependence pre- and post-irradiation, the indication is that the dominant radiation-induced generation level is coincident with (or very near) the corresponding pre-irradiation level. The results of Figure 4-8 also reveal that K_g is only very weakly temperature dependent over the range studied and that surface generation velocity is temperature dependent over portions of the range examined. The latter behavior can most likely be accounted for in terms of the temperature dependence of parameters associated with a generation level (or levels) at the SiO_2 -Si interface.

4.1.4 CCD Results

Figure 4-9 shows change in dark output voltage for several CCDs following both pulsed and steady-state neutron bombardment. These devices were unpowered during irradiation and dark voltage measurements were made using the

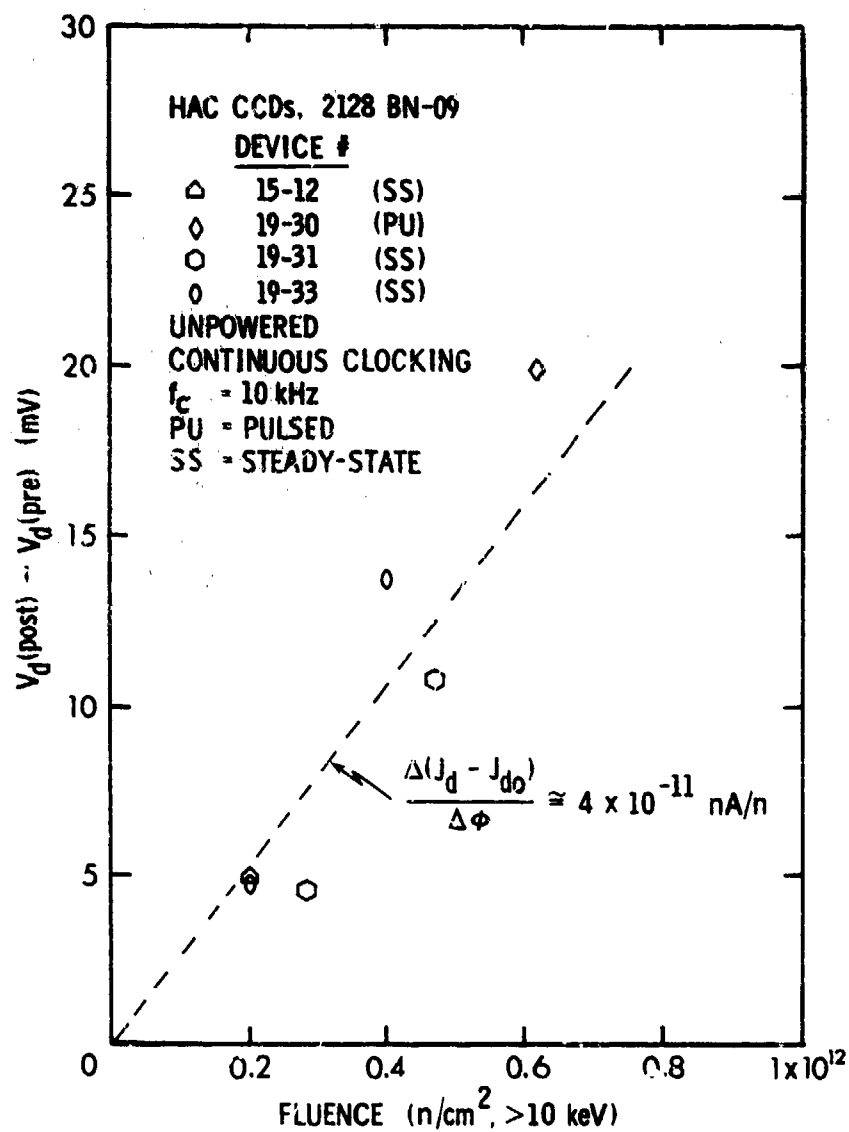


Figure 4.9. Change in dark output voltage due to both pulsed and steady-state neutron bombardment for CCDs irradiated in an unpowered mode.

continuous clocking method ($f_c = 10$ kHz) within one hour following bombardment. An approximately linear dependence of change in dark voltage on fluence is observed and a value for dark-current introduction rate $[\Delta(J_d - J_{d0})/\Delta\phi]$ of $\sim 4 \times 10^{-11}$ nanoamps per neutron results. Additional data, obtained by the integration method, yielded an introduction rate in agreement with this value.

An anomalous sensitivity for the present CCDs to radiation-induced increases in dark current was observed when devices were irradiated in a powered mode (continuous clocking, no input charge). Dark current increases were observed to be proportional (apparently) to neutron fluence to the 3.5 power. Further study revealed that this sensitivity was due to ionizing radiation and was not a neutron effect. The ionizing dose accompanying neutron bombardment in this study ranged from 10 to 500 rads (Si). Irradiation of an unpowered CCD in the gamma-ray environment of a Co^{60} source to a total dose of 100 rads produced no observable change in dark current. However, irradiation of a powered device in the same source to about the same total dose produced a dark current increase comparable to that produced during neutron bombardment. (These data are presented in Section 4.2.3.) In general, the data indicate a strong bias dependence of ionization-induced increases in measured dark current. It is not presently clear which region in the CCDs investigated exhibits an extreme total-ionizing-dose sensitivity. (One possibility is charge buildup in the radiation-sensitive field oxide which would then deplete the silicon and give rise to an additional source of dark current. Further discussion of this possibility is given below.) However, this effect is probably related to the present device design and/or processing procedures and therefore is most likely not of general interest. The results of Figure 4-9 are of general applicability in that the basic effect of neutrons on dark current in a CTD is illustrated. (See additional data in Section 4.2.4.)

Short-term annealing measurements of dark current in CCDs bombarded by a pulse of neutrons were attempted in this investigation. To perform such measurements, it is necessary to operate a given device with power applied during irradiation since active measurements are made as a function of time following the pulse. Because devices were powered, the observed response was dominated by the ionizing radiation effect mentioned above. Thus, information regarding the transient annealing behavior of generation centers in the depletion region of HAC CCDs was not obtained. (Such data for Fairchild devices are presented

in Section 4.2.4.) Since transient annealing of neutron damage in silicon is strongly dependent on the electron density present,⁵² one might expect the rate of dark-current recovery to be relatively slow since the carrier concentration in a depleted region is quite low.

Before having determined that the observed anomalous response of the present HAC CCDs, when irradiated under power, was an ionizing radiation effect, we performed an experiment to rule out the possibility that introduction of neutron damage in a depletion region is bias dependent. The following measurements were made on MOS capacitors on an n-type substrate. Devices were irradiated with a neutron burst (5.4×10^{11} n/cm²) under three bias conditions: (1) DC (-8.5V); (2) clocked (0 to -8.5V, 5 kHz square wave); (3) grounded gate. These conditions were repeated in a second experiment with unirradiated devices using a steady-state neutron flux to achieve the same fluence. Pre- and post-irradiation determinations of τ_s and τ_g were performed and damage coefficients then determined. Values for K_s were in good agreement with each other (and with the value given in Figure 4-4) for all conditions. The same statement also applies reasonably well for K_g values. We conclude that introduction of generation centers in a depletion region is independent of biasing condition, and in fact no such dependence was anticipated.

4.1.5 Discussion

It is of interest to calculate the expected increase in dark current for a neutron-irradiated charge transfer device. Dark current density J_d in a CCD due to generation of carriers in a depletion region of width x_d is given by⁵³

$$J_d = q n_i x_d / 2 \tau_g . \quad (10)$$

Using Eq. (4), we obtain

$$J_d = \frac{q n_i x_d}{2} \left(\frac{1}{\tau_{go}} + \frac{\phi}{K_g} \right) = J_{do} + \frac{q n_i x_d \phi}{2 K_g} , \quad (11)$$

and thus

$$\frac{d(J_d - J_{do})}{d\phi} = \frac{q n_i x_d}{2 K_g} . \quad (12)$$

At room temperature, $n_i = 1.4 \times 10^{10} \text{ cm}^{-3}$; from Figure 4-5, $K_g = 7.0 \times 10^6 \text{ n-sec/cm}^2$. The depletion region width is estimated to be on the order of 2 to 3 μm , which includes all of the 0.8 μm n-type epi layer plus a portion of the 30 $\Omega\text{-cm}$ p-type substrate.* This yields a calculated range for $d(J_d - J_{do})/d\phi$ of 3.2 to $4.8 \times 10^{-11} \text{ nA/n}$, in good agreement with the experimental value of $\sim 4 \times 10^{-11} \text{ nA/n}$ for devices irradiated in an unpowered condition. Thus, we have employed MOS capacitors to obtain the basic quantity (K_g) needed to predict neutron-induced increases in J_d in a CCD, and the resulting agreement between calculation and experiment is satisfying. We further note that K_g should be of general usefulness in predicting neutron damage effects in depletion regions for any silicon device bombarded by fission neutrons. (See Section 5.0.)

Table 4-2 compares values of $d(J_d - J_{do})/d\phi$ derived from data obtained by various workers with the present result. It should be borne in mind that values for this quantity are expected to be in agreement only if x_d is the same, based on Eq. (12), and also if all experimental conditions are the same. For purposes of comparison, we assume that x_d is approximately the same in all cases. The present data and that of Hartsell³³ and Chang³⁵ were obtained using a fission reactor, and their values for $d(J_d - J_{do})/d\phi$ agree within a factor of ~ 2 with the current value. The value obtained by Saks³⁴ is a factor of 5 higher than ours, which is consistent with the more effective introduction of generation centers by the higher energy neutrons he employed than the fission neutrons used here. In summary, the present value of $d(J_d - J_{do})/d\phi$ is in reasonable agreement with values derived from data obtained by Hartsell³³ and Chang,³⁵ the two cases for which comparison appears appropriate. One further comparison can be made. Williams and Nelson³² obtained a value for K_s of $3.3 \times 10^{13} \text{ n-sec/cm}^2$ using a p-surface-channel device (n-type substrate). This value falls midway between those shown in Figure 4-4 and thus is in reasonable agreement with the present work. However, this agreement may be fortuitous since τ_s (and therefore K_s) depends on the magnitude of the voltage step applied in a C-t measurement and on the doping concentration. Storage time and its associated damage coefficient do not have the fundamental physical significance that τ_g and K_g have.

Lowering the operating temperature of a charge transfer device causes a dramatic reduction in dark current due to the strong temperature dependence of carrier generation rate in the depletion region. Neutron bombardment introduces

*In subsequent work, described in Section 5.0 of this report, we concluded that the depletion region width is most likely larger than that used here.

Table 4-2. Comparison of values for $d(J_d - J_{do})/d\phi$ derived from data obtained by various workers.

Reference	$d(J_d - J_{do})/d\phi$ (nA/neutron)	Radiation Source	Comments
Hartsell ³³	$\sim 9.6 \times 10^{-11}$	Fast-burst reactor	Buried channel
	$\sim 5.6 \times 10^{-11}$	Fast-burst reactor	Surface channel
Saks ³⁴	1.9×10^{-10}	Cyclotron (0 to 30 MeV neutrons, 15-MeV peak)	Buried channel
Chang ³⁵	$\sim 2 \times 10^{-11}$	Fast-burst reactor	Buried channel and Surface channel
Present work	$\sim 4 \times 10^{-11}$	TRIGA reactor	Buried channel

generation centers in that region which give rise to an increase in dark current. The impact of this radiation-induced increase can be diminished by lowering the device operating temperature. We consider such a hardening approach here and present a graph that allows the selection of an operating temperature which should prevent post-irradiation dark current from being larger than some specific value.

The temperature dependence of J_d [Eq. (10)] is dominated by that of n_i , where

$$n_i = C_1 T^{3/2} \exp(-E_g/2kT) = C_1 f(T) . \quad (13)$$

(C_1 is a constant and E_g is bandgap energy.) Upon defining a second constant, C_2 , as $q x_d/2$, we obtain

$$J_d = J_{do} + \frac{C_1 C_2 f(T) \phi}{K_g} . \quad (14)$$

Plotting $\log f(T)$ versus reciprocal temperature yields a slope (i.e., an activation energy) of -0.58 eV. (For this determination, we employed $E_g = 1.11$ eV and the bandgap temperature dependence was neglected. This is reasonable over

the temperature range considered.) As noted above, τ_g is only weakly temperature dependent. Using the pre-irradiation value for the activation energy of τ_g in Figure 4-8 (0.05 eV) results in an overall temperature dependence for J_{do} of $\exp(-0.63 \text{ eV}/kT)$. This dependence is in good agreement with the τ_s data of Figure 4-7 and in exact agreement with pre- and post-irradiation data obtained for HAC CCDs (not shown here). For simplicity, we assume that the second term in Eq. (14) also varies as $\exp(-0.63 \text{ eV}/kT)$ and thus that J_d has this same dependence. This is a reasonable assumption since K_g is only weakly temperature dependent, as discussed above.

Upon normalizing J_d to J_{do} , we obtain

$$\frac{J_d}{J_{do}} = 1 + \frac{\tau_{go} \phi}{K_g}. \quad (15)$$

This expression was used at 303°K (i.e., $J_{do} \equiv 1$ before irradiation at $1000/T = 3.3^\circ\text{K}^{-1}$) to obtain values of normalized dark current density as a function of fluence using $K_g = 7.0 \times 10^6 \text{ n-sec/cm}^2$. A value of τ_{go} was selected (14 μsec) so that $\Delta J_d / \Delta \phi$ would equal $4 \times 10^{-11} \text{ nA/n}$ for $J_{do} = 20 \text{ nA/cm}^2$, a typical dark current density for the CCDs studied. Curves with a -0.63 eV slope were then drawn through the calculated room-temperature values and results are shown in Figure 4-10. This graph illustrates the effectiveness of lowering the operating temperature of a CTD to avoid neutron-induced dark current problems. As an example, assume that the maximum dark current density that be tolerated is unity, the value of J_{do} at 303°K in Figure 4-10. If the expected fluence is 10^{13} n/cm^2 , then this figure indicates that operating the device at $T \leq 269^\circ\text{K}$ will keep $J_d \leq$ unity following irradiation. Thus, a relatively moderate lowering of the operating temperature in a CTD should result in a substantial radiation tolerance in terms of neutron-induced increases in dark current.

4.1.6 Summary

A study of the mechanisms of neutron-induced dark current increases in charge transfer devices has been performed using MOS capacitors and CCDs as test vehicles. MOS capacitors were used to obtain neutron damage coefficients associated with storage-time and generation-lifetime degradation (K_s and K_g , respectively) and gamma-ray damage coefficients associated with increases in

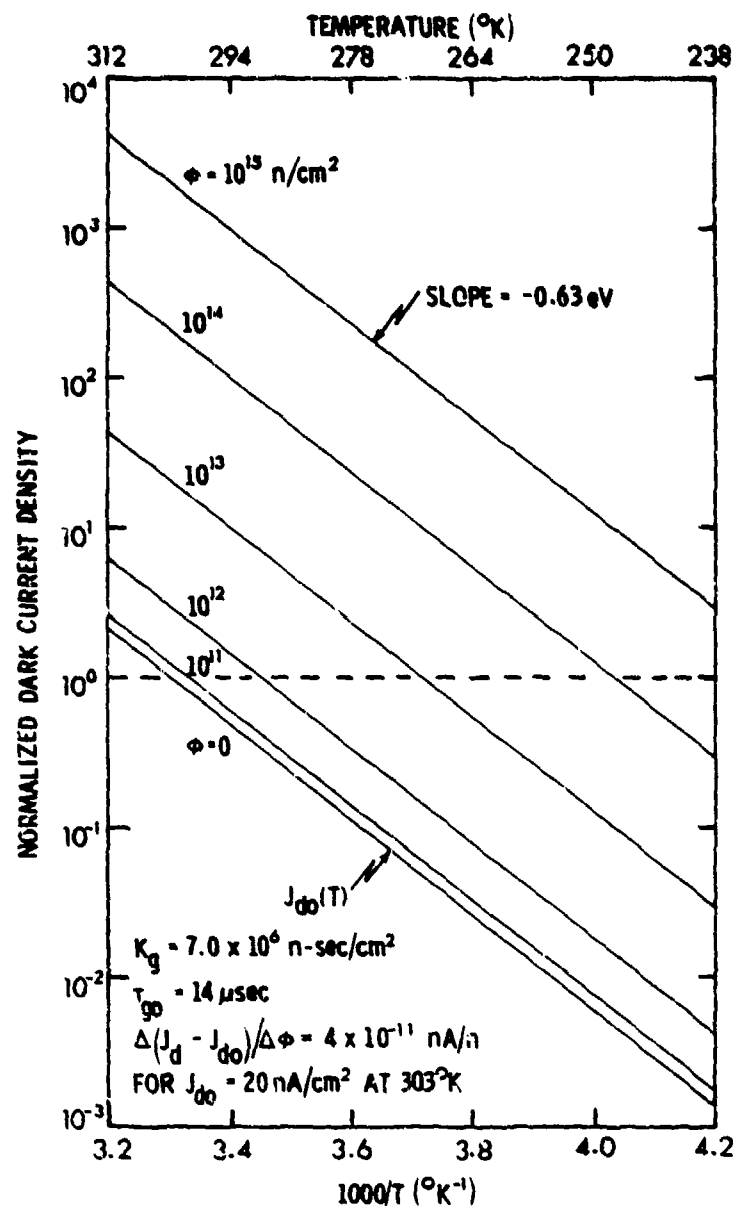


Figure 4-10. Normalized dark current density versus reciprocal temperature with neutron fluence as a parameter. The effect of a reduced operating temperature on radiation tolerance is illustrated.

surface generation velocity at the $\text{SiO}_2\text{-Si}$ interface. In terms of the radiation response of a buried-channel CCD, the quantity determined having the most fundamental significance is K_g , the generation lifetime damage coefficient. A unique value for this coefficient of $7.0 \times 10^6 \text{ n-sec/cm}^2$ was determined for devices on both n- and p-type substrates. This value was then used to calculate the expected change in dark current density with neutron fluence in a CTD. The calculated value is in good agreement with the present experimental value of $\sim 4 \times$

10^{-11} nA/n for irradiated CCDs. (See additional discussion of this point in Section 5.0.) Experimental values for the ratio of K_s/K_g were obtained and found to be greater than six orders of magnitude. These substantial differences were accounted for reasonably well for both n-type and p-type material using the model of Heiman.⁴⁷ A qualitative explanation was presented to account for the substantial difference between recombination-lifetime and generation-lifetime damage coefficients which is based on consideration of the Hall-Shockley-Read model and also on the nature of neutron damage in a depletion region. A discussion was presented which indicates that a moderate reduction in operating temperature of a CTD should substantially reduce its sensitivity to the production of dark current by neutron bombardment.

4.2 ADDITIONAL STUDIES OF RADIATION EFFECTS ON CHARGE-COUPLED DEVICES

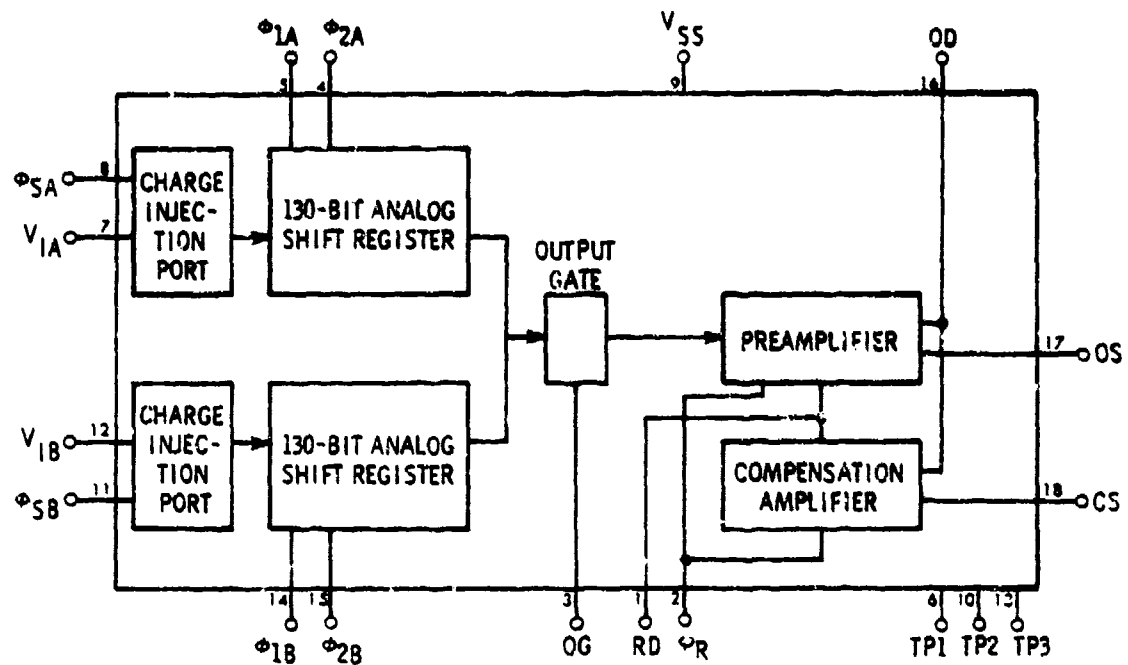
4.2.1 Introduction

Section 4.1 of this report describes results of studies of radiation effects on CCDs performed during the first half of the performance period for the present contract. In this section, we present findings obtained during the second half of the program. In addition, data are presented which serve to reinforce and provide further insight regarding several of the points briefly made above. The primary subjects included here are: a) effects of ionizing radiation on Hughes Aircraft and Fairchild CCDs; b) transient and permanent effects of neutron bombardment on the Fairchild CCD 311. As in Section 4.1, emphasis is placed here on investigation of radiation-induced increases in dark-current density.

4.2.2 Experimental Procedures

Techniques used to measure dark current were the same as those described in Section 4.1.2.3. The radiation facilities employed were the TRIGA Reactor and the Co^{60} source at Northrop Research and Technology Center. All measurements were made at room temperature, which was monitored. Data were corrected to 298°K based on the measured temperature dependence of dark-current in CCDs, as mentioned above. Two types of n-buried-channel CCDs were studied: devices fabricated by Hughes Aircraft (described in 4.1.2.1 and in References 35 and 54) and the commercially available Fairchild CCD 311. Figure 4.11 shows a block diagram of and pin identification for the CCD 311. Note that this device contains two 130-bit analog shift registers which normally are multiplexed. We operated the clocks for these two shift registers 180° out of phase so that dark-current information for both was obtained simultaneously. Also note that the CCD 311 uses a two-phase clock whereas the Hughes Aircraft device operates with four-phase clocking.

Pertinent schematic diagrams of circuits employed in conjunction with the CCD 311 are now presented. Figure 4-12 shows a diagram of the circuit used in radiation testing (both reactor and Co^{60}). This circuit permits active measurements to be made during pulsed or steady-state irradiation. The drive circuit illustrated in block form in Figure 4-12 is shown in detail in Figure 4-13. Figure 4-13a depicts the clock waveform and signal input generator. In Figure 4-13b, the circuit used to provide power for the CCD 311 and for the



PIN NAMES	
ϕ_{1A} , ϕ_{2A} , ϕ_{1B} , ϕ_{2B}	Analog Shift Register Transport Clocks
OG	Output Gate
OS	Output Transistor Source
OD	Output Transistor Drain
CS	Compensation Transistor Source
ϕ_R	Reset Transistor Gate Clock
RD	Reset Transistor Drain
V_{SS}	Substrate (Ground)
V_{IA} , V_{IB}	Analog Input Gates
ϕ_{SA} , ϕ_{SB}	Analog Sample Clocks
TP1, TP2, TP3	Test Points

Figure 4-11. Block diagram of and pin identification for the Fairchild CCD 311.

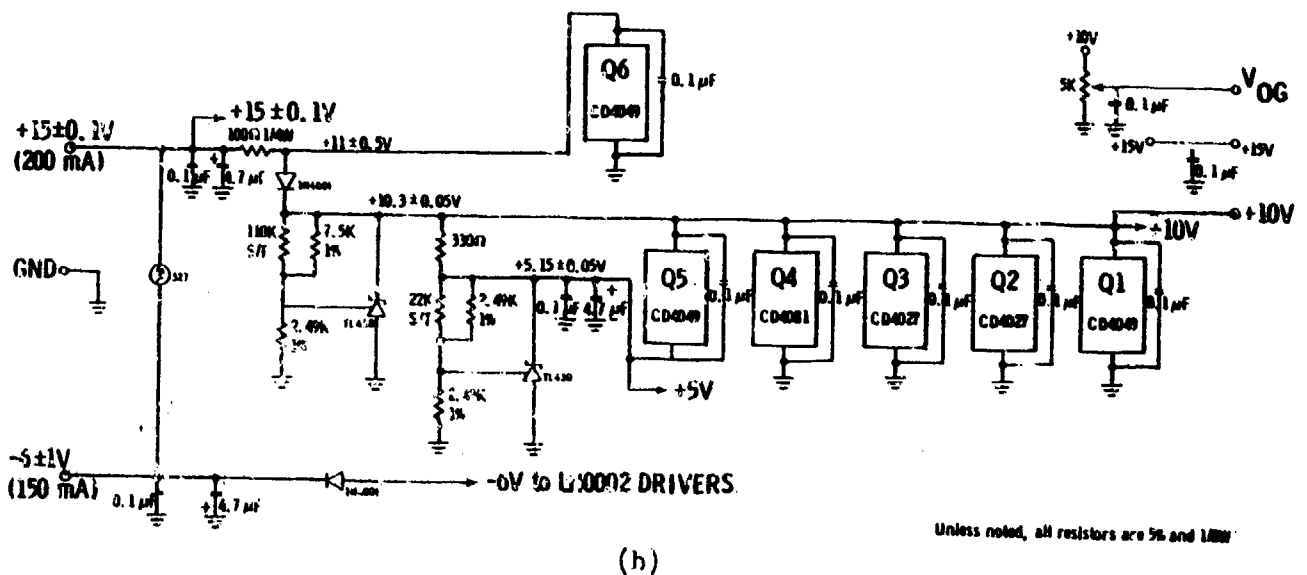
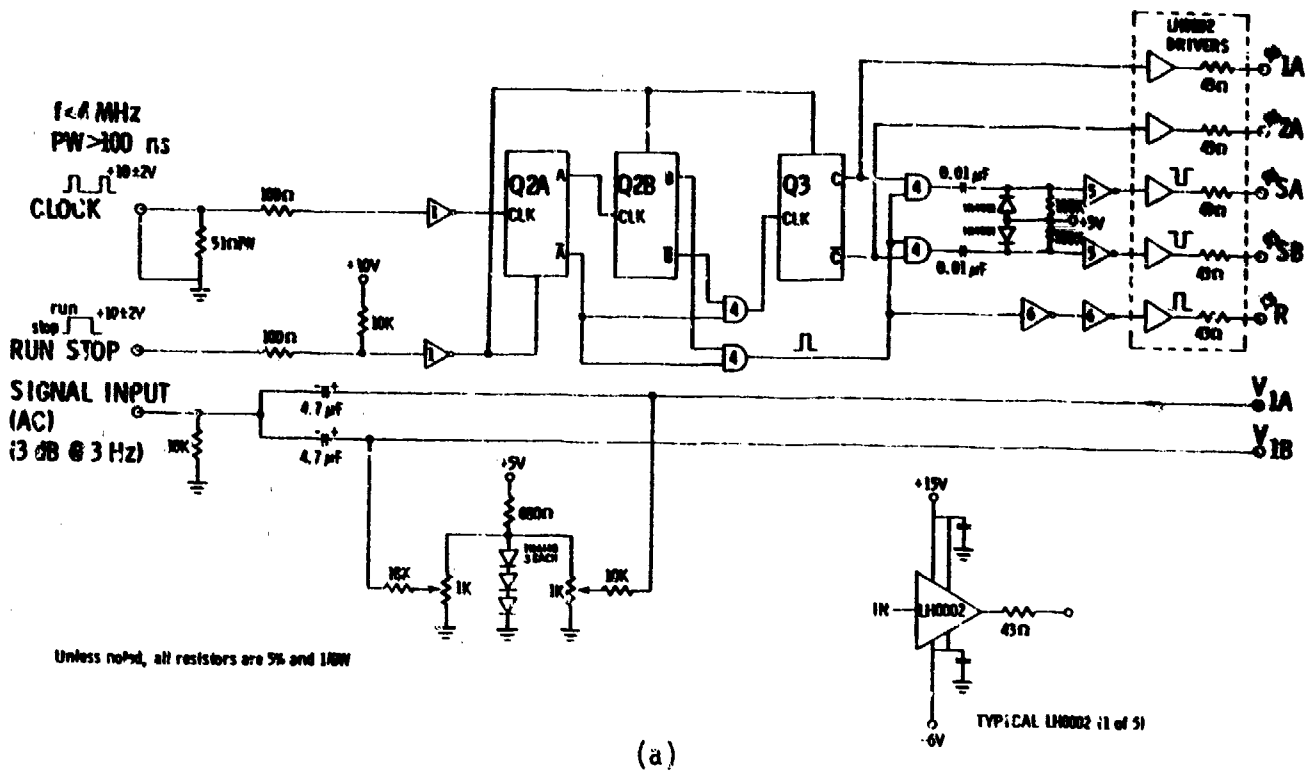


Figure 4-13. Drive circuit for the Fairchild CCD 311:

- Clock waveform and signal input generator;
- Circuit to provide power for the CCD 311 and for the circuit shown in Figure 4-13a.

circuit of Figure 4-13a is presented. A timing diagram showing waveforms applicable for the circuit of Figure 4-13a is given in Figure 4-14. Details of the pin connections for the CCD 311 during irradiation are shown in Figure 4-15. Figure 4-16 shows the differential amplifier circuit used to eliminate the reset pulse at the output (refer to Figure 4-12). In Figure 4-17, the drive amplifiers used in testing the CCD 311 are illustrated.

4.2.3 Ionizing Radiation Effects

As mentioned briefly in Section 4.1.4, dark current density in Hughes Aircraft CCDs was found to be quite sensitive to ionizing radiation when devices were irradiated in a powered mode. We present here the data which led to that conclusion along with additional results of ionizing irradiation studies.

A schematic diagram of the Hughes Aircraft buried-channel CCD studied is shown in Figure 4-18. (A similar design is used in the Fairchild part.) In earlier work,⁵⁵ we noted that the apparent sensitivity of the HAC CCD to neutron bombardment was greatly enhanced if the device was irradiated with power applied. These previous data are shown in Figure 4-19 where the change in output dark voltage (proportional to dark current) is plotted versus neutron fluence. The open symbols represent data for powered devices and the solid symbols are for unpowered parts. ("Powered" is defined here as the application of typical ac and dc voltages to all appropriate terminals of the CCD with the exception of the input. No charge was input to the CCD for the purpose of permitting dark current measurements by either of the methods described in Section 4.1.2.3. The "unpowered" condition refers to irradiation of a CCD with all of its leads imbedded in conductive foam.)

An extreme sensitivity of the powered parts as compared to the unpowered units is evidenced in Figure 4-19. Ionizing radiation is also incident on the CCDs during neutron bombardment, so we performed an experiment to determine whether the sensitivity of dark current in parts irradiated under power was a neutron effect or an effect of ionizing radiation. During neutron bombardment, CaF_2 TLDs were used to measure the concomitant ionizing dose. Figure 4-20 shows the data of Figure 4-19 replotted in terms of change in dark voltage versus total dose. Also shown are data points obtained for HAC CCDs irradiated in a Co^{60} source. Device 19-41 had received no previous irradiation. It was

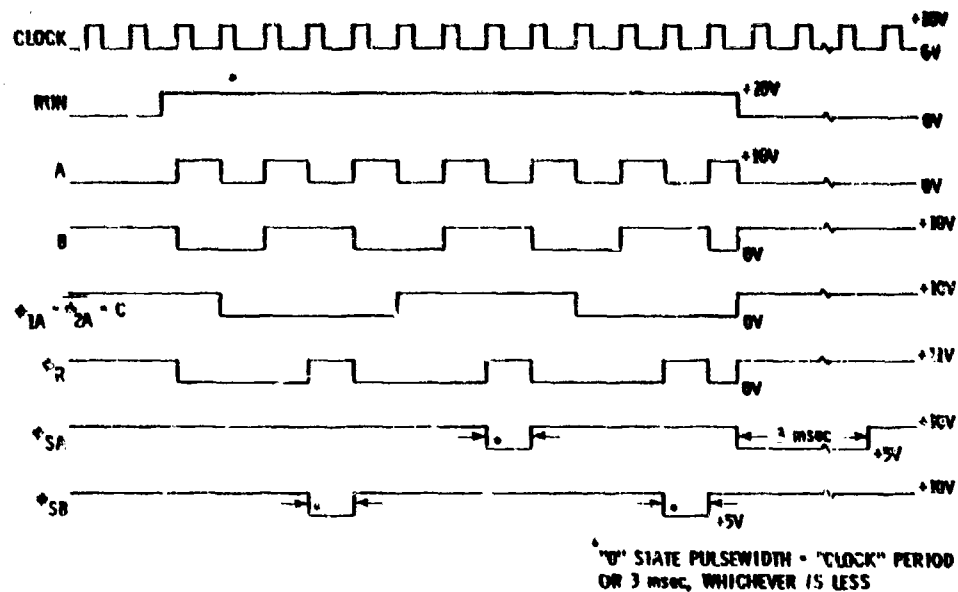


Figure 4-14. Timing diagram for the CCD 311. Waveforms applicable for the circuit of Figure 4-13a are shown.

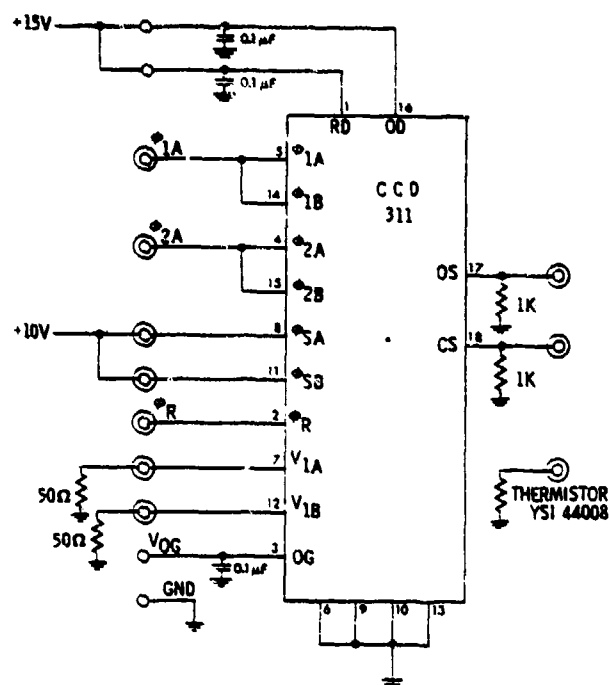


Figure 4-15. Pin connections for the CCD 311 during irradiation. (See Figure 4-12.)

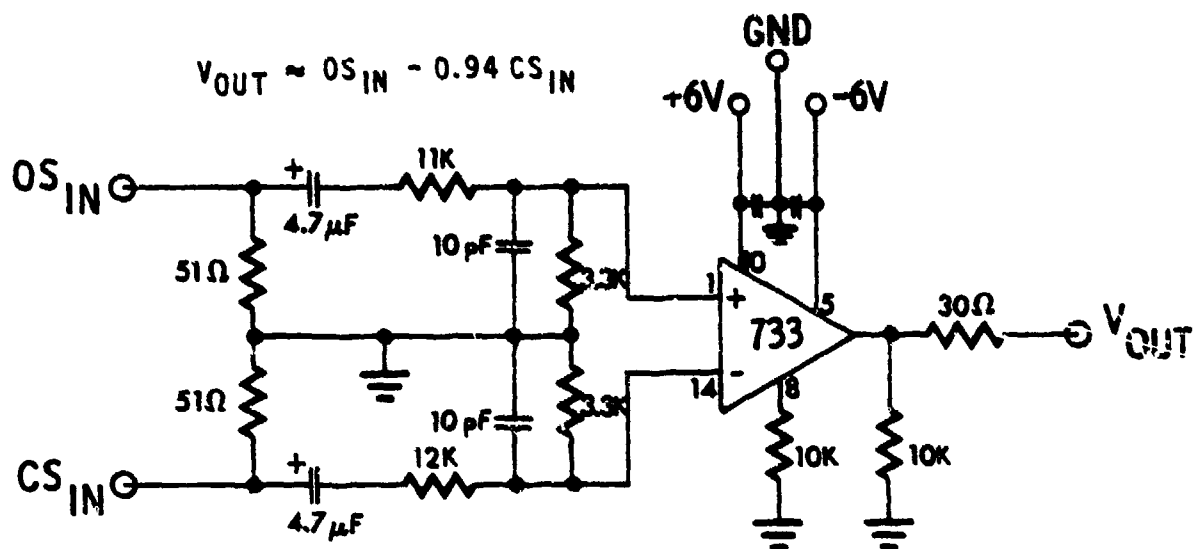


Figure 4-16. Differential amplifier used with the CCD 311 to eliminate the reset pulse at the output. (See Figure 4-12.)

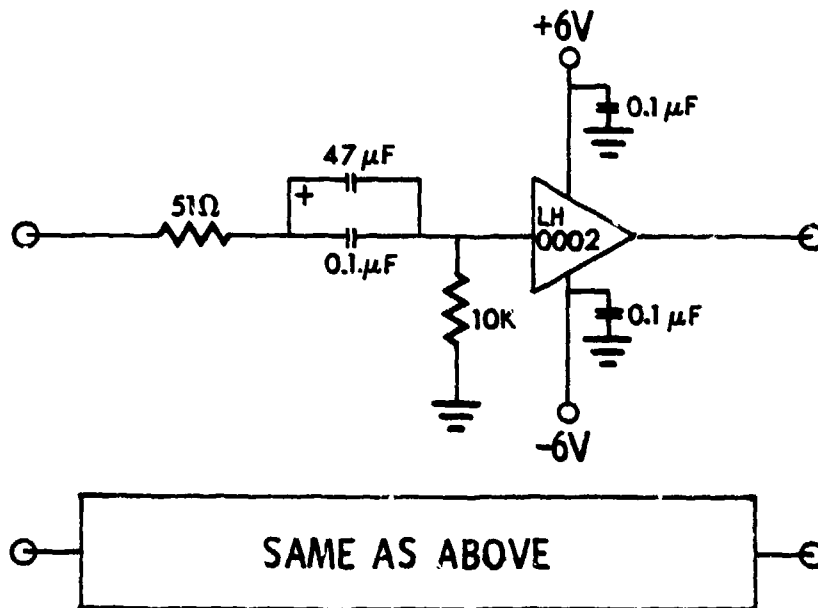


Figure 4-17. Drive amplifiers used with the CCD 311. (See Figure 4-12.)

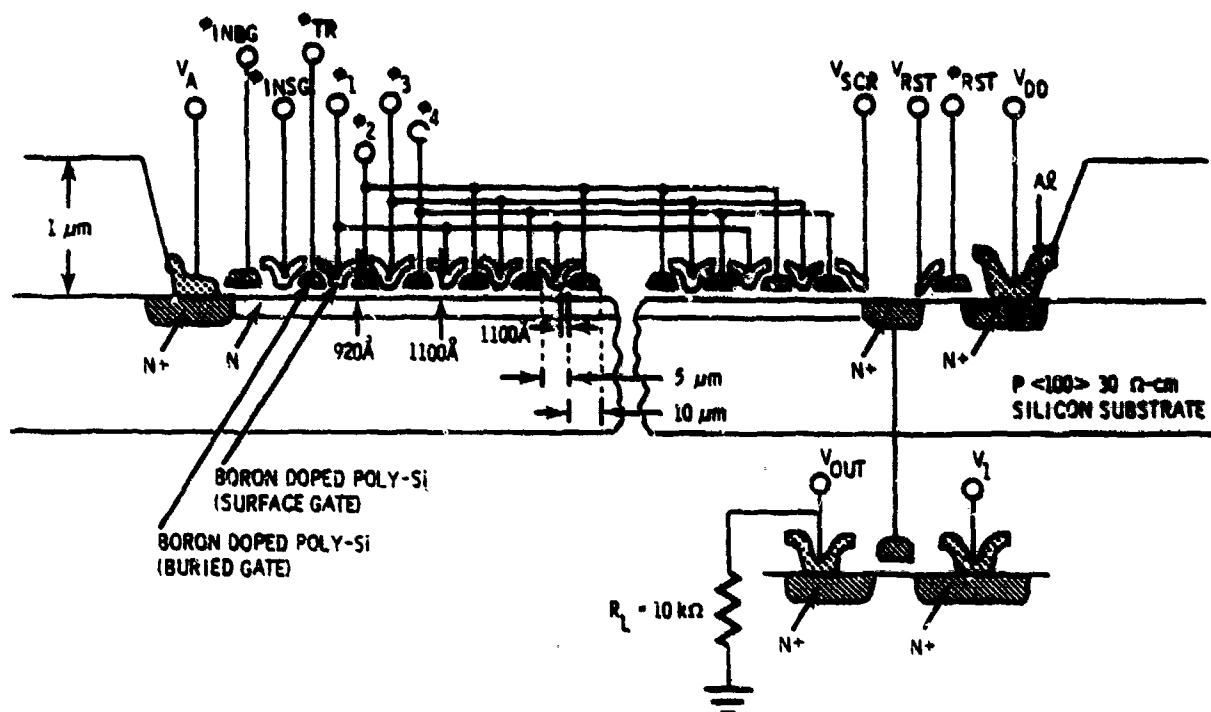


Figure 4-18. Schematic diagram of the Hughes Aircraft buried-channel CCD.

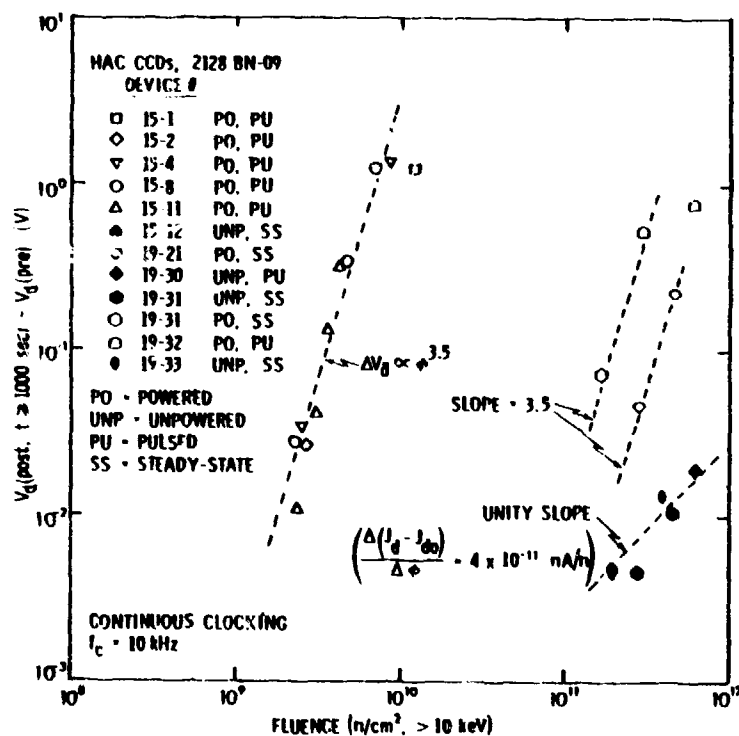


Figure 4-19. Radiation-induced change in dark output voltage for the Hughes Aircraft CCD. Although dark voltage is plotted versus neutron fluence, only the solid data points are attributable to neutron damage. (See text.)

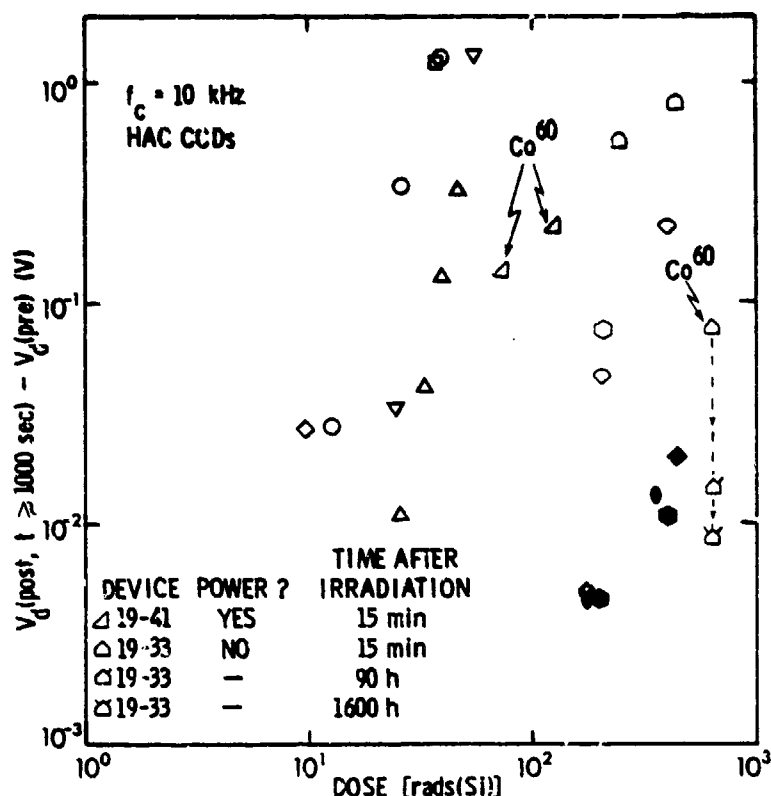


Figure 4-20. Change in dark output voltage versus ionizing dose for the Hughes Aircraft CCD. Except for the two designated "Co⁶⁰", all data points shown are those given in Figure 4-19. In the present case, the ionizing dose received during neutron bombardment is plotted as the abscissa.

first irradiated to 130 rads with power applied and the resulting change in dark voltage was substantial, as shown in Figure 4-20. The 130-rad data point shown for this device is in general agreement with those shown for other devices from wafer #19. This result reveals that the extreme sensitivity of dark current in powered HAC CCDs is an effect of ionizing irradiation, and not of neutron bombardment. After a 16h anneal at room temperature, V_d for Device 19-41 decreased to 65% of the 130-rad value shown in Figure 4-20. This anneal was followed by an additional irradiation under power to a dose of 75 rads. The change in dark voltage at 10 kHz as a result of this irradiation was 140 mV. This result is plotted in Figure 4-20 in terms of the incremental dose and the incremental change in V_d (i.e., 75 rads and 140 mV). The result of this second irradiation of Device 19-41 is consistent with that obtained in the first bombardment.

In a second experiment, Device 19-33 was irradiated in the Co^{60} source with no power applied. This device had been previously neutron irradiated twice and had received ionizing doses of 180 rads (unpowered) and 170 rads (powered). Three months later the Co^{60} experiments were performed, and at that time the dark current density for this device was 50% larger than its pre-irradiation (virgin) value. The first unpowered gamma irradiation was to a total dose of 100 rads, and no change in dark current was observed. This result indicates that the ionizing-radiation sensitivity of HAC CCDs to ionizing radiation arises only when power is applied. However, a second unpowered irradiation of Device 19-33 to an additional 660 rads caused V_d to increase significantly, as shown in Figure 4-20. (Also shown are results of long-term room-temperature anneals of 90 and 1600 hours. Significant recovery was noted.) This result could cause one to suspect that the solid data points in Figures 4-19 and 4-20 (also shown in Figure 4-9), which are results of neutron bombardment in an unpowered state, are attributable to the effects of both neutrons and gamma rays. However, results of neutron bombardment of the Fairchild CCD 311 (discussed below), which is insensitive to ionizing radiation (also discussed below), are consistent with findings shown in Figure 4-9 for unpowered HAC CCDs. That is, we judge the solid data points in that figure to be attributable solely to the effects of neutrons. It is possible that results of Co^{60} bombardment of Device 19-33 were influenced by the fact that it had previously been irradiated with power applied. Further study would be required on virgin devices to clear up this issue. (Exploration of this point was not of primary importance in the present program.)

For comparison purposes, Fairchild CCD 311s were irradiated in the Co^{60} source with and without power applied. Results are shown in Figure 4-21 where dark current density is plotted versus total dose. Devices 1 and 2 were irradiated unpowered. Device 1 was still functioning at 10^5 rads (the highest dose examined for this unit), and the increase in dark current density was only ~20%. Device 2 was still operational at 3×10^5 rads but failed somewhere between that dose and 10^6 rads. Devices 23 and 25 were irradiated under power. Device 23 exhibited a strong increase in dark current (saturated) at 5×10^4 rads and failed to operate after 8×10^4 rads. Device 25 failed at 9×10^4 rads. It is interesting to note that the Fairchild CCD was not intentionally fabricated as a radiation-hardened part but it exhibits moderate tolerance to ionizing radiation.

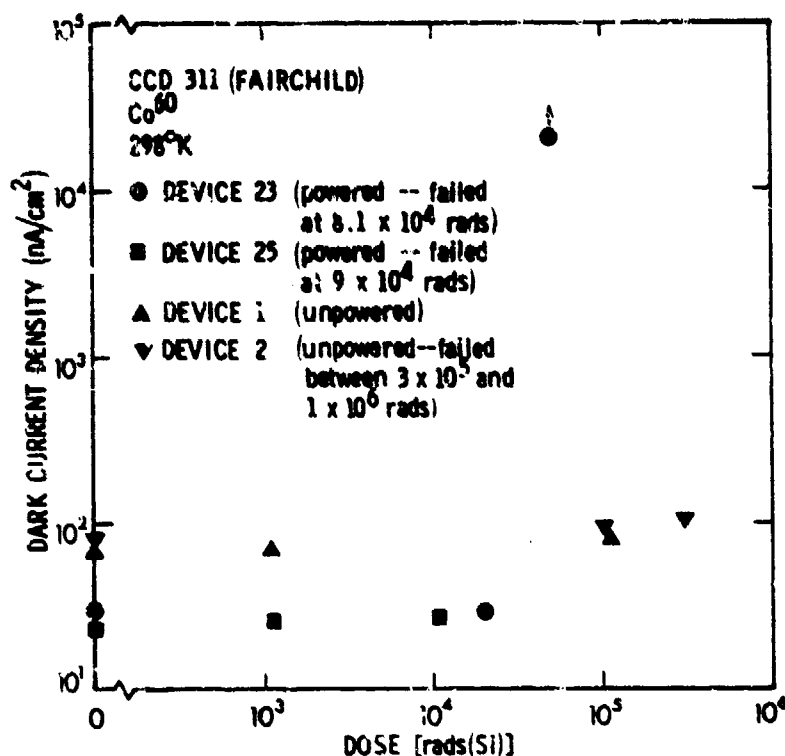


Figure 4-21. Dark current density versus ionizing dose for the Fairchild CCD 311.

To explore further the sensitivity of HAC CCDs to ionizing radiation, additional measurements were made. Figure 4-22 shows dark current density versus total dose for three HAC devices irradiated with power applied. The results are rather striking and deserve considerable comment. Before doing so, some experimental differences should be noted. Devices 19-62 and 17-65 were previously unirradiated whereas Device 19-21 had received an earlier neutron-plus-gamma irradiation (see Table 2 in Reference 55). In that earlier irradiation, dark current was observed to recover to within a factor of two of its pre-irradiation value after a thirty-day room-temperature anneal. It is not presently clear whether the irradiation history of Device 19-21 had an effect on the later experiment (Figure 4-22), i.e., gave rise to the difference between results for this unit and the other two devices. However, this aspect of the data is unimportant for the present purposes. We concentrate here on the trends evident, and results shown for all three devices in Figure 4-22 are qualitatively similar. One additional difference was that Device 19-21 was operated at a constant clock frequency (500 kHz) during irradiation whereas

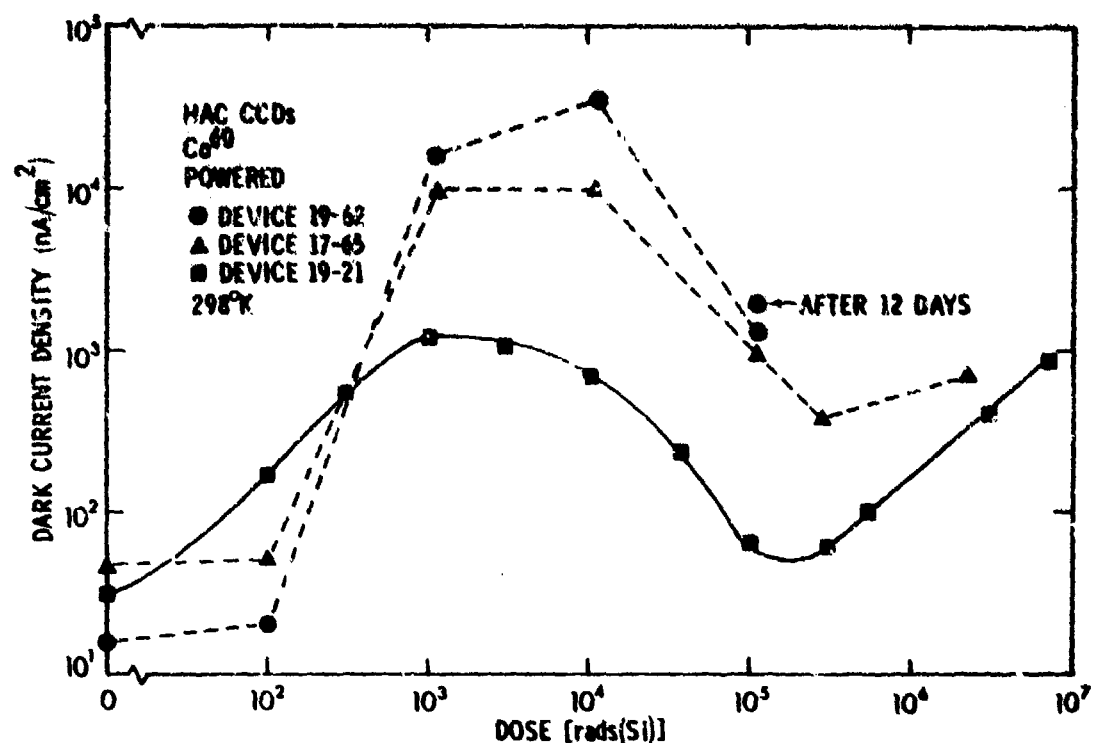


Figure 4-22. Dark current density versus ionizing dose for Hughes Aircraft CCDs.

the clock frequency was varied for Devices 19-62 and 17-65. This difference in procedure is probably not of importance. A final note regarding experimental procedures: the dark current measurements of Figure 4-22 were made with the Co^{60} source lowered into the floor (i.e., dose rate equal to zero). With the source raised, the presence of ionizing radiation enhances the dark current and also produces noise in the measurement system.

Three dark-current regimes are evident in Figure 4-22. A strong increase in J_d is noted in the range $10^2 - 10^3$ rads. This is followed by a strong decrease in J_d in the range $10^3 - 10^5$ rads. In the third regime ($>10^5$ rads), J_d once again exhibits an increase. This third regime is reasonably well understood and is attributable to two effects: 1) an increase in the generation center density in the depletion-region bulk due to bombardment by the $\sim 1\text{-MeV}$ Co^{60} gamma rays; 2) an increase in the generation center density at the $\text{SiO}_2\text{-Si}$ interface due to production of interface states by the ionizing radiation. (Note that the first effect is production of displacement damage by ionizing radiation). Both of these effects should increase linearly with dose. Figure 4-23

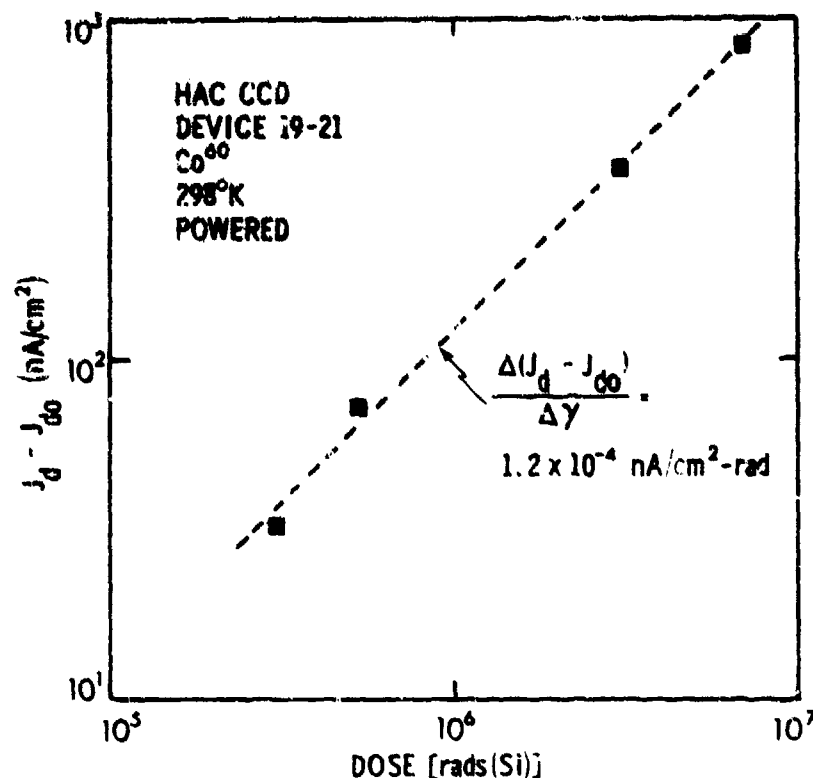


Figure 4-23. Change in dark current density versus ionizing dose for a Hughes Aircraft CCD. Data shown were derived from Figure 4-22.

shows the change in dark current density (i.e., $J_d - J_{d0}$) versus dose for Device 19-21 (data from Figure 4-22), and a linear dependence is indeed observed. The rate of change obtained is 1.2×10^{-4} nA/cm²-rad. To examine how well that rate describes data obtained by other workers, we have made the comparison illustrated in Figure 4-24. Data derived from the work of Chang and Aubuchon^{35,54} are shown, along with a dashed line corresponding to the rate of change obtained in Figure 4-23. There is considerable scatter in the experimental data, which is perhaps due in part to the fact that some of the data were obtained with bias applied and the rest without bias. Radiation-induced production of interface states should be enhanced by the application of a field across the gate oxide.⁵⁶ There is a slight indication in Figure 4-24 that powered devices exhibited a larger increase in dark current density, but further study is needed to confirm this point. (In the present program, we irradiated a HAC CCD in the Co⁶⁰ source with no power applied up to a dose of 3×10^6 rads. Dark current exhibited a linear increase with dose at high doses. However,

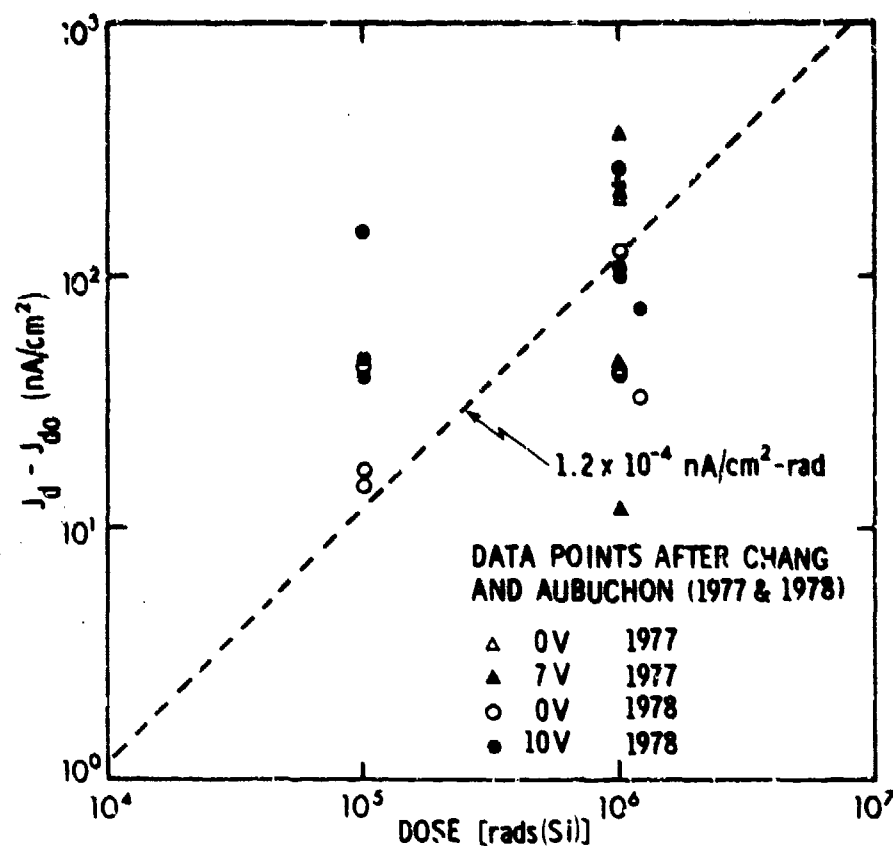


Figure 4-24. Change in dark current density versus ionizing dose. 35,54
Data points were obtained from the work of Chang and Aubuchon.
The dashed line is based on the fit to data shown in Figure 4-24.

the rate of change observed was a factor of ~ 3.5 larger than that shown in Figure 4-23. Clearly, additional investigation of the bias dependence of ionizing radiation effects on CCDs at high doses is needed. In this zero-bias experiment, unfortunately no data points were recorded for doses less than 10^5 rads. In retrospect, such data would have been useful in view of the discussion above in conjunction with Figure 4-20.) Note that at 10^6 rads in Figure 4-24 the dashed line passes roughly through the middle of the scattered data points, indicating some success in predicting the experimental observations. At 10^5 rads, the data points are all higher than the dashed line and this may be due to remanence of a portion of the anomalous enhanced current evident at lower doses (Figure 4-22). We now discuss this anomalous current.

The strong increase in dark current density at low doses, shown in Figure 4-22, is qualitatively consistent with the data shown in Figure 4-20. In the

former case, the ionizing dose was obtained from a Co^{60} source whereas in the latter case the ionizing radiation was concomitant with neutron bombardment. A starting point for a model which has potential for describing these findings is now given. The HAC CCDs contain a non-radiation-hardened field oxide, as shown in Figure 4-18. Not shown there is a channel-stop diffusion that is also present. Figure 4-25 is a schematic of the field oxide and the channel stop. A relatively small total ionizing dose can give rise to significant positive charge buildup in a field oxide.⁵⁷ This effect is enhanced if a bias is applied across that oxide layer. Positive charge buildup will result in formation of a depletion region in the underlying p-type substrate. Thermal generation of carriers will occur in this region and these carriers could substantially increase the CCD dark current if they were able to couple into the channel. However, the channel stop should prevent this from occurring. At higher doses, negatively charged interface states will form at the field oxide-silicon interface, as shown in Figure 4-25. This negative charge will serve to compensate for built-up positive charge in the oxide, thereby reducing the extent of the depletion region in the silicon. Thus, fewer carriers would be thermally generated in that region at higher doses. Once again, the problem with this model is that it is not clear how carriers thermally generated external to the CCD channel can couple into the channel and enhance the dark current. The anomalous response of HAC CCDs to ionizing radiation is most likely associated with a device processing problem that has yet to be determined. Further study of the effects of processing variations on this response will most likely be required before the observed phenomena can be understood and counteracted.

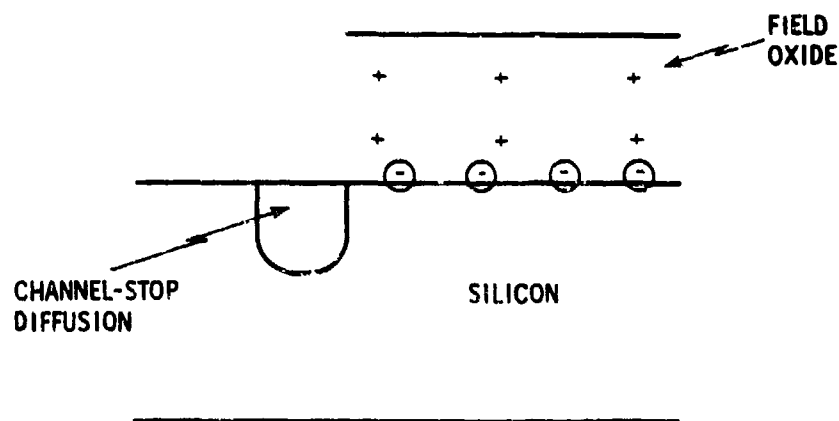


Figure 4-25. Illustration of charge buildup in the field oxide for a CCD.

One final point should be noted regarding data shown in Figure 4-22. For Device 19-62, dark current density was measured after a 12-day post-irradiation anneal at room temperature. Dark current increased by 50% over this period of time, as shown in the figure. This behavior indicates that annealing of the radiation "damage" responsible for the decrease in J_d in the $10^4 - 10^5$ rads range proceeds at a faster rate than annealing of the "damage" responsible for the dark-current increase in the $10^2 - 10^3$ rads range. Qualitatively, such behavior appears inconsistent with the model depicted in Figure 4-25 since the amount of radiation-induced positive charge in SiO_2 tends to decrease with time following irradiation whereas the interface-state density tends to remain constant or increase over the same time regime for a thermal-oxide/silicon interface.⁵⁶ (To determine whether this statement applies for a field-oxide/silicon interface would require further study.)

4.2.4 Neutron Effects

The relative absence of ionizing radiation effects on dark current density in the Fairchild CCD 311 as compared to the HAC CCD makes it a good test vehicle for examining neutron effects on CCDs powered during bombardment. Results of neutron irradiations of the CCD 311 are reported here. In the first experiment, five separate devices were irradiated unpowered to five different fluences, and dark current measurements were made before and after these steady-state irradiations. (Post-irradiation measurements were performed within approximately one hour after bombardment.) Figure 4-26 is a plot of the change in dark current density versus neutron fluence. Data over a fairly wide fluence range are fit quite well by a unity-slope line as shown in the figure. The slope obtained, 3.5×10^{-11} nA/neutron, compares quite well with the result for the HAC CCD shown above in Figure 4-9. (Additional discussion of these results is given in Section 5.3 of this report.)

Measurements of dark current density were performed as a function of time following pulsed neutron bombardment for the CCD 311. In the first experiment performed, Device J6 was operated at a clock frequency of 2 kHz during bombardment, and the continuous clocking method was used to monitor dark current as a function of time. This device was bombarded by two neutron pulses a few hours apart. Both bursts were ~20 msec wide (\$1.90 pulse) and shielding was as follows: 1/4" bora¹ plus 4.3" Pb. In addition, for the first pulse 7" of water shielding was employed to reduce the fluence. No water shielding was used on the

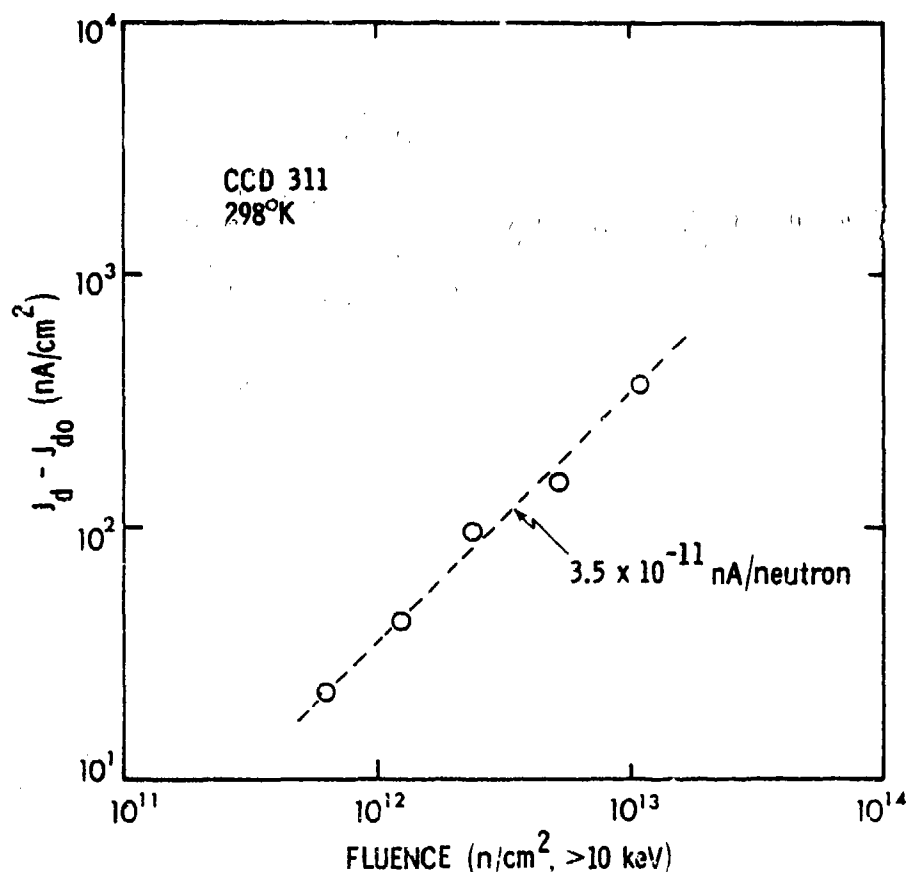


Figure 4-26. Change in dark current density versus neutron fluence for the Fairchild CCD 311.

second burst. Sulphur pellets were used for neutron dosimetry and CaF_2 TLDs were employed to obtain total ionizing dose. With no water shielding, the plutonium-to-sulphur ratio is known to be 11.9 for our shielding conditions. We obtained a fluence of $4.4 \times 10^{11} \text{ n/cm}^2$ ($>10 \text{ keV}$) for the second pulse (gamma dose $\approx 130 \text{ rads(Si)}$). For 7" H_2O shielding, the plutonium-to-sulphur ratio is estimated to be ~ 9 and we thereby obtained $\sim 2.6 \times 10^{10} \text{ n/cm}^2$ ($>10 \text{ keV}$) as the fluence for the first burst (gamma dose $\approx 60 \text{ rads(Si)}$).

Figure 4-27 shows dark current density versus time for Device J6 following the two neutron pulses described above. Data are displayed for the time regime 7-2400 sec after each burst. Following the first pulse, no useable information was obtained at times less than 7 sec on any of the four oscilloscope channels employed. This occurred because of inappropriate choice of gain settings. (It was clear, however, that the dark current signal exhibited erratic behavior for $t < 7 \text{ sec}$.) The pre-irradiation value of dark current density for Device J6 at 298°K was 4.6 nA/cm^2 . At 2400 sec after the first neutron burst ($\sim 2.6 \times 10^{10} \text{ n/cm}^2$), the value of J_d at that same temperature

was 5.4 nA/cm^2 , so only slight permanent damage was incurred. At 2400 sec following the second burst ($4.4 \times 10^{11} \text{ n/cm}^2$), $J_d = 27.7 \text{ nA/cm}^2$ as shown in Figure 4-27. At 7 sec, J_d is a factor of 2.7 larger than this value.

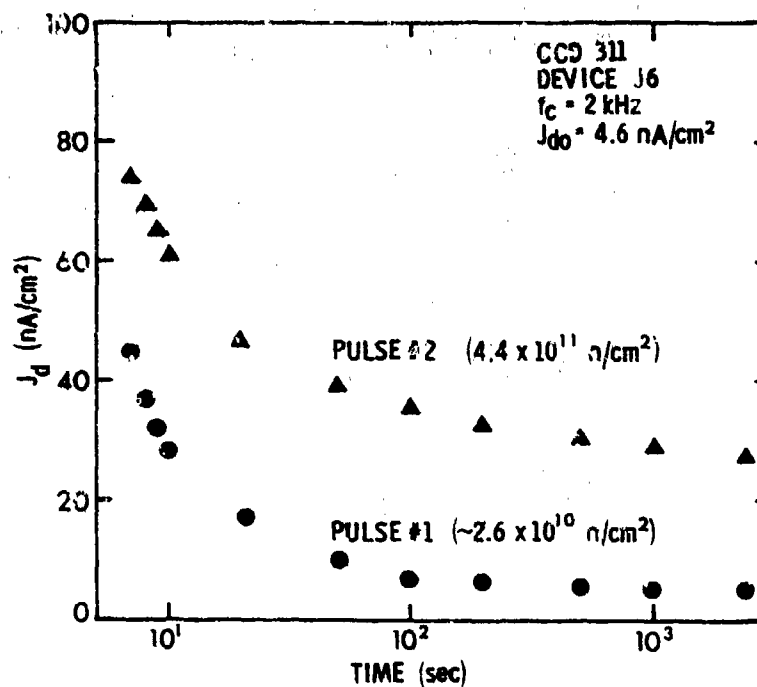


Figure 4-27. Dark current density versus time following pulsed neutron bombardment for the Fairchild CCD 311 (Device J6).

For times less than 7 sec after pulse #2, several phenomena were observed. As an aid to describing the observations, let the value of J_d at 7 sec be equal to x . For $t < 0.2$ sec, no definitive information was obtained, but it is likely that the CCD wells were saturated at such times due to ionizing radiation associated with the burst. At $t = 0.2$ sec, the two shift registers in Device J6 had a significantly different dark current. One register had a relative J_d of $2.5x$ whereas the second had a value of $12x$. Between 0.2 and 1.9 sec, J_d decreased monotonically (and significantly). At $t = 1.8$ sec, for the first register $J_d = 1.3x$ and for the second register $J_d = 6x$. At $t = 2$ sec, control rod reentry occurs, thereby reducing the amount of ionizing radiation incident on the device. Thus, dark current decreases at this point. (See Reference 55 for additional discussion of the contribution of ionization to J_d in CCDs before reentry of the control rod occurs.) At $t = 2.2$ sec, $J_d = 1.2x$

and $1.6 \times$ for the first and second registers, respectively. Between $t = 2.2$ and 5.8 sec, J_d remained constant and the difference between the two registers was maintained. Between $t = 5.8$ and 7 sec, a transition occurred in which the dark current for both registers became equal and also J_d began to decrease with time. We interpret the data as follows. For $t \geq 7$ sec, J_d is dominated by thermal generation of carriers at neutron-produced centers in the depletion region bulk. As time increases, defect reordering occurs, thereby reducing the effective generation center density (i.e., J_d decreases). For $t < 2$ sec, J_d is dominated by ionizing events for this device. Between 2 and 7 sec, apparently electrical stability of the CCD is being restored subsequent to the large signals experienced at earlier times. (In this regard, we performed an experiment on an unirradiated CCD 311 and observed a recovery time constant of 1 to 2 sec when the clock frequency was abruptly doubled. The initial frequency was low enough so that the dark output voltage was saturated. Doubling the frequency reduced V_d , but it took 1 to 2 sec before steady-state (i.e., constant V_d) conditions were reached. This result indicates that one must exercise caution when interpreting early-time data in short-term annealing experiments on CCDs.)

Since we interpret the data of Figure 4-27 in terms of transient annealing of neutron damage, further analysis was performed in a manner analogous to previous studies of short-term recovery in neutron-irradiated silicon devices.⁵⁸ We define a dark-current annealing factor (AF) as follows:

$$AF = \frac{J_d(t) - J_{do}}{J_d(\infty) - J_{do}} \quad (15)$$

In this equation $J_d(t)$ is dark current density at any time t following pulsed neutron bombardment, J_{do} is the pre-irradiation value, and $J_d(\infty)$ is the value at some long time following bombardment (2400 sec for the data of Figure 4-27).

Figure 4-28 shows AF versus time for Device J6 based on the data of Figure 4-27. A substantial difference is noted between results for pulse #1 and pulse #2. One may question the validity of this difference since the amount of permanent damage induced by the first pulse was relatively small. Thus, in Equation (15) we have a relatively small difference between relatively large numbers in the denominator, so a moderate degree of experimental error

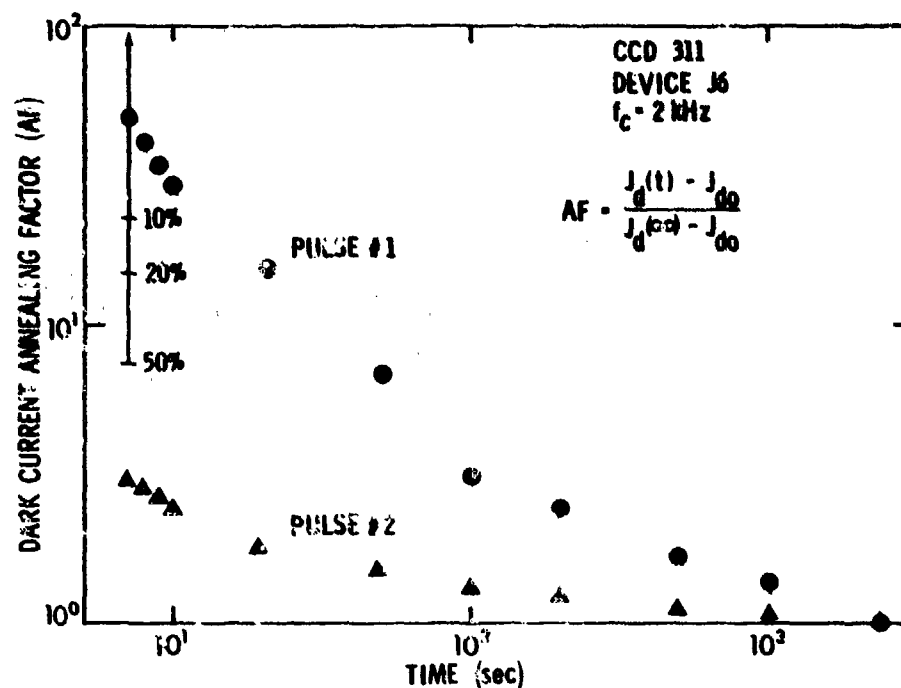


Figure 4-28. Dark current annealing factor versus time for the Fairchild CCD 311. Data shown were derived from Figure 4-27.

can have a large impact on the annealing factor. However, this impact is stronger in the direction of a larger AF as opposed to the direction of closer agreement between the two data sets in Figure 4-28. To examine how much experimental error would be required for the data obtained following pulse #1 to bring that data set into better agreement with the results obtained after pulse #2, we varied $J_d(\infty)$ and J_{d0} . For example, assuming 10% error, AF was recalculated by increasing $J_d(\infty)$ by 10% and decreasing J_{d0} by 10%. This constitutes a worst-case error situation in which the AF calculated from measured values overestimates the actual AF. An error bar is shown in Figure 4-28 at 7 sec corresponding to 10% error. Also shown are 20% and 50% error bars. We estimate that the error in J_d measurements for our experiments was no larger than $\pm 20\%$, and most likely was considerably smaller. Even if the error was $\pm 50\%$, AF after pulse #1 would still be significantly larger than that obtained after pulse #2. Hence, the discrepancy evident in Figure 4-28 appears to be real, but additional low-fluence data would be required to confirm it.

There is also a potential problem with the pulse #2 AF data in Figure 4-28. Measured dark voltage at early times (i.e., 7 sec) was very close to the maximum

value that can be obtained in normal operation from the device studied. This situation resulted because of the relatively low clock frequency employed. The question arose whether the pulse #2 AF data were influenced by the approach of dark voltage to near its saturation value. That is, we suspected that at early times the device was not in a linear operating range so that the variation of V_d with frequency was nonlinear. To avoid the possible effects of saturation, additional measurements were made on a second CCD 311 (Device J3) at higher clock frequencies.

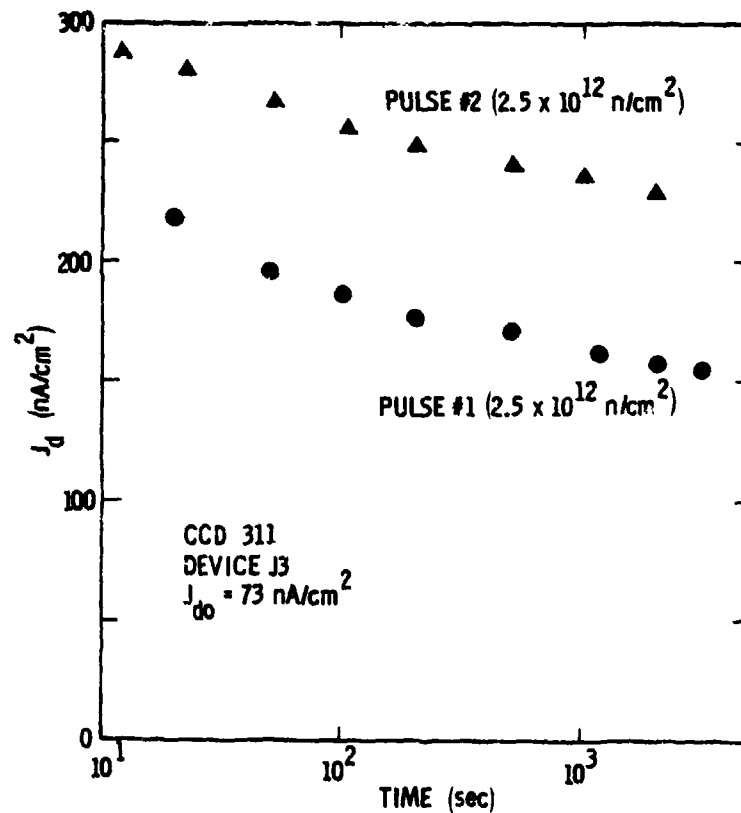


Figure 4-29. Dark current density versus time following pulsed neutron bombardment for the Fairchild CCD 311 (Device J3).

Figure 4-29 shows J_d versus time following two identical neutron bursts [2.5×10^{12} n/cm² (> 10 keV), (2.90 pulse, ~10 msec width, gamma dose \approx 330 rads (Si))] for Device J3. Note that the pre-irradiation dark current density (73 nA/cm²) is considerably larger than that for Device J6, so that a considerably higher fluence was required for J3 to cause a significant increase in dark current. For pulse #1, the clock frequency during bombardment was 200 kHz. This frequency was sufficiently high to keep V_d substantially less than its

saturation value at early times following bombardment. At $t = 15$ sec, the clock frequency was decreased to 20 kHz for the purpose of increasing the signal amplitude during later-time measurements. For pulse #2, the clock frequency was 500 kHz during bombardment and was decreased to 50 kHz at $t = 2$ sec.

Figure 4-30 shows AF versus time for the two data sets of Figure 4-29 (Device J3). Agreement between the results for pulse #1 and pulse #2 is good. Also shown in Figure 4-30 are AF results for Device J6 (pulse #2) taken from Figure 4-28. For $t \geq 20$ sec, agreement among the three data sets is good, which suggests that the true dark-current AF at, for example, 20 sec is ~ 1.7 as compared to the value of 30 obtained for Device J6 after pulse #1 (Figure 4-28). There is still the possibility of a fluence dependence of the transient annealing behavior at low fluences, but such a dependence appears unlikely in view of the agreement shown in Figure 4-30 for Devices J3 and J6. (We also note that no fluence dependence of short-term annealing in neutral bulk silicon was observed previously.⁵⁹)

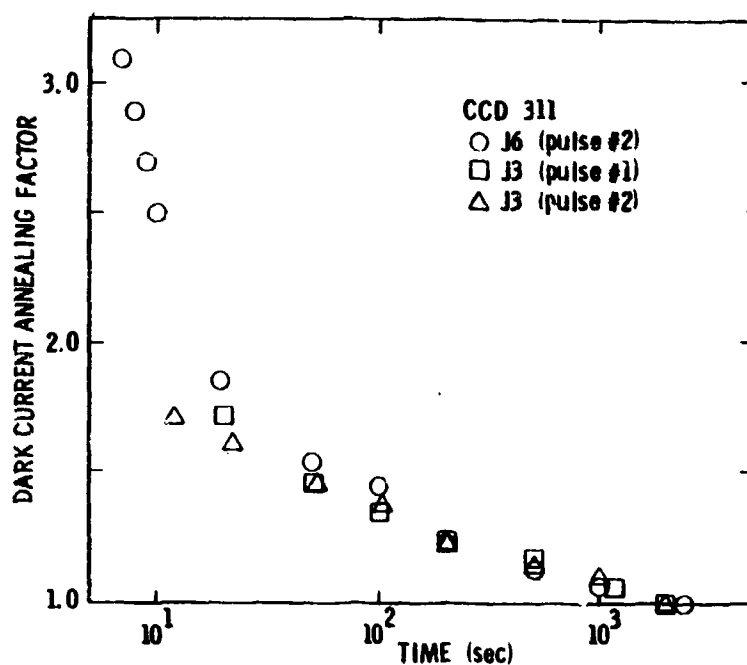


Figure 4-30. Dark current annealing factor versus time for the Fairchild CCD 311. Data shown were derived from Figures 4-28 and 4-29.

It is of interest to compare the observed change in J_d at long times following pulsed bombardment with the predicted change based on data in Figure 4-26, and such a comparison is made in Table 4-3. The experimental data

Device #	Pulse #	Fluence (n/cm^2)	Measured ΔJ_d (nA/cm^2)	Calculated ΔJ_d (nA/cm^2)
J6	1	$\sim 2.6 \times 10^{10}$	0.80	0.91
J6	2	4.4×10^{11}	22.3	15.5
J3	1	2.5×10^{12}	82.4	87.5
J3	2	2.5×10^{12}	83.3	87.5

Table 4-3. Comparison of measured and calculated "permanent" changes in dark current density for irradiated CCD 311s. Measured values are based on the value for J_d at times ≥ 2000 sec following pulsed neutron bombardment (see Figures 4-27 and 4-29). Calculated values are based on the slope shown in Figure 4-26 (3.5×10^{-11} nA/n).

are taken from Figures 4-27 and 4-29, and the calculated values were obtained using $\Delta J_d / \Delta \phi = 3.5 \times 10^{-11}$ nA/n. Agreement between measured and calculated values for ΔJ_d is good, which demonstrates that permanent increases in J_d by neutron bombardment can be predicted quite well for the CCD 311. Regarding prediction of the transient behavior of J_d , the AF at a given time can be used for this purpose. For example, $AF \approx 1.7$ at 20 sec following bombardment, so the appropriate value of $\Delta J_d / \Delta \phi$ to use at that time is $(1.7)(3.5 \times 10^{-11})$, or 6×10^{-11} nA/n. The basis for this calculation is obvious upon inspection of Equation (15).

The dark-current annealing factors shown in Figure 4-30 are significantly larger at times > 10 sec than those observed for neutral bulk regions in bulk silicon and silicon devices.^{58,59} For example, in the neutral-region case at 20 sec AF ranges from 1.0 to ~ 1.2 . For the depletion-region situation (i.e., dark current annealing) $AF \approx 1.7$ at that time. Short-term annealing is

strongly dependent on injection level in neutral material.⁶⁰ On this basis, one might speculate that the higher AF in the depletion-region case is due to the extremely low free-carrier density in that region. However, since the CCD gates were clocked during the transient recovery period, most of the depletion region is collapsed (i.e., becomes neutral material) for one-half the time. It is possible that the portion of the depleted region which does not collapse is responsible for the relatively slow transient recovery observed. Further study will be required to clarify this point.

4.2.5 Summary.

In this section, results of an investigation of neutron and ionizing radiation effects performed during the second half of this program have been presented. Principal findings are as follows. The HAC CCD is quite sensitive to the effects of ionizing radiation when irradiated under power. Dark current density for this device exhibits a strong increase in the range $10^2 - 10^3$ rads, followed by a significant decrease in the range $10^4 - 10^5$ rads. At higher doses, J_d increase linearly with dose and this is attributable to production of generation centers in the depletion-region bulk and to production of electronic states at the $\text{SiO}_2\text{-Si}$ interface. Dark current in the Fairchild CCD 311 was relatively insensitive to ionizing irradiation, both in unpowered and powered conditions, up to $\sim 10^5$ rads, where device failure was observed. Studies of the transient and permanent effects of neutron bombardment on the CCD 311 were performed. The rate of change of dark current density with neutron fluence was found to be 3.5×10^{-11} nA/neutron for measurements made approximately one hour after steady-state neutron irradiation. Short-term annealing measurements were performed in which dark current density was monitored as a function of time following pulsed bombardment. As an example, at 20 sec after irradiation the dark current annealing factor was ~ 1.7 . This means that the appropriate value for $\Delta J_d / \Delta \phi$ at that time for the CCD 311 is 6×10^{-11} nA/n as opposed to the long-term value of 3.5×10^{-11} nA/n.

SECTION 5.0

NEUTRON DAMAGE COEFFICIENT FOR SILICON DEPLETION REGIONS

5.1 INTRODUCTION

A damage coefficient appropriate for the introduction by neutrons of carrier generation centers in a silicon depletion region has been determined, as described in Section 4.1 of this report. There it was suggested that this damage coefficient might be generally useful for predicting the effects of neutron bombardment on silicon devices. In the present section, we explore that possibility. A presentation of the analytical background is given first, followed by a comparison of calculations with experimental results obtained on silicon devices at several laboratories.

5.2 ANALYTICAL CONSIDERATIONS

The expression for the steady-state net recombination rate R at a single level in neutral bulk material is given by the Hall-Shockley-Read model as

$$R = \frac{c_n c_p N_r (pn - n_i^2)}{c_n (n + n_1) + c_p (p + p_1)} \quad (1)$$

In this expression, p and n are hole and electron concentrations, c_p and c_n are hole and electron capture probabilities, n_i is the intrinsic carrier concentration, N_r is the recombination center concentration, and n_1 is the electron concentration that would exist if the Fermi level were located at the recombination level. (A similar definition holds for p_1 .) In the space-charge region of a reverse-biased p-n junction, $p, n \ll n_i$. Also, for a level near midgap, $n_1, p_1 \approx n_i$, so that $n, p \ll n_1, p_1$. Equation (1) thus reduces to the following expression for the thermal generation rate G of carriers at generation centers in a depletion region:⁵¹

$$G = - \frac{c_n c_p N_g n_i^2}{c_n n_1 + c_p p_1} \quad (2)$$

(N_g is the generation center concentration.) Generation lifetime τ_g is a characteristic time associated with the thermal generation of carriers and is given by⁵¹

$$\tau_g = \frac{c_n n_1 + c_p p_1}{2 c_n c_p N_g n_i} . \quad (3)$$

Thus, the generation rate is given by⁵¹

$$G = - n_i / 2 \tau_g . \quad (4)$$

(See additional discussion of this relation in Section 5.4.) The current density in a reverse-biased p-n junction due to thermal generation of carriers in a depletion region of width x_d is given by

$$J_g = \int_0^{x_d} q |G| dx \cong q |G| x_d = \frac{q n_i x_d}{2 \tau_g} . \quad (5)$$

(The approximation is due to the assumption of a uniform generation rate over the entire depleted region. See further discussion in Section 5.4 on the validity of Eq. (5).)

The generation current density J_g typically dominates reverse current flow in a silicon p-n junction below $\sim 100^\circ\text{C}$.⁵¹ In certain device structures, it is possible for carrier generation at interface states to be an important component of reverse current. We assume for simplicity here that dark (or leakage) current in neutron-irradiated silicon devices is dominated by J_g . The primary effect of neutron bombardment is to decrease τ_g due to introduction of generation centers in the depletion region. As noted in Section 4.1, this degradation process can be expressed as

$$\frac{1}{\tau_g} = \frac{1}{\tau_{g0}} + \frac{\phi}{K_g} . \quad (6)$$

In this expression, τ_{g0} and τ_g are pre- and post-irradiation values of generation lifetime, respectively, ϕ is neutron fluence, and K_g is generation-lifetime damage coefficient. Substituting (6) into (5), we obtain

$$J_g = \frac{q n_i x_d}{2} \left(\frac{1}{\tau_{g0}} + \frac{\phi}{K_g} \right) = J_{g0} + \frac{q n_i x_d \phi}{2 K_g} , \quad (7)$$

and thus the neutron-induced change in generation current density is given by

$$J_g - J_{g0} = q n_i x_d \phi / 2 K_g . \quad (8)$$

As described in Section 4.1 of this report, capacitance-versus-time measurements were made on MOS capacitors before and after neutron bombardment. Zerbst analysis was used to obtain generation lifetime, and the resulting data are repeated here for convenience (Figure 5-1). Linear degradation of τ_g is evident over a wide range in fission neutron fluence. Also, results for devices fabricated on n- and p-type material are in agreement. The value of K_g which describes the data in Figure 5-1 quite well is 7.0×10^6 neutron-sec/cm². We also found (see Section 4.1) that τ_{g0} and τ_g , and hence K_g , are only weakly temperature dependent. Thus, the value obtained here for K_g appears to apply for depletion regions in both n- and p-type silicon at room temperature and also is a good value for use over a moderate temperature range (~240 to ~370°K, the range studied). The implication is that the present K_g value is of general usefulness in predicting neutron damage effects in depletion regions for any silicon device bombarded by fission neutrons. Below we compare calculations with experimental data to examine the validity of this concept.

It should also be noted that neutron-induced carrier removal can have an important effect in silicon p-n junctions. As stated above, the primary effect of neutrons on a reverse-biased p-n junction is to degrade τ_g and thereby increase J_g . This effect is important at moderate fluence levels ($\geq 10^{11}$ n/cm²), as shown in Figure 5-1. At relatively high fluences (e.g., $> 10^{13}$ n/cm²), carrier removal can cause the depletion region to widen, thereby causing J_g to increase due to the larger volume for carrier generation. Emphasis here is placed on changes in J_g due to τ_g degradation, but mention of carrier removal effects is made where appropriate.

The rate of change of generation current density with neutron fluence can be expressed, using Eq. (8), as

$$\frac{d(J_g - J_{g0})}{d\phi} = q n_i x_d / 2 K_g . \quad (9)$$

Assuming a temperature-independent value of K_g (7.0×10^6 n-sec/cm²), we can calculate values of this derivative. Figure 5-2 shows results of such calculations at 270, 300, and 330°K as a function of depletion region width. As an example, for a 1- μ m width, the value of the right side of Eq. (9) (from

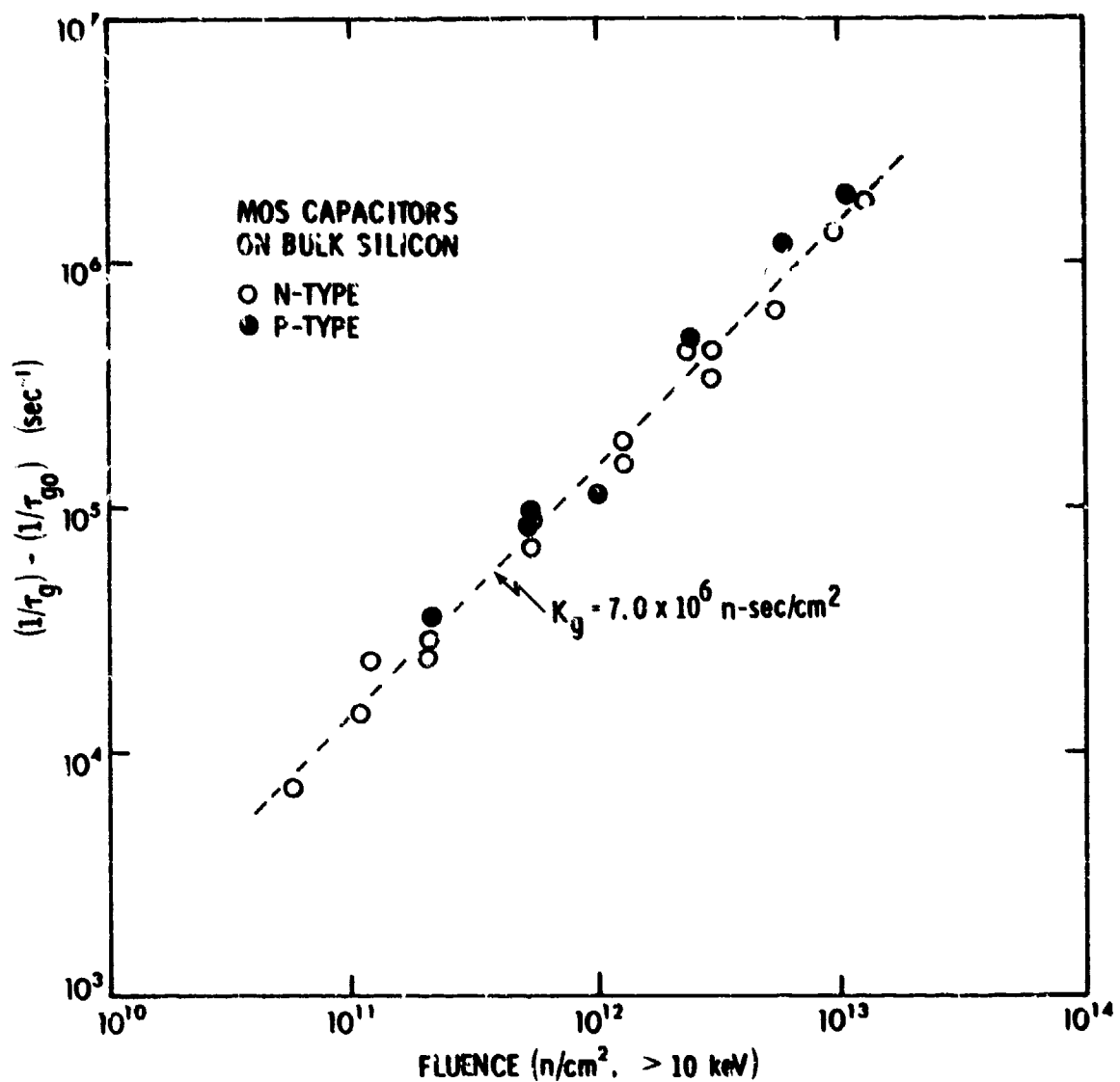


Figure 5-1. Neutron-induced change in reciprocal generation lifetime for MOS capacitors on bulk n- and p-type silicon. These data yield a generation lifetime damage coefficient K_g .

Figure 5-2) is 1.6×10^{-11} nanoamps per neutron. Thus, a fission neutron fluence of 10^{13} n/cm^2 ($> 10 \text{ keV}$) should cause an increase in generation current density of 160 nA/cm^2 .

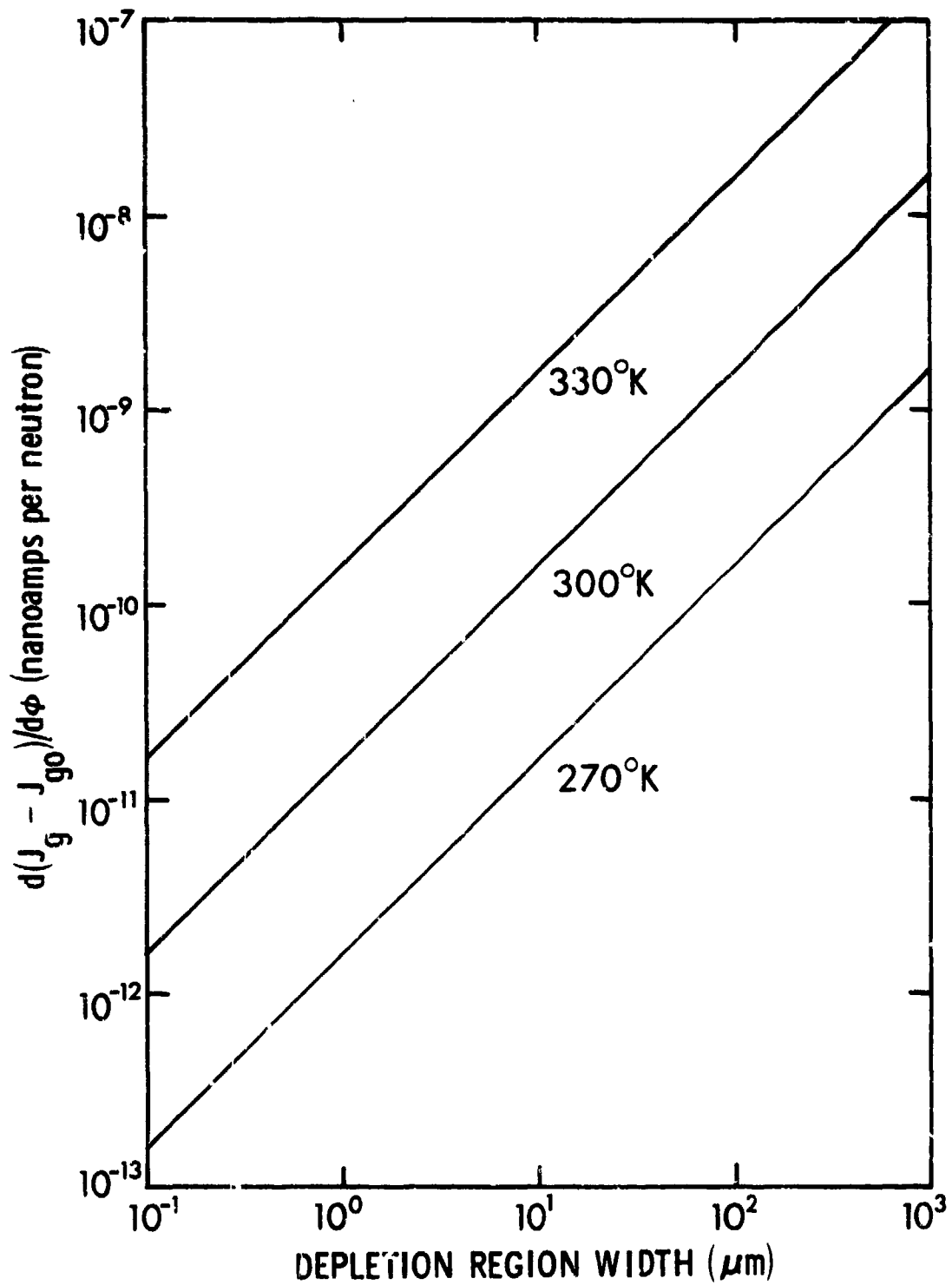


Figure 5-2. Calculated values of the neutron-induced change in generation current density as a function of depletion region width for three temperatures.

5.3 COMPARISON OF CALCULATIONS WITH EXPERIMENTAL DATA

Available experimental data are now compared with results of calculations using the analytical approach described above. The data considered here are: (1) CCD data presented in Section 4.0; (2) PIN photodiode results obtained by Kalma and Hardwick;⁶¹ (3) JFET data of Kern and McKenzie.⁶²

Figures 4-9 and 4-26 show the increase in dark current density in neutron-irradiated buried-channel CCDs. For the Hughes Aircraft device (Figure 4-9), the rate of change in dark current density with fluence is $\sim 4 \times 10^{-11}$ nA/neutron. For the Fairchild CCD311 (Figure 4-26), the value for this rate is 3.5×10^{-11} nA/neutron. Upon comparing these experimental results with the calculations shown in Figure 5-2, depletion region widths of ~ 2.2 and ~ 2.5 μm are indicated for the Fairchild and Hughes devices, respectively. However, calculated deep depletion widths for these device types are considerably larger.* To make such calculations, we use the expression for the depletion width of a step junction (n^+p) with a reverse bias V_r applied:

$$x_d = \left(\frac{2 \epsilon_s \epsilon_0 V_r}{q N_a} \right)^{1/2} \quad (10)$$

For the Hughes Aircraft CCD, the substrate dopant concentration N_a is $\sim 5 \times 10^{14} \text{ cm}^{-3}$, corresponding to $\sim 30 \Omega\text{-cm}$ material. Also, gate electrodes were clocked between 0 and 10V. We assume that all of this voltage appears across the n^+p junction and that none of it is dropped across the gate oxide. Equation (10) then yields 5.1 μm . The n-type epi layer (0.8 μm thick) is also depleted in normal operation of the CCD, so the total depletion width is $\sim 5.9 \mu\text{m}$. For the Fairchild CCD311, the range given for the substrate resistivity is 15 to 60 $\Omega\text{-cm}$. Upon using Eq. (10) with $V_r = 10\text{V}$ and also adding the thickness of the n-type epi layer (0.5 μm), we obtain a range of ~ 4.1 to $\sim 6.5 \mu\text{m}$ for the total depletion width, with the mean value being $\sim 5.3 \mu\text{m}$. Thus, the ratio of calculated x_d (Eq. (10)) to apparent x_d (Figure 5-2) is ~ 2.4 for CCDs from both suppliers. Stated another way, there is an apparent discrepancy by a factor of ~ 2.4 between CCD dark current measurements and calculations of the neutron-induced change in this quantity using Eq. (9). Possible reasons for this discrepancy are discussed below in Section 5.4.

*The present calculations of x_d are considered more accurate than the estimated range given in our earlier work (reported in Section 4.1).

Kalma and Hardwick⁶¹ measured the radiation response of various commercially available PIN photodiodes. Included in their study were measurements of neutron-induced increases in dark current for such devices. Figure 8 in their paper is a plot of dark current versus neutron fluence for diodes from seven manufacturers. Table 5-1 in the present work lists the device types studied by Kalma and gives additional information. The reverse bias at which dark current measurements were made and the measured pre-irradiation capacitance at that bias are listed for each device.⁶³ These values of bias and capacitance are those appropriate for the data shown in Figure 8 of Kalma's paper.^{61,63} It is assumed here that the measured capacitance is attributable solely to the depletion layer of width x_d in a given PIN diode. This width was then calculated using the relation $x_d = \epsilon A/C$, where ϵ is dielectric constant, A is active area, and C is capacitance. Results of such calculations are listed in Table 5-1 for each device type.

The next step was to replot Kalma's data, for convenience of analysis, in terms of the change in dark current density ($J_d - J_{d0}$) versus neutron fluence and Figures 5-3 to 5-6 present the results of this replotting. Also shown in these figures (solid and dashed lines) are results of calculations performed using Eq. (8). Table 5-2 gives the ratio of calculated to experimental values of the quantity $J_d - J_{d0}$ as a function of neutron fluence based on information in Figures 5-3 to 5-6. We now discuss findings for each device type.

Figure 5-3 compares calculation with experiment for Spectronics devices. For the SPX-3290, agreement is quite good at the two highest fluences. At 10^{12} n/cm², the calculated change in dark current density is 63% of the measured value. At 10^{11} n/cm², calculation yields a value that is 42% of the measured change in current. For the SPX-2232, agreement is good at the highest fluence. At lower fluences, calculated values are 32 to 38% of those measured. The indication is that some additional current component (i.e., other than that due to carriers thermally generated in the depletion region) contributes at lower fluences.

Figure 5-4 presents experimental data and calculations for the Hewlett-Packard PIN diode. Agreement is good at the highest fluence. (It should be noted that in Kalma's paper⁶¹ there is a plotting error at the highest fluence

Table 5-1. Active area, pre-irradiation capacitance under reverse bias, and calculated depletion-layer width for PIN photodiodes studied by Kalma and Hardwick.⁶¹

MANUFACTURER	DEVICE	ACTIVE AREA (mm ²)	REVERSE BIAS (V_r) FOR DARK CURRENT MEASUREMENTS (V)	PRE-IRRADIATION CAPACITANCE AT V_r (pF)	CALCULATED DEPLETION-LAYER WIDTH AT V_r (PRE-IRRADIATION) (μ m)
EG&G	YAG-100	5.1	200	3	179
EG&G	SHS-100	5.1	100	5	107
United Detector Technology	PIN-05D	5.1	10	15	36
United Detector Technology	PIN-020A	0.2	20	4	5.3
Hewlett-Packard	5082-4207	0.8	20	4.5	19
Spectronics	SPX-3290	0.15	25	1.9	8.3
Spectronics	SPX-2232	1.26	10	3	44

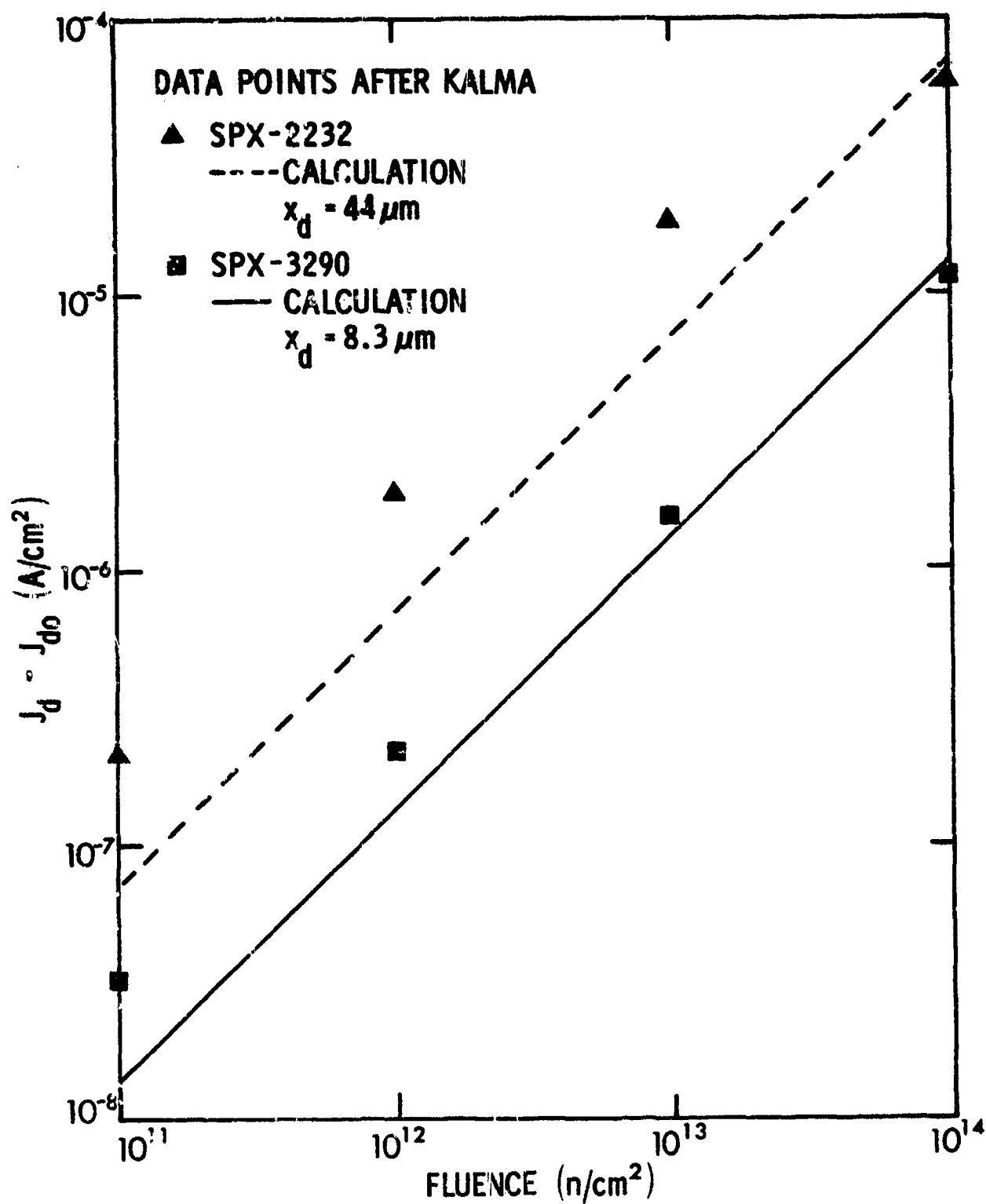


Figure 5-3. Change in dark current density versus neutron fluence for Spectronics PIN diodes. Data points were derived from the work of Kalma and Hardwick.⁶¹ Results of calculations are also shown.

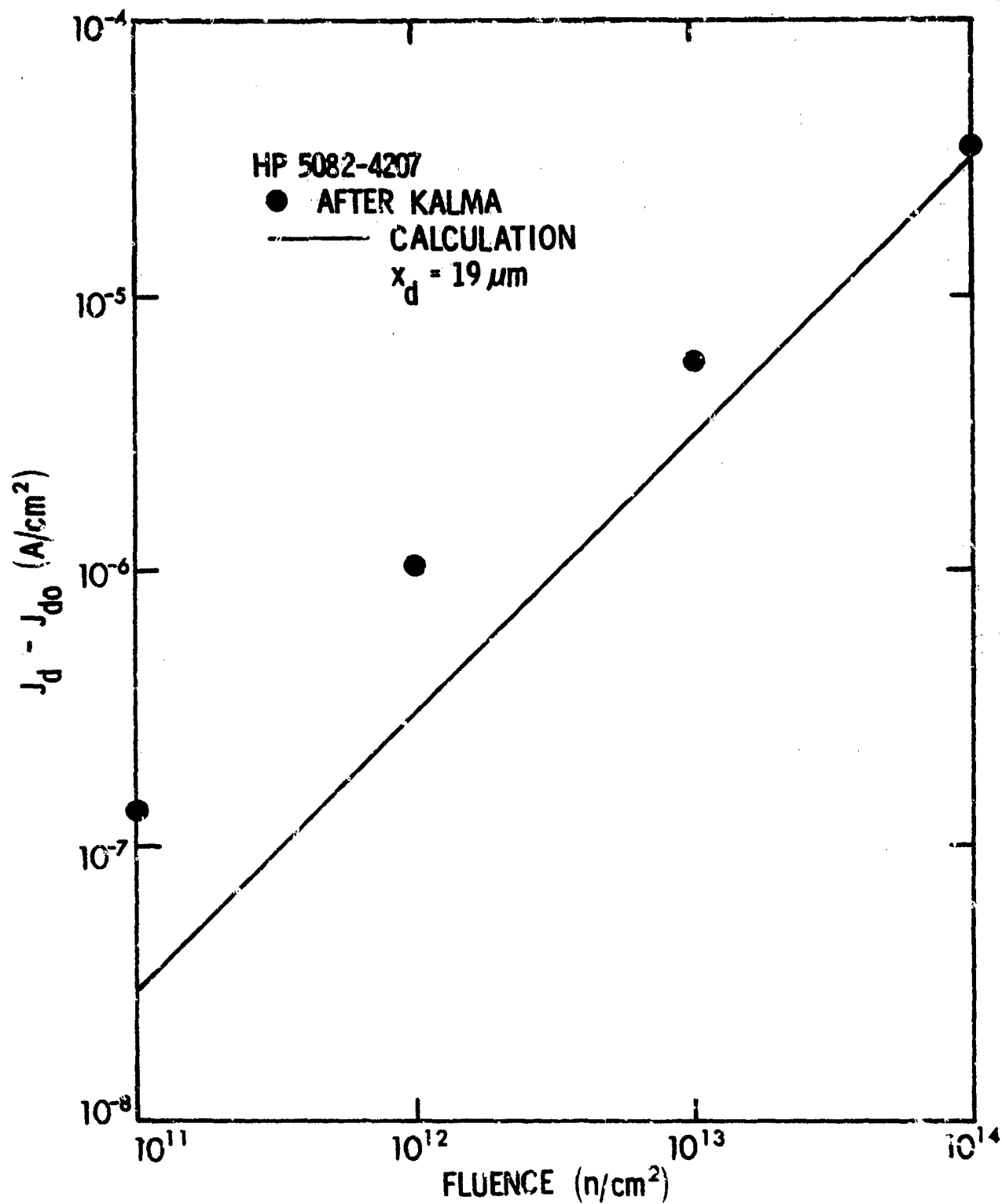


Figure 5-4. Change in dark current density versus neutron fluence for a Hewlett-Packard PIN diode. Data points were derived from the work of Kalma and Hardwick.⁶¹ Results of calculations are also shown.

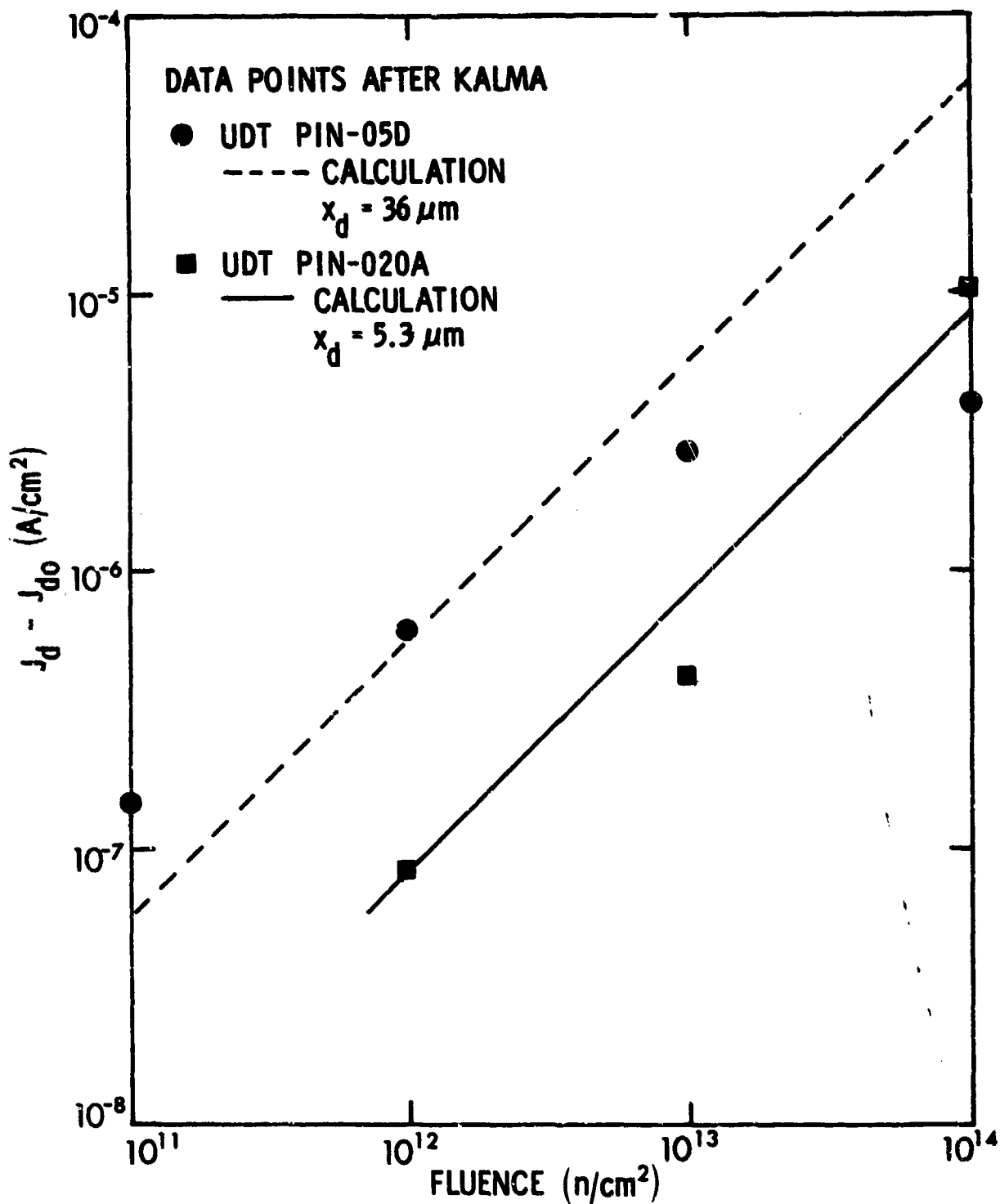


Figure 5-5. Change in dark current density versus neutron fluence for United Detector Technology PIN diodes. Data points were derived from the work of Kalma and Hardwick.⁶¹ Results of calculations are also shown.

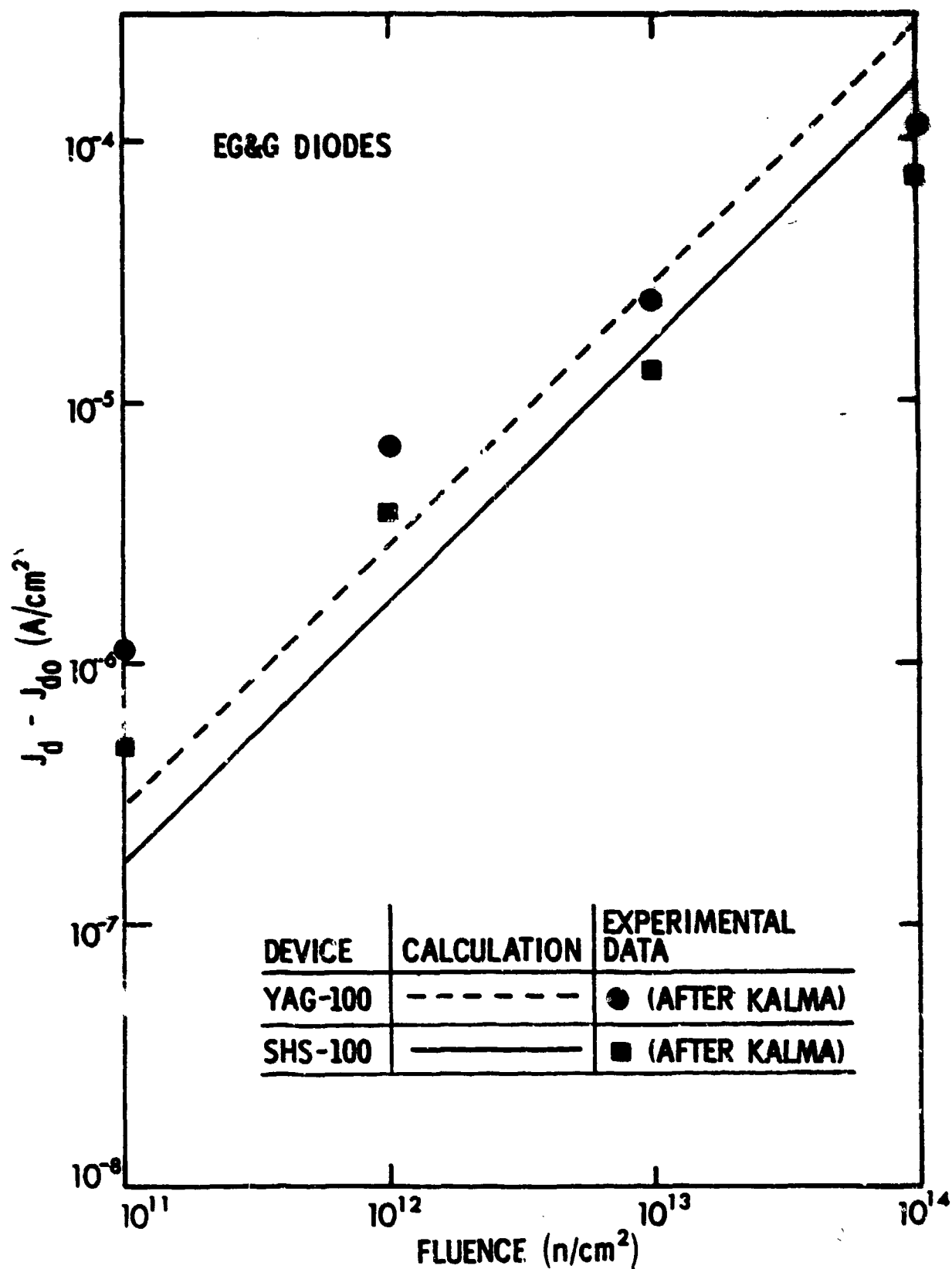


Figure 5-6. Change in dark current density versus neutron fluence for EG&G PIN diodes. Data points were derived from the work of Kalma and Hardwick.⁶¹ Results of calculations are also shown.

Table 5-2. The ratio of calculated to experimental values of the quantity $J_d - J_{d0}$ at various neutron fluences based on information in Figures 5-3 to 5-6.

DEVICE	10^{11} n/cm^2	10^{12} n/cm^2	10^{13} n/cm^2	10^{14} n/cm^2
SPX-2232	0.32	0.36	0.38	1.18
SPX-3290	0.42	0.63	0.86	1.2
5082-4207	0.23	0.30	0.54	0.86
PIN-05D	0.39	0.97	2.15	14.5
PIN-020A	—	1.00	1.98	0.78
YAG-100	0.25	0.43	1.16	2.54
SHS-100	0.35	0.45	1.28	2.32
AVERAGE (excludes PIN-05D)	0.31	0.53	1.03	1.48

in Figure 8 for the Hewlett-Packard device. The data point shown here in Figure 5-4 is the correct one.⁶³) Disagreement is noted at lower fluences, with the discrepancy decreasing as the fluences increase. Qualitatively, one can account for this discrepancy in terms of an additional current component that saturates at some moderate fluence value. An example of such a saturating current would be that attributable to gamma-ray-induced charge buildup in a surface oxide layer. This charge buildup would lead to enhanced thermal generation of carriers due to interface state production and/or depletion of the underlying silicon. Charge buildup in SiO_2 does saturate, but further study would be required to determine the mechanism responsible for the enhanced current at low fluences evident in Figure 5-4.

Comparisons between calculations and experimental data for United Detector Technology devices are shown in Figure 5-5. For the PIN-05D, the data tend toward saturation at high fluences. The calculated line (dashed) describes the data fairly well at the three lowest fluences but not at 10^{14} n/cm^2 . At that fluence, Kalma noted a significant (i.e., factor of ~ 4) drop in capacitance for this device, apparently due to carrier removal.⁶³ Since the PIN-05D was not operated in full depletion, carrier removal should result in a wider depletion region and thus

an increase in dark current. However, the measured current at 10^{14} n/cm² is substantially less than would be expected if no change in depletion width had occurred. (Note that a constant, pre-irradiation, value of x_d was used to perform calculations. This is true in all cases shown in Figures 5-3 to 5-6.) For the PIN-020A, agreement between calculation and experiment is good at 10^{12} and 10^{14} n/cm², with a factor of ~ 2 discrepancy occurring at the intermediate fluence. Kalma noted a slight (25%) decrease in measured capacitance for this device after 10^{14} n/cm², presumably due to carrier removal.⁶³ If the lower value of capacitance is used to calculate a new value of x_d , then the agreement between experiment and calculation is within 5% at 10^{14} n/cm² for the PIN-020A. In view of the scatter in the data for United Detector devices, such close agreement is probably fortuitous.

Comparison of calculations with experimental data for EG&G devices are shown in Figure 5-6. Calculated results underestimate the data at the two lowest fluences and overestimate the data at the two highest fluences. At 10^{13} n/cm², agreement between theory and experiment is within $\sim 25\%$, with the discrepancy being considerably larger at other fluences.

Kern and McKenzie⁶² measured leakage current in JFETs before and after 14.8-MeV neutron bombardment. This current was measured between source and drain while a gate bias of sufficient magnitude to deplete the active volume was applied. The primary source of leakage current in their devices should be thermal generation of carriers in the depletion region. At 300°K, the increase in leakage current after 1.1×10^{12} n/cm² was 3×10^{-12} A. The volume of the devices studied, assumed to be fully depleted, was 2.04×10^{-8} cm³. Equation (8) can be expressed in terms of generation current instead of current density:

$$I_g - I_{go} = q n_i \phi x_d A / 2 K_g \quad (11)$$

(A is area.) We equate the $x_d A$ product to the volume of the depletion region given by Kern and McKenzie. In order to calculate $I_g - I_{go}$, a value of K_g appropriate for 14.8 MeV neutrons is needed. For recombination center production in neutral bulk silicon, fusion neutrons are a factor of 2 to 3 more effective.⁶⁴ Assuming that 14.8-MeV neutrons are a factor of 2 more effective than fission neutrons in producing generation centers, K_g is then reduced to 3.5×10^6 n-sec/cm². Equation (11) then yields a value of 7.2×10^{-12} A for change in generation current, which is a factor of 2.4 larger than that measured by

Kern and McKenzie. It is interesting to note that this discrepancy factor is equal to that noted above for CCDs when experimental results were compared with calculations. Further discussion of this point is given below. One additional comment: Kern and McKenzie's data indicate that neutron bombardment produces a generation level very close to the level which dominates before irradiation. The same conclusion was reached in our work (reported in Section 4.1).

5.4 DISCUSSION AND CONCLUSIONS

We first summarize the above comparisons of calculations with experimental results. For CCDs fabricated by two sources, the calculated neutron-induced increase in dark current density was larger than the experimental value by a factor of 2.4. For the JFET data of Kern and McKenzie,⁶² our calculated increase in leakage current is larger than their experimental value by a factor of 2.4, assuming a fusion-fission damage ratio of 2. For the PIN photodiode data of Kalma and Hardwick,⁶¹ results are varied. As shown in Table 5-2, at low fluences (i.e., 10^{11} and 10^{12} n/cm²) the calculated increases in dark current underestimate the experimental values. At the two highest fluences, the calculated value is larger than the experimental value in most cases. We have listed average ratios at each fluence in Table 5-2 to provide a rough indication of the degree of agreement between experiment and calculation for the PIN diodes. (Because of the anomalously low measured dark current for the PIN-05D after 10^{14} n/cm², ratios for this device type were omitted in calculating average values.) The average discrepancy is a factor of 3 at the lowest fluence and a factor of 1.5 at the highest fluence. Overall, agreement is better at 10^{13} and 10^{14} n/cm² than at the two lowest fluences. Note that in the most successful cases (SPX-3290 and PIN-020A), agreement between theory and experiment is within a factor of ~ 2 when all fluences examined are considered. Also note that in Eq. (8), which was used to perform dark current calculations, the scaling factor on the right-hand side is x_d . Upon normalizing the change in dark current density to this quantity, the data of Kalma and Hardwick⁶¹ should become independent of device type if it is assumed that the present model fully describes their results. Figure 5-7 shows the results of such a scaling. Also shown is the calculated value of $(J_d - J_{d0})/x_d$ versus fluence. The discrepancies evident between calculation and experiment in Figure 5-7 were discussed above in connection with results shown in Figures 5-3 through 5-6 and in Table 5-2.

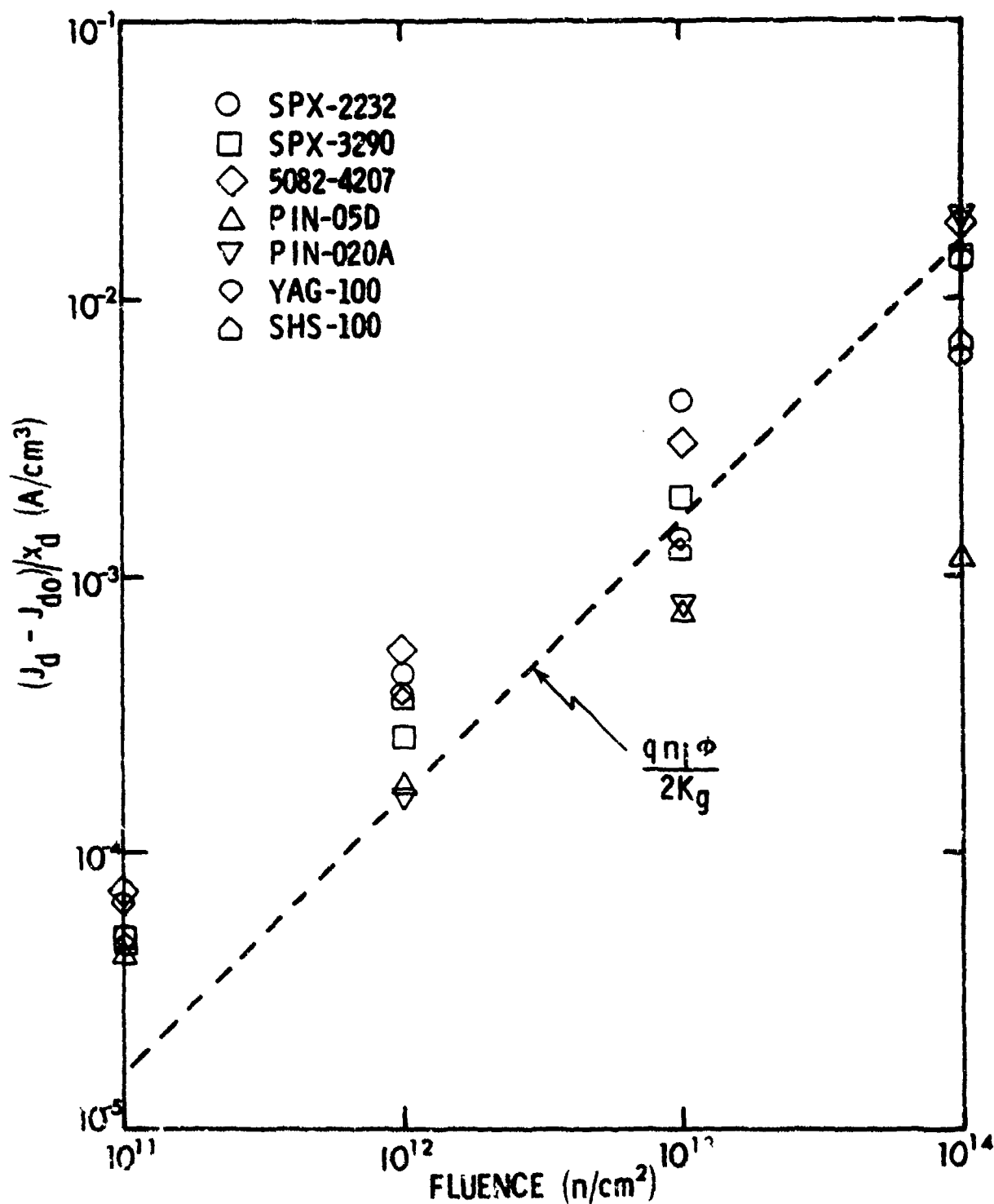


Figure 5-7. The quantity $(J_d - J_{d0})/x_d$ versus neutron fluence for various PIN diodes. Data were derived from the work of Kalma and Hardwick⁶¹ as described in the text. Values of x_d employed are given in Table 5-1.

(The approach used to obtain the calculated fit in Figure 5-7 should be of general applicability for devices in which measured dark current is dominated by generation current (i.e., originates in the depleted region). We can express the change in dark current, ΔI_d , per unit volume V and per unit neutron fluence as (using Eq. (11))

$$\frac{\Delta I_d}{V\phi} = \frac{q n_i}{2 K_g} \quad (12)$$

At 300°K, we obtain a value for $\Delta I_d/V\phi$ of 1.6×10^{-16} amps/neutron-cm for fission neutrons. Multiplying this value by the depletion-region volume and by the neutron fluence will give the predicted change in dark current for a given device.)

In the process of attempting to determine possible explanations for the discrepancies noted above for various types of silicon devices, we noted differences in analytical relationships for generation rate and generation lifetime in the literature. Grove⁵¹ gives the expression for G stated above (Eq. (2)), and then equates this expression to $n_i/2\tau_g$ (Eq. (4)), which leads to the τ_g relation given in Eq. (3). That is, Grove states that $G \equiv n_i/2\tau_g$ in general for a single generation level. (Note that he does not assume this level to be at midgap.) On the other hand, Sze,⁶⁵ who also employs the same G expression as Grove (Eq. (2) above), states that $G \equiv n_i/\tau_g$ in general. He then obtains an expression for τ_g which differs by a factor of 2 from that given by Grove (Eq. (3) above). It is not our intent to resolve this conflict here, but it does have an impact on the τ_g and K_g values obtained in the present work. In Eq. (1) of Section 4.1, a differential equation is given which is based on the modification of Zerbst analysis⁴² performed by Schroder and Nathanson.³⁸ That equation actually differs slightly from the one developed by Schroder and Nathanson because they assume $G = n_i/\tau_g$ whereas Eq. (1) in Section 4.1 was developed⁴¹ assuming $G = n_i/2\tau_g$. Thus, we have been consistent in our analytical approach here in that the same G expression was used in the Zerbst analysis used to obtain τ_g (and hence K_g) as in the analysis used to obtain an expression for J_g (Eq. (5) above). If instead we had assumed $G = n_i/\tau_g$, then all τ_g values and also the value for K_g would be a factor of 2 larger. That is, K_g would equal 1.4×10^7 n-sec/cm². Thus, care must be employed when using $K_g = 7 \times 10^6$ n-sec/cm²; one must assume $G = n_i/2\tau_g$ when doing so. It is important to

note that calculations performed using Eqs. (8) and (9) (e.g., the calculations shown in Figure 5-2) are independent of the G expression assumed as long as the same expression is used consistently (i.e., in Zerst analysis and in subsequent calculations). We therefore conclude that the generation rate expression assumed here does not account for the discrepancies noted above between calculations and experimental data for various devices.

Grimmeiss^{66,67} has performed experimental work and analysis which indicates that for levels deep in the forbidden gap the effective width for carrier generation in a reverse-biased p-n junction is less than the full depletion width. (This topic has also been addressed by Calzolari and Graffi.⁶⁸) If such a situation applies for the experimental cases considered above, then a portion of the discrepancy between calculation and experiment can be accounted for. In the case of CCDs, the maximum reverse voltage appearing across the junction between the n-type epi layer and the p-type substrate is 10V. Braun and Grimmeiss⁶⁷ calculate for a linearly graded p⁺n junction (not the actual case here, but close enough for the present purposes) with 10V applied that the percentage of the depletion region width effective for carrier generation is 80%. This factor reduces the discrepancy between experiment and calculation for CCDs to a factor of ~ 1.9 . (If we further assume that some portion, say 15%, of the applied gate voltage is dropped across the oxide, the discrepancy factor is reduced to ~ 1.7 .)

For the JFET experiments of Kern and McKenzie,⁶² a DC reverse bias of 5V was applied to the gate p-n junction to deplete the device. Once again using the linearly graded p⁺n junction calculations of Braun and Grimmeiss,⁶⁷ we obtain an effective carrier generation width of 75% of the full depletion region width. Applying this correction reduces the discrepancy factor between theory and experiment to ~ 1.3 .

For the PIN diode data of Kalma and Hardwick,⁶¹ it is not presently clear how to make an appropriate correction for the effective generation volume. (However, see Footnote 10 in Ref. 69.) As seen in Table 5-2, at the two lowest fluences such a correction would serve to increase the discrepancy between calculation and experiment. It appears that an additional current component, i.e., other than generation current, is important at such fluences. At the two highest fluences, a generation volume correction would decrease the

observed discrepancy in most cases. One further note: Leakage current measurements on PIN diodes were performed at room temperature, which may have varied a few degrees.⁶³ This could account for some of the discrepancy between calculations and experimental data since J_g depends strongly on temperature through n_i . We also note that the active areas listed in Table 5-1, which were used in all calculations, were not measured but were obtained from manufacturers' data sheets. Actual areas could differ somewhat from these typical values for specific devices and therefore increase the discrepancy between calculated and experimental results for PIN diodes.

To conclude, we have found that leakage current data obtained for various neutron-irradiated silicon devices, including CCDs, PIN diodes, and JFETs, can be described reasonably well using a model which incorporates K_g , the generation lifetime damage coefficient determined using MOS capacitors. Agreement between calculations and experimental results is within a factor of ≤ 2 for most cases, with the exception of PIN diode data at low fluences (10^{11} n/cm²). Such agreement suggests that the present calculational approach is suitable for making reasonably accurate estimates of neutron-induced increases in dark current for silicon devices. From a basic mechanisms viewpoint, further work will be required to resolve the remaining discrepancy between calculated and experimental results.

SECTION 6.0

REFERENCES

1. O.L. Curtis, Jr., J.R. Srouer, and K.Y. Chiu, J. Appl. Phys. 45, 4506 (1974).
2. J.R. Srouer, O.L. Curtis, Jr., and K.Y. Chiu, IEEE Trans. Nucl. Sci. 21, 73 (Dec. 1974).
3. J.R. Srouer, S. Othmer, O.L. Curtis, Jr., and K.Y. Chiu, IEEE Trans. Nucl. Sci. 23, 1513 (1976).
4. J.R. Srouer and K.Y. Chiu, IEEE Trans. Nucl. Sci. 24, 2140 (1977).
5. H.E. Boesch, Jr., and J.M. McGarrity, IEEE Trans. Nucl. Sci. 23, 1520 (1976).
6. R.C. Hughes, Phys. Rev. Lett. 30, 1333 (1973); Phys. Rev. Lett. 35, 449 (1975).
7. O.L. Curtis, Jr., and J.R. Srouer, J. Appl. Phys. 48, 3819 (1977).
8. H.E. Boesch, Jr., F.B. McLean, J.M. McGarrity, and G.A. Ausman, Jr., IEEE Trans. Nucl. Sci. 22, 2163 (1975).
9. F.B. McLean, H.E. Boesch, Jr., and J.M. McGarrity, IEEE Trans. Nucl. Sci. 23, 1506 (1976).
10. F.B. McLean, G.A. Ausman, Jr., H.E. Boesch, Jr., and J.M. McGarrity, J. Appl. Phys. 47, 1529 (1976).
11. F.W. Schmidlin, Phys. Rev. B16, 2362 (1977).
12. R.C. Hughes, Phys. Rev. B15, 2012 (1977).
13. R.N. Nucho and A. Madhukar, in The Physics of SiO₂ and Its Interfaces, S.T. Pantelides, Editor (Pergamon, New York, 1978), p. 60.
14. D.J. Chadi, R.B. Laughlin, and J.D. Joannopoulos, in The Physics of SiO₂ and Its Interfaces, S.T. Pantelides, Editor (Pergamon, New York, 1978), p. 55.
15. A. Hartstein, Z.A. Weinberg, and D.J. DiMaria, in The Physics of SiO₂ and Its Interfaces, S.T. Pantelides, Editor (Pergamon, New York, 1978), p. 51.
16. E. Schibli and A.G. Milnes, Solid-State Electronics 11, 323 (1968).
17. M. Kuhn, Solid-State Electronics 13, 873 (1970).
18. M. Lax, Phys. Rev. 119, 1502 (1960).
19. T.H. Ning, J. Appl. Phys. 49, 5997 (1978).

20. J.S. Blakemore, Semiconductor Statistics (Pergamon Press, New York, 1962), p. 139.
21. K.M. van Vliet, Proc. IRE 46, 1004 (1958).
22. R.D. Nelson, Optical Engineering 16, 275 (1977).
23. P. LoVecchio, P. Raimondi, and R. Longshore, Proc. IRIS Detector Specialty Group, March 1976.
24. P. Norton, Phys. Rev. Lett. 30, 488 (1973).
25. A.H. Kalma and C.J. Fischer, IEEE Trans. Nucl. Sci. 24, 2158 (1977).
26. S. Othmer, O.L. Curtis, Jr., and D.N. Pocock, Proceedings of IRIS Detector Specialty Group, March 1976.
27. V.E. Butuzov and B.V. Kornilov, Soviet Physics - Semiconductors 3, 769 (1969).
28. W.R. Thurber, A.W. Stallings, and J. Krawczyk, NBS Technical Note 743, 1972, p. 14.
29. W.M. Bullis, Solid State Electronics 9, 143 (1966).
30. W.G. Oldham, IEEE Trans. Nucl. Sci. 19, 347 (Dec. 1972).
31. R.F. Bass, IEEE Trans. Nucl. Sci. 14, 78 (Dec. 1967).
32. R.A. Williams and R.D. Nelson, IEEE Trans. Nucl. Sci. 22, 2639 (1975).
33. G.A. Hartsell, in "Proceedings of the 1975 International Conference on Applications of CCDs," San Diego, CA, October 1975.
34. N.S. Saks, J.M. Killiany, and W.D. Baker, in "Proceedings of NASA-JPL Conference on CCD Technology and Applications," Washington, D.C., December 1976.
35. C.P. Chang and K.G. Aubuchon, Final Report on Contract N000173-76-C-0166, March 1977.
36. N.S. Saks, IEEE Trans. Nucl. Sci. 24, 2153 (1977).
37. C.P. Chang, IEEE Trans. Nucl. Sci. 24, 2190 (1977).
38. D.K. Schroder and H.C. Nathanson, Solid-State Electronics 13, 577 (1970).
39. R.F. Pierret and D.W. Small, IEEE Trans. Electron Devices 20, 457 (1973).
40. D.W. Small and R.F. Pierret, Solid-State Electronics 19, 505 (1976).
41. T. Takino, Ph.D. thesis, UCLA 1976.
42. M. Zerbst, Z. Angew, Phys. 22, 30 (1966):

43. D.K. Schroder and J. Guldberg, Solid-State Electronics 14, 1285 (1971).
44. J.G. Simmons and L.S. Wei, Solid-State Electronics 19, 153 (1976).
45. A. Many, Y. Goldstein, and N.B. Grover, Semiconductor Surfaces (North-Holland, Amsterdam, 1965), pp. 194-208.
46. O.L. Curtis, Jr., IEEE Trans. Nucl. Sci. 13, 33 (Dec. 1966).
47. F.P. Heiman, IEEE Trans. Electron Devices 14, 781 (1967).
48. O.L. Curtis, Jr., J. Appl. Phys. 39, 3109 (1968).
49. B.L. Gregory, IEEE Trans. Nucl. Sci. 16, 53 (Dec. 1969).
50. O.L. Curtis, Jr., and J.R. Srour, IEEE Trans. Nucl. Sci. 20, 196 (Dec. 1973).
51. A.S. Grove, Physics and Technology of Semiconductor Devices (Wiley, New York, 1967).
52. B.L. Gregory and H.H. Sander, Proc. IEEE 58, 1328 (1970).
53. C.H. Sequin and M.F. Tompsett, Charge Transfer Devices (Academic Press, New York, 1975), p. 134.
54. C.P. Chang and K.G. Aubuchon, Final Report on Contract N00173-77-C-0158, June 1978.
55. J.R. Srour, S. Othmer, S.C. Chen, and R.A. Hartmann, Report No. HDL-CR-78-134-1, Final Report on Contract DAAG-39-77-C-0134, October 1978.
56. P.S. Winokur, J.M. McGarrity, and H.E. Boesch, Jr., IEEE Trans. Nucl. Sci. 23, 1580 (1976).
57. J.R. Adams, W.R. Dawes, and T.J. Sanders, IEEE Trans. Nucl. Sci. 24, 2099 (1977).
58. J.R. Srour and O.L. Curtis, Jr., IEEE Trans. Nucl. Sci. 19, 362 (Dec. 1972).
59. J.R. Srour and O.L. Curtis, Jr., J. Appl. Phys. 40, 4082 (1969).
60. B.L. Gregory and H.H. Sander, Proc. IEEE 58, 1328 (1970).
61. A.H. Kalma and W.H. Hardwick, IEEE Trans. Nucl. Sci. 25, 1483 (1978).
62. H.E. Kern and J.M. McKenzie, IEEE Trans. Nucl. Sci. 17, 256 (Dec. 1970).
63. A.H. Kalma, personal communication.
64. J.R. Srour, IEEE Trans. Nucl. Sci. 20, 190 (Dec. 1973).

65. S.M. Sze, Physics of Semiconductor Devices (Wiley, New York, 1969), p. 103.
66. H.G. Grimmeiss, in Annual Review of Materials Science, Vol. 7 (Annual Reviews Inc., Palo Alto, 1977), p. 341.
67. S. Braun and H.G. Grimmeiss, J. Appl. Phys. 44, 2789 (1973).
68. P.U. Calzolari and S. Graffi, Solid-State Electronics 15, 1003 (1972).
69. S. Braun and H.G. Grimmeiss, Solid State Communications 11, 1457 (1972).

DISTRIBUTION LIST

DEPARTMENT OF DEFENSE

Assistant to the Secretary of Defense
Atomic Energy
ATTN: Executive Assistant

Command & Control Technical Center
ATTN: C-362, G. Adkins

Defense Documentation Center
12 cy ATTN: DD

Defense Electronic Supply Center
ATTN: DESC-ECS, D. Drooge
ATTN: DESC-ECT, J. Niles
ATTN: DESC-EQE, R. Grillmeier
ATTN: DESC-EQE, J. Coupsil
ATTN: DESC-ELP, R. Munko
ATTN: DESC-ECS, D. Hill
ATTN: DESC-ECS, J. Dennis

Defense Logistics Agency
ATTN: DLA-QEL, J. Slattery
ATTN: DLA-SE

Defense Material Specifications & Standard Office
ATTN: L. Fox

Defense Nuclear Agency
ATTN: RAEV, A. Kubo
ATTN: DDST
ATTN: RAEV, M. Kemp
4 cy ATTN: TITL

Field Command
Defense Nuclear Agency
ATTN: FCPR

Field Command
Defense Nuclear Agency
Livermore Division
ATTN: FCPRL

National Security Agency
ATTN: G. Daily
ATTN: T. Brown
ATTN: P. Deboy

NATO School (SKAPE)
ATTN: U.S. Documents Officer

Undersecretary of Defense for Rsch. & Engrg.
ATTN: Strategic & Space Systems (OS)

DEPARTMENT OF THE ARMY

Aberdeen Proving Ground
Department of the Army
ATTN: S. Harrison

BMD Advanced Technology Center
Department of the Army
ATTN: ATC-T

BMD Systems Command
Department of the Army
ATTN: BMDSC-4W, R. Dekalb

DEPARTMENT OF THE ARMY (Continued)

Deputy Chief of Staff for Rsch. Dev. & Acq.
Department of the Army
ATTN: Advisor for RDA Analysis, M. Gale

Harry Diamond Laboratories
Department of the Army
ATTN: DELHD-N-P, F. Balicki
ATTN: DELHD-N-RSH, H. Eisen
ATTN: DELHD-N-RBH, J. Halpin
ATTN: DELHD-N-RPH
ATTN: DELHD-N-RBC, J. McGarrity
ATTN: DELHD-N-P

U.S. Army Armament Research & Development Command
ATTN: DRD/R-LCA-PD

U.S. Army Communications R & D Command
ATTN: D. Huehe

U.S. Army Missile R & D Command
3 cy ATTN: KSIC

U.S. Army Nuclear & Chemical Agency
ATTN: Library

White Sands Missile Range
Department of the Army
ATTN: STEWS-TE-AN, T. Leura
ATTN: STEWS-TE-AN, M. Squires

DEPARTMENT OF THE NAVY

Naval Air Systems Command
ATTN: AIR 350F

Naval Electronic Systems Command
ATTN: Code 5045.11, C. Suman

Naval Ocean Systems Center
ATTN: Code 4471

Naval Postgraduate School
ATTN: Code 0142, Library
ATTN: Code 1424, Library

Naval Research Laboratory
ATTN: Code 6701, J. Brown
ATTN: Code 5216, H. Hughes
ATTN: Code 6627, C. Guenger
ATTN: Code 6601, E. Jolicki
ATTN: Code 6650, A. Namenson
ATTN: Code 6600, J. McFillinney
ATTN: Code 5210, J. Davey

Naval Sea Systems Command
ATTN: SEA-06J, R. Lane

Naval Ship Engineering Center
ATTN: Code 617402

Naval Surface Weapons Center
ATTN: Code F31
ATTN: Code F30

DEPARTMENT OF THE NAVY (Continued)

Naval Weapons Center
ATTN: Code 233

Naval Weapons Evaluation Facility
ATTN: Code AT-6

Naval Weapons Support Center
ATTN: Code 70242, J. Munarin
ATTN: Code 7024, J. Ramsey
ATTN: Code 7024, T. Ellis

Office of Naval Research
ATTN: Code 220, D. Lewis
ATTN: Code 427, L. Cooper

Office of the Chief of Naval Operations
ATTN: OP 985F

Strategic Systems Project Office
Department of the Navy
ATTN: NSP-2701, J. Pitsenberger
ATTN: NSP-2015
ATTN: NSP-230, D. Gold
ATTN: NSP-27331, P. Spnctor

DEPARTMENT OF THE AIR FORCE

Air Force Aero-Propulsion Laboratory
ATTN: POD, P. Stover

Air Force Avionics Laboratory
ATTN: TEA, R. Conklin
ATTN: DHE, H. Hennecke

Air Force Geophysics Laboratory
ATTN: SULL
ATTN: SULL S-29

Air Force Institute of Technology
ATTN: ENP, C. Bridgeman

Air Force Materials Laboratory
ATTN: LTE
ATTN: LPO, R. Hickmott

Air Force Systems Command
ATTN: XRLA, R. Stead
ATTN: DLCAM, T. Seale
ATTN: DLW
ATTN: DLCA

Air Force Technical Applications Center
ATTN: TAE

Air Force Weapons Laboratory, AFSC
ATTN: ELT, J. Ferry
ATTN: ELP, M. Knoll
ATTN: ELP, J. Mullis
ATTN: ELP, R. Maier
ATTN: ELP, G. Chapman
3 cy ATTN: SUL

Foreign Technology Division
Air Force Systems Command
ATTN: TQTD, B. Ballard
ATTN: PDJV

DEPARTMENT OF THE AIR FORCE (Continued)

Air Logistics Command
Department of the Air Force
ATTN: MMETH, F. Walter
ATTN: MMETH, R. Padfield
ATTN: MMIFM, D. Stanger
ATTN: MMGRW, G. Fry
ATTN: MMEDD, C. Graham
ATTN: OO-ALC/MM, R. Blackburn
ATTN: MMIFM, S. Mallory

Rome Air Development Center
Air Force Systems Command
ATTN: RBRP, C. Lane
ATTN: RBRM, J. Brauer

Rome Air Development Center
Air Force Systems Command
ATTN: ESR, W. Shedd
ATTN: ESER, R. Buchanan
ATTN: ESR, P. Vail
ATTN: ETS, R. Dolan
ATTN: ESE, A. Kahan

Space & Missile Systems Organization
Air Force Systems Command
ATTN: AQT, W. Blakney
ATTN: AQM
ATTN: DYS, L. Darda
ATTN: SZJ, R. Davis
ATTN: C. Kelly

Space & Missile Systems Organization
Air Force Systems Command
ATTN: MNNG
ATTN: MNNL, S. Kennedy
ATTN: MNNH, J. Tucker

Strategic Air Command
Department of the Air Force
ATTN: XPFS, M. Carra

DEPARTMENT OF ENERGY

Department of Energy
Albuquerque Operations Office
ATTN: Document Control for WSSB

DEPARTMENT OF ENERGY CONTRACTORS

Lawrence Livermore Laboratory
ATTN: Document Control for Technical Info.

Los Alamos Scientific Laboratory
ATTN: Document Control for J. Freed

Sandia Laboratories
ATTN: Document Control for F. Coppage
ATTN: Document Control for W. Dawes
ATTN: Document Control for J. Hood
ATTN: Document Control for J. Barnum
ATTN: Document Control for R. Gregory

OTHER GOVERNMENT AGENCIES

Central Intelligence Agency
ATTN: OSI/RD

OTHER GOVERNMENT AGENCIES (Continued)

Department of Commerce
National Bureau of Standards
ATTN: Security Officer for R. Scace
ATTN: Security Officer for W. Bullis
ATTN: Security Officer for J. Humphreys
ATTN: Security Officer for J. Mayo-Wells
ATTN: Security Officer for J. French
ATTN: Security Officer for K. Galloway
ATTN: Security Officer for S. Chappell

NASA
Goddard Space Flight Center
ATTN: V. Danchenko
ATTN: J. Adolphsen

NASA
George C. Marshall Space Flight Center
ATTN: M. Nowakowski
ATTN: L. Haniter
ATTN: EGO2
ATTN: H. Yearwood

NASA
ATTN: J. Murphy

NASA
Lewis Research Center
ATTN: M. Baddour

NASA
Ames Research Center
ATTN: G. DeYoung

DEPARTMENT OF DEFENSE CONTRACTORS

Advanced Microdevices, Inc.
ATTN: J. Schlageter

Advanced Research & Applications Corporation
ATTN: R. Armistead

Aerojet Electro-Systems Com.
ATTN: T. Hanscome

Aerospace Corporation
ATTN: D. Fresh
ATTN: S. Bower
ATTN: W. Willis

Aerospace Industries Assoc. of America, Inc.
ATTN: S. Siegel

Battelle Memorial Institute
ATTN: R. Thatcher

BDM Corporation
ATTN: D. Wunch
ATTN: R. Pease
ATTN: D. Alexander

Bendix Corporation
Navigation and Control Group
ATTN: E. Meeder

Boeing Company
ATTN: I. Arimura
ATTN: A. Johnston
ATTN: C. Rosenberg
ATTN: W. Rumpza

DEPARTMENT OF DEFENSE CONTRACTORS (Continued)

Boeing Company
ATTN: D. Egelkrout

Burr-Brown Research Corporation
ATTN: H. Smith

California Institute of Technology
Jet Propulsion Laboratory
ATTN: A. Shumka
ATTN: W. Price
ATTN: A. Stanley

Charles Stark Draper Laboratory, Inc.
ATTN: R. Ledger
ATTN: P. Greiff
ATTN: R. Bedingfield
ATTN: A. Schutz
ATTN: C. Lai

Cincinnati Electronics Corporation
ATTN: C. Stump
ATTN: L. Hammond

Control Data Corporation
ATTN: J. Meehan

University of Denver
Colorado Seminary
Denver Research Institute
ATTN: Security Officer for F. Venditti

E-Systems, Inc.
Garland Division
ATTN: K. Reis

Electronic Industries Association
ATTN: J. Hessman

EMM Corporation
ATTN: F. Krch

Exp. & Math. Physics Consultants
ATTN: T. Jordan

Fairchild Camera and Instrument Corporation
ATTN: R. Marshall
ATTN: Security Control for D. Myers

Ford Aerospace & Communications Corporation
ATTN: Technical Information Services
ATTN: J. Davison

Ford Aerospace & Communications Corporation
ATTN: D. Cadle

Franklin Institute
ATTN: R. Thompson

Garrett Corporation
ATTN: R. Weir

General Dynamics Corporation
Convair Division
ATTN: W. Hansen
ATTN: N. Cohn

General Dynamics Corporation
Fort Worth Division
ATTN: K. Fields
ATTN: O. Wood

DEPARTMENT OF DEFENSE CONTRACTORS (Continued)

General Electric Company
Space Division

ATTN: R. Casey
ATTN: L. Sivo
ATTN: D. Long
ATTN: J. Peden

General Electric Company
Re-Entry & Environmental Systems Division

ATTN: W. Patterson
ATTN: R. Benedict
ATTN: J. Palchefskey, Jr.
ATTN: Technical Library

General Electric Company
Ordnance Systems

ATTN: J. Reid

General Electric Company
Aircraft Engine Business Group

ATTN: R. Hellen

General Electric Company
Aerospace Electronics Systems

ATTN: W. Patterson
ATTN: D. Cole
ATTN: J. Gibson

General Electric Company

ATTN: D. Pepin

General Electric Company-TEMPO

ATTN: M. Espig
ATTN: DASIAC

General Electric Company-TEMPO

ATTN: DASIAC

General Research Corporation

Santa Barbara Division

ATTN: Technical Information Office
ATTN: R. Hill

George C. Messenger

Consulting Engineer

ATTN: G. Messenger

Georgia Institute of Technology

Georgia Tech. Research Institute

ATTN: R. Curry

Georgia Institute of Technology

Office of Contract Administration

ATTN: Res. & Sec. Coord. for H. Denny

Goodyear Aerospace Corporation

Arizona Division

ATTN: Security Control Station

Grumman Aerospace Corporation

ATTN: J. Rogers

GTE Sylvania, Inc.

Electronics Systems Group-Eastern Division

ATTN: C. Thornhill
ATTN: L. Blaisdell
ATTN: L. Pauples

DEPARTMENT OF DEFENSE CONTRACTORS (Continued)

GTE Sylvania, Inc.

ATTN: H & V Group
ATTN: H. Ullman
ATTN: P. Fredrickson
ATTN: J. Waldron

Harris Corporation

Harris Semiconductor Division

ATTN: J. Cornell
ATTN: C. Anderson

Honeywell, Inc.

Avionics Division

ATTN: R. Gumm

Honeywell, Inc.

Avionics Division

ATTN: C. Cerulli

Honeywell, Inc.

Radiation Center

ATTN: Technical Library

Honeywell, Inc.

Defense Systems Division

ATTN: K. Gaspard

Hughes Aircraft Company

ATTN: R. McGowan
ATTN: J. Singletary

Hughes Aircraft Company

ATTN: E. Smith
ATTN: W. Scott

IBM Corporation

ATTN: T. Martin
ATTN: F. Fietse
ATTN: H. Mathers

IIT Research Institute

ATTN: I. Mindel

Institute for Defense Analyses

ATTN: Technical Information Services

Intel Corporation

ATTN: M. Jordan

International Business Machine Corporation

Thomas Watson Research Center

ATTN: J. Ziegler

International Telephone & Telegraph Corporation

ATTN: Department 608
ATTN: A. Richardson

Intersil, Inc.

ATTN: D. MacDonald

IRT Corporation

ATTN: J. Harrity

JAYCOR

ATTN: T. Flanagan
ATTN: R. Stahl
ATTN: L. Scott

DEPARTMENT OF DEFENSE CONTRACTORS (Continued)

Johns Hopkins University
Applied Physics Laboratory
ATTN: P. Partridge

Kaman Sciences Corporation
ATTN: J. Lubell

Litton Systems, Inc.
Guidance & Control Systems Division
ATTN: G. Maddox

Lockheed Missiles & Space Company, Inc.
ATTN: C. Thompson
ATTN: H. Phillips
ATTN: E. Smith
ATTN: P. Bene
ATTN: M. Smith

Lockheed Missiles & Space Company, Inc.
ATTN: J. Smith
ATTN: J. Crowley

M.I.T. Lincoln Laboratory
ATTN: P. McKenzie

Martin Marietta Corporation
ATTN: W. Brockett
ATTN: H. Cates
ATTN: W. Janocko
ATTN: R. Gaynor

Martin Marietta Corporation
ATTN: E. Carter

Magnavox Govt. & Indus. Electronics Company
ATTN: W. Richeson

McDonnell Douglas Corporation
ATTN: Technical Library

McDonnell Douglas Corporation
ATTN: M. Stitch
ATTN: D. Dohm
ATTN: Library

McDonnell Douglas Corporation
ATTN: J. Holmgren
ATTN: D. Fitzgerald

Mission Research Corporation
ATTN: C. Longmire

Mission Research Corporation-San Diego
ATTN: J. Azarewicz
ATTN: V. Van Lint
ATTN: J. Raymond
ATTN: R. Berger

Mitre Corporation
ATTN: M. Fitzgerald

Motorola, Inc.
Government Electronics Division
ATTN: A. Christensen

Motorola, Inc.
Semiconductor Group
ATTN: L. Clark

DEPARTMENT OF DEFENSE CONTRACTORS (Continued)

National Academy of Sciences
National Materials Advisory Board
ATTN: R. Shane

National Semiconductor Corporation
ATTN: R. Wang
ATTN: A. London

University of New Mexico
Electrical Engineering & Computer Science Dept.
ATTN: H. Southward

Northrop Corporation
Northrop Research & Technology Center
ATTN: T. Jackson
ATTN: P. Eisenberg
ATTN: A. Kalma
ATTN: R. Hartmann
ATTN: S. Chen
2 cy ATTN: S. Othmer
2 cy ATTN: Library
15 cy ATTN: J. Srour

Northrop Corporation
Electronic Division
ATTN: D. Strobel
ATTN: L. Apodaca
ATTN: P. Gardner

Physics International Company
ATTN: J. Shea
ATTN: Division 6000
ATTN: J. Huntington

R & D Associates
ATTN: C. MacDonald
ATTN: R. Poll
ATTN: S. Rogers

Rand Corporation
ATTN: C. Crain

Raytheon Company
ATTN: J. Ciccio

Raytheon Company
ATTN: A. Van Doren
ATTN: H. Flescher

RCA Corporation
Government Systems Division
Astro Electronics
ATTN: V. Mancino
ATTN: G. Brucker

RCA Corporation
David Sarnoff Research Center
ATTN: D. O'Connor
ATTN: Office N103

RCA Corporation
Government Systems Division
Missile & Surface Radar
ATTN: R. Killion

RCA Corporation
Camden Complex
ATTN: J. Saultz
ATTN: E. Van Keuren

DEPARTMENT OF DEFENSE CONTRACTORS (Continued)

RCA Corporation
Somerville Plant, Solid State Division
ATTN: W. Allen

Rensselaer Polytechnic Institute
ATTN: R. Gutmann

Research Triangle Institute
ATTN: Security Office for M. Simons, Jr.

Rockwell International Corporation
ATTN: V. Strahan
ATTN: J. Bell
ATTN: T. Oki
ATTN: G. Messenger
ATTN: V. De Martino

Rockwell International Corporation
Space Division
ATTN: D. Stevens

Rockwell International Corporation
ATTN: T. Yates
ATTN: TIC BA08

Sanders Associates, Inc.
ATTN: L. Brodeur

Science Applications, Inc.
ATTN: J. Naber
ATTN: V. Ophan
ATTN: V. Verbinski

Science Applications, Inc.
ATTN: W. Chadsey

Science Applications, Inc.
ATTN: D. Stribling

Singer Company
ATTN: J. Brinkman

Singer Company
Data Systems
ATTN: R. Spiegel

Solar Energy Research Institute
ATTN: A. Stanley

Sperry Rand Corporation
Sperry Microwave Electronics
ATTN: Engineering Laboratory

Sperry Rand Corporation
Sperry Division
ATTN: P. Maraffino
ATTN: R. Viola
ATTN: F. Scaravaglione
ATTN: C. Craig

DEPARTMENT OF DEFENSE CONTRACTORS (Continued)

Sperry Rand Corporation
Sperry Flight Systems
ATTN: D. Schow

Sperry Univac
ATTN: J. Inda

Spire Corporation
ATTN: R. Little

SRI International
ATTN: P. Dolan
ATTN: A. Whitson

Systron Donner Corporation
ATTN: J. Indelicato

Teledyne Ryan Aeronautical
ATTN: J. Rawlings

Texas Instruments, Inc.
ATTN: R. Stehlin
ATTN: A. Peletier

TRW Defense & Space Systems Group
ATTN: A. Pavelko
ATTN: A. Witteles
ATTN: O. Adams
ATTN: R. Kingsland
ATTN: R. Schnieder
ATTN: H. Holloway
ATTN: H. Haid
ATTN: P. Guilfoyle

TRW Defense & Space Systems Group
ATTN: M. Gorman
ATTN: F. Fay
ATTN: R. Kitter

TRW Systems and Energy
ATTN: D. Millward
ATTN: G. Spehar

Vought Corporation
ATTN: Library
ATTN: Technical Data Center
ATTN: R. Tomme

Westinghouse Electric Corporation
Aerospace & Electronic Systems Division
ATTN: L. McPherson

Westinghouse Electric Corporation
Defense and Electronic Systems Center
ATTN: D. Crichi
ATTN: H. Kalapaca